UNIVERSITY OF GENOVA

PHD PROGRAM IN BIOENGINEERING AND ROBOTICS

Microfluidic organ-on-chip for assessing the transport of therapeutic molecules and polymeric nanoconstructs

Maria Grazia Barbato

Thesis submitted for the degree of Doctor of Philosophy

XXXIII cycle

March 2021

Paolo Decuzzi	Supervisor
Giorgio Cannata	Head of the PhD Program

Thesis Jury:

Francesco Gentile Università degli Studi di Napoli Federico II	External examiner
Filippo Causa Università degli Studi di Napoli Federico II	External examiner

Department of Informatics, Bioengineering, Robotics and Systems Engineering

Fight for things that you care about, but do it in a way that will lead others to join you.
Ruth Bader Ginsburg

A mamma e papà

Declaration

I hereby declare that except where specific reference is made to the work of others, the contents of this dissertation are original and have not been submitted in whole or in part for consideration for any other degreeor qualification in this, or any other university. This dissertation is my own work and contains nothing which is the outcome of work done in collaboration with others, except as specified in the text and Acknowledgements. This dissertation contains fewer than 65,000 words including appendices, bibliography, footnotes, tables and equations and has fewer than 150 figures.

Maria Grazia Barbato

March 2021

Acknowledgements

This Thesis would not have been possible without the costant presence of my family, Beatrice, Elisabetta and Gianbenedetto, and my dear Simone.

I am deeply grateful to my supervisor Prof. Paolo Decuzzi who accompanied me into this scientific journey, guiding me and pushing me beyond my limits. I am taking this opportunity to thank also my labmates that shared with me these last years, offering always support, knowledge and patience. A special thanks goes to the “little” family I met in Genova, Martina, Valentina and Miguel, who have been my rock in this journey. And thanks also to all the brilliant researchers who made this PhD-work possible.

Table of Contents

Chapter 1

State of the art

1.1 The vascular system

The discovery of the circulatory system represented a revolution that completely changed the understanding of living systems. The first description of the circulatory system dates back to 1628 when William Harvey demonstrated that blood circulated around the body through a system of arteries and veins. In 1865, Wilhelm His coined the term “endothelium” to differentiate the inner lining of body cavities from “epithelium”. Few years later, in 1874, Theodor Schwann observed, for the first time, the capillary wall in tadpole. [1] The branched network of blood vessels, consisting of arteries, veins, and capillaries, ensures tissue and organ homeostasis, delivery of gases, nutrients, metabolites, cells, and removal of waste products. These functions are developed earlier in the embryo, where spatio-temporally defined interactions lead to establishing a functional vascular system. [2] During development, vasculature develops through vasculogenesis, the formation of *de novo* vessels from the association of endothelial cell precursors known as angioblasts, and angiogenesis, the formation of new vessels by sprouting of pre-existing vessels (**Figure 1.1**). Formation of vasculature is followed by stabilization, involving the recruitment of mural cells and the generation of extracellular matrix (ECM), branching, remodeling, with cues

coming from the environment and lastly specialization, including arterio-venous determination and organ-specific capillary structure. [3]

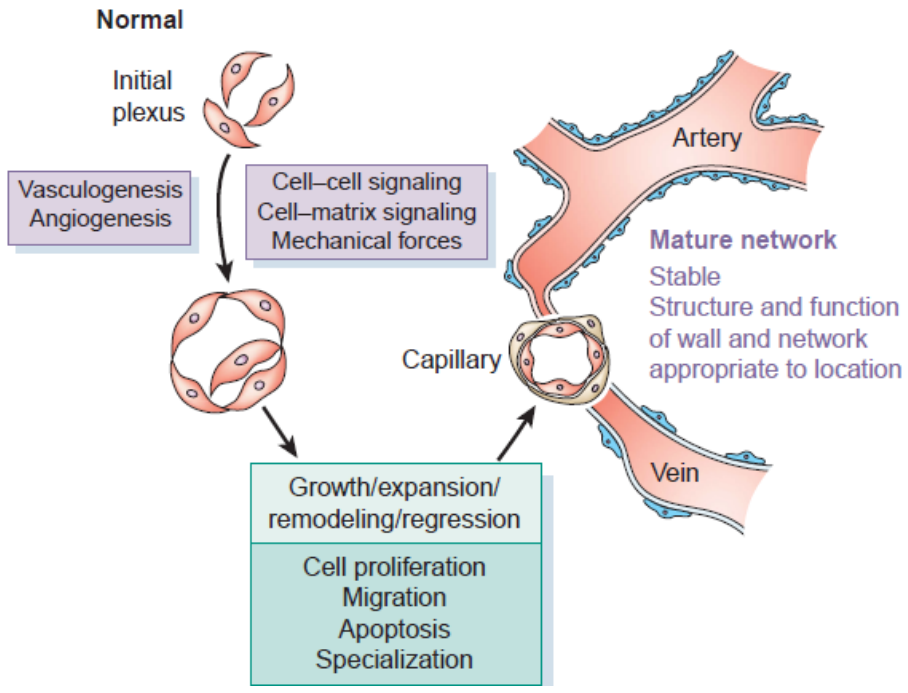

Adapted from *Jain, R.K., Nature medicine, 2003.*

Figure 1.1. Formation and maturation of vascular network. Vasculature forms via vasculogenesis or angiogenesis, processes regulated by cell-cell and cell-matrix interactions. The nascent vasculature undergoes further steps of stabilization, branching and remodeling. During last step of specialization, a stable network of arteries, veins and capillaries is functionally assembled. [3]

Despite regional and organ differences, blood vessels consist of three distinct regions:

- *Tunica intima*, a single layer of endothelial cells, lying on the basal lamina;

- *Tunica media*, containing smooth muscle cells (SMCs) and elastic fibers:
- *Tunica adventitia*, composed of fibro-elastic connective tissue. [4]

Based on the type of vessels and organs in which they reside, endothelial cells (ECs) show defined structural and functional properties. Organ-specific vasculature differs in permeability, delivery of nutrients to organs and traffic regulation of immune cells. [5]

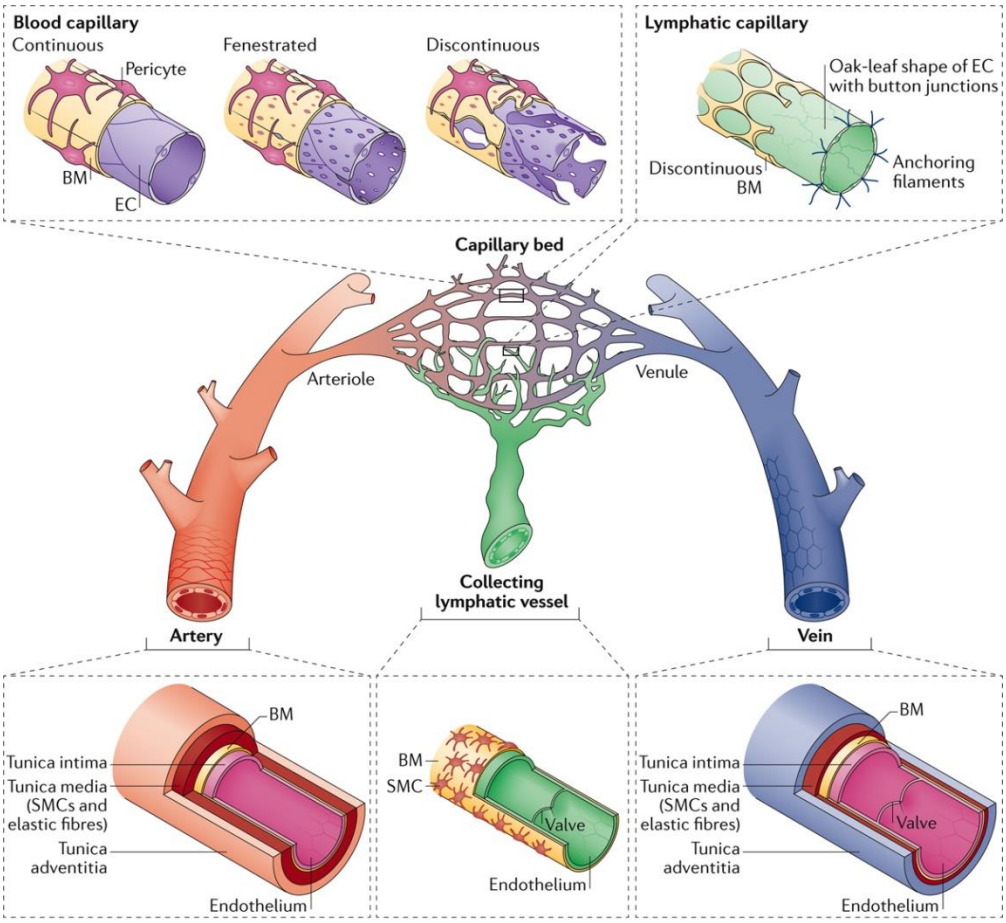

Adapted from *Potente et al., Nature Reviews Molecular Cell Biology, 2017*

Figure 1.2. Schematic of vascular organization. Arteries (red), veins (blue) and interconnected capillaries constitute the vascular network. Arterioles, capillaries and venules constitute the microvasculature. Three type of capillaries can be found: continuous, fenestrated and discontinuous (or sinusoidal). [5]

Capillaries constitute the majority of surface area of circulation, resulting in ~ 4000-7000 m^2 for an average-sized human. [6] Across this surface, nutrients, solutes, and water are exchanged between blood and tissues through diffusion and convection. A single layer of endothelial cells, lying on the basal lamina surrounded by pericytes, constitutes the capillary network leading to small vessels with a diameter of 5-10 μm. There are three types of capillaries: continuous, fenestrated, and sinusoidal (**Figure 1.2**).

Endothelial cells of continuous capillaries, for instance, brain capillary, are tightly bound together, allowing the passage of water, small molecules, and lipid-soluble materials while restricting the diffusion of larger molecules, drugs, and pathogens. Fenestrated capillaries, observed, in kidneys and some intestinal tracts, present pores that enable the passage of larger solutes that are compatible in size with peptides. Sinusoidal capillaries, located in the liver and spleen, present gaps between endothelial cells allowing the passage of larger molecules comparable in size with plasma proteins. [7]

1.2 Vascular Permeability

The term “closed” commonly describes the vascular system, but physiologically it also needs to be “open”, meaning permeable, to ensure the exchange of gases, nutrients, and wastes across tissues. Leakage of a dye from the capillaries of a developing amphibian tail was first observed in 1935, describing the phenomenon of vascular permeability for the first time. [8] Vascular permeability is an intrinsic feature of blood vessels, reflecting the integrity and tightness of the endothelial barrier. It is essential for homeostasis, and it varies among different organs, adapting

to physiological and biological needs (for example, temperature, exercise), and contributes to the pathophysiology of many diseases, such as arthritis, infections, stroke, and cancer. [9] Along the vascular tree, arterioles present low permeability values, while venules present higher permeability values, from ~10^{-6} to 10^{-4} cm/s.[10] Capillaries and post-capillary venules are considered as the site of fluids, solutes, and nutrients exchange. Capillaries are responsible for fluid passage, while post-capillary venules are mainly responsible for plasma proteins leakage and leucocyte extravasation. [11]

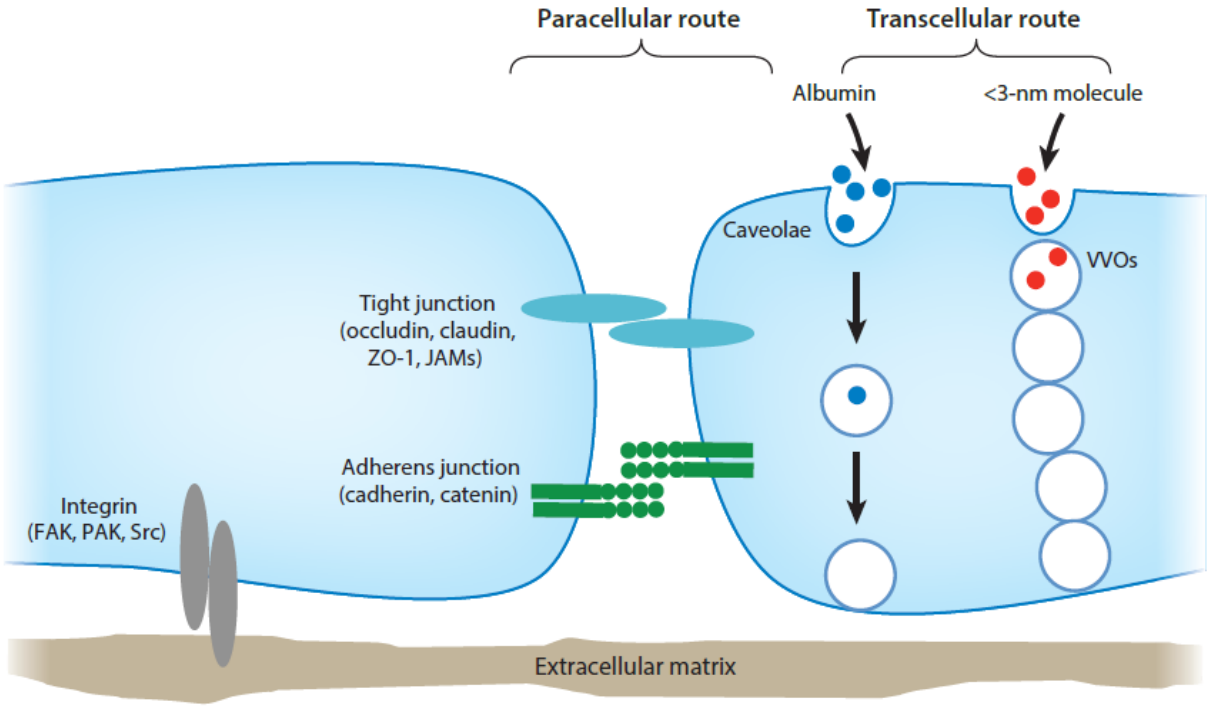

Adapted from *Park-Windhol et al., Annu.Rev.Pathol.Mech.Dis, 2016*

Figure 1.3. Paracellular and Transcellular pathways across endothelial cells. The transport of fluids and molecules across the endothelial barrier can occur through the paracellular or transcellular route. [15]

Two different pathways contribute to the movement of solutes across the endothelial barrier (**Figure 1.3**):

- The paracellular route, enabling free convective and diffusion transport of molecules and solutes smaller than 3-5nm through the opening and closing of adherens junctions (AJs) and tight junctions (TJs):
- The transcellular route or transendothelial vesicular transport, passing through a vesicles-mediated transport of molecules and involving caveolae and vesiculo-vacuolar organelles. [12]

Adjacent endothelial cells are connected by AJs and TJs, whose number and organization are organ- and tissue-specific. Two cadherins are highly expressed by endothelial cells : VE-cadherin, which is specifically presents on endothelial cells, and neuronal cadherin (N-cadherin), which is presents also on neural cells and smooth muscle cells. Despite similar level of protein expression only VE-cadherin is located at cell–cell contacts, whereas N-cadherin is distributed over the whole cell membrane [13, 14] VE-cadherin junctional protein is essential for endothelial barrier integrity and it is characterized by extracellular cadherin motifs, a transmembrane domain and an intracellular domain. The juxtamembrane intracellular domain mediates the interaction with p120, while the distal intracellular domain interacts with β-catenin and plakoglobin, which bind in turns to α-catenin, linking the VE-cadherin complex to the actin cytoskeleton. [9, 13] Three families of transmembrane proteins compose the TJs: claudins, occludins and junctional adhesion molecules (JAMs). Through their cytoplasmatic domain, these proteins are linked to the actin cytoskeleton via binding proteins like ZO-1 and cingulin, thus directing, controlling and limiting paracellular permeability. AJs are necessary for the formation of TJs, leading to the concept that changes in AJs are coordinated with changes in TJs. [15]

An increase in endothelial permeability is related to the formation of small gaps between endothelial cells, and change in VE-Cadherin distribution along cell borders. Hyperpermeability conditions are linked to an increase in endothelial permeability, can be brief and reversible after a stimulus such as acute inflammation, or sustained as in chronic inflammation and tumors (**Figure 1.4**). [9, 13]

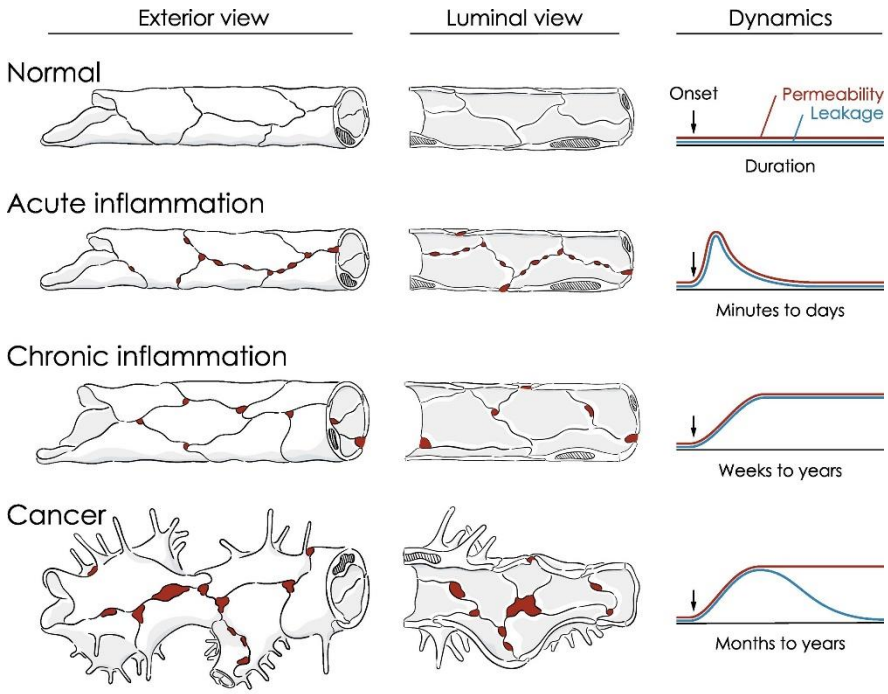

Adapted from *Claesson-Welsh et al., Cell Press, 2020*

Figure 1.4. Dynamics of vascular permeability. In normal vessels, cells are arranged into a uniform barrier that prevents the leakage of proteins and solutes. In acute inflammation, gaps formed between endothelial cells, leading to a transient increase in endothelial permeability. In chronic inflammation, a sustained increase in permeability in associated with gaps formation that can be reverted only with pharmacological treatments. In cancer, the formation of junctions between endothelial cells in defective, resulting in a sustained increased permeability.

In particular, besides epigenetic and genetic changes, tumors require the induction of a tumor vasculature. Neo-vascularization in tumors is a key step to ensure the supply of oxygen, metabolites, and waste removal for tumor progression. Tumor blood vessels are irregular and

tortuous, and blood flow is slow and irregular. They are often leaky and hemorrhagic, resulting in an upregulated inflammatory response. [16]

Permeability-increasing agents or endothelial barrier protectors modulate endothelial permeability. Among permeability-increasing agents, vascular permeability growth factor (VEGF), discovered in 1980s, is the most well-known. Activation of VEGF leads to the phosphorylation and disassembly of VE-cadherin, promoting formation of gaps and plasma leakage. [17] Similarly, thrombin, histamine, bradykinin, nitric oxide (NO), and lipopolysaccharide (LPS) promote vascular permeability. [9, 12] Conversely, endothelial barrier protectors, like cyclin-adenosine-monophosphate (cAMP), Sphingosine-1 (SP1), and Angiopoietin-1 (Ang-1), prevents increases in endothelial permeability, thereby preserving the endothelial barrier integrity. [12, 17]

Permeability coefficients represent the functional measure of microvascular exchanges of capillary walls. The exchange of fluids across the endothelium is driven by the difference in hydrostatic pressure generated by the circulating blood fluid and the concentration gradients of plasma proteins between the vascular lumen and the extravascular space. [11] This is expressed in the Starling equation, summarized as:

$$J_v/A = L_p\ [\Delta P - \sigma\Delta\pi] \text{ (Eq.1)}$$

Where J_v is the fluid volume filtration rate (mL/s); A is the endothelial surface area (cm^2); ΔP is the hydrostatic pressure difference across the capillary wall (mmHg); $\Delta\pi$ is the oncotic pressure difference, derived by plasma proteins between the lumen and extravascular compartment. In addition, L_p is the hydraulic conductivity, a coefficient that describes the permeation of capillaries

to water; σ is the osmotic reflection coefficient, that describes the sieving properties of capillaries (comprise between 0 and 1, where 0 define a completely permeable capillary, and 1 a completely impermeable capillary). [18] Under physiological conditions, there is no plasma protein crossing into the interstitial tissue (concentration of albumin in the blood is 4.5 g/dL). Consequently, the oncotic pressure is directed into tissue, while the hydrostatic pressure is directed into the lumen of the vessel. In pathophysiological conditions, plasma proteins accumulate into the tissue, leading to the accumulation of large quantities of fluid and leads to edema formation. [11] The exchange of solutes across the capillary walls is related to two forces, convection and diffusion. When plasma proteins are dragged along the fluid current, convection prevails as exchange mechanism; instead, when the fluid becomes slow in distal microvessels, diffusion prevails. In this condition, it is the Fick's law that describes the passive diffusion of solutes with the following equation:

$$J_s = D * A * \Delta C/\Delta x \text{ (Eq.2)}$$

Where, J_s is the flux of solute, driven by a concentration difference (ΔC) over a surface area A, along the distance Δx, following the diffusion coefficient D of the solute. [19]

Diverse approaches, both *in vitro* and *in vivo*, are used to measure endothelial permeability quantitatively. Generally, *in vitro,* endothelial cells are cultured as a monolayer on porous filters in Transwell chambers to ensure the endothelial barrier tightness. Through fluorescent-based approaches, the accumulation of a fluorescent tracer from the top compartment to the bottom compartment is measured as a function of relative fluorescence intensity over time. [17] Alternatively, it is possible to measure endothelial barrier integrity as a function of the electrical resistance. Lipophilic molecules cover endothelial cells' membranes, restricting the passage of aqueous solutions and functions as an electric insulator. Transendothelial Electrical Resistance

(TEER) is a function of the electrical resistance of the endothelium. Probes are placed in the luminal and abluminal side, and the impedance to flow to small inorganic ions is calculated, reflecting the barrier integrity of the endothelial monolayer. [11] However, *in vitro*, most common endothelial cells used in culture are derived from large vessels that cannot be representative of microvascular cells. Usually, endothelial cells cultured on a plastic substrate undergo significant changes in phenotype and upregulation of inflammatory genes. Moreover, loss or alterations of adhesion and junctional proteins lead to higher permeability values. Simultaneously, lack of flow conditions, basement membrane and supporting cells do not resemble the blood vessel physiological structure. [20] *In vivo* approaches for the measurement of vessel permeability rely on cannulation and perfusion of single vessels in selected region of the microvascular bed. The most commonly used assay is the Mile Assay.[21] In this technique, a colored dye, that strongly bind to albumin (e.g. Evans blue), is injected into blood circulation, and its accumulation into a specific site is observed over time. However, this technique present several limitations. For example, it is not compatible with non-inflamed tissue, where albumin does not cross the endothelium. Dual Isotope approach, Intravital Microscopy, Magnetic Resonance Imaging (MRI) and Positron emission tomography (PET) techniques are also employed to measure endothelial permeability *in vivo*. [11, 17] However, animal experiments are time-consuming, technically demanding, suffer from intrinsic variability between animals and present well-known ethical limitations. More importantly, several legislation require adherence to the 3R principles (replacing, reducing and refining) to reduce animal testing while promoting alternatives. In this scenario, microfluidic technologies offer the possibility to overcome the limitations of *in vitro* approaches in vascular biology, and at the same time to faithfully recapitulate the *in vivo* physiological environment of blood vessels.

1.3 Microfluidic technologies

By definition, microfluidic is the manipulation of small amounts of fluids (10^{-9} to 10^{-8} liters) using channels of width ranging from tens to hundreds of micrometers. [22] By employing technologies first developed in the semiconductor industry, fluids can be manipulated using microscale devices. In 1950s, the first microfluidic technology was developed, putting the efforts for dispensing small amounts of fluids in the range of nano- and picoliter – the basis of the actual ink-technology. Years later, a simple microfluidic analysis system based on capillary liquid structure reached the market. These systems were used in the detection of pregnancy, drug abuse, or cardiac markers. [23] In the recent years these microfluidic devices are referred as "lab-on-chip". They have also been applied in the biological research, offering several advantages: the reduction of volumes and reagents cost, the spatio-temporal control of cell environment and the possibility of assay parallelization. At the microscale, fluid phenomena are different from those that are dominant at the macroscale. In particular, laminar flow, surface tension and capillaries forces are the ones that dominate at the microscale level, which translate into phenomena like passive pumping into microchannels, precise surface patternig and monodisperse droplets formation. [24]

Primarily, the development of microfluidic devices focused on the fabrication of silicon and glass, using cleanroom techniques. For the selection of substrate materials for a microfluidic device in biological research, it is important to consider some particular characteristics such as optical transparency for cell imaging, the desired degree of mechanical rigidity or flexibility, surface chemistry reactivity and biocompatibility. According to these criteria, it is clear that both silicon and glass are not suitable materials for bio-microfluidics application, because:

- Silicon is opaque to visible and ultraviolet light, making it incompatible with microscopy techniques and requires expensive fabrication techniques;
- Glass is a brittle material, requires non trivial-bonding process, and possesses inaccessible and expensive fabrication methods. [25]

In the 1970s, the Bell Lab developed a new fabrication technique, the elastomeric micro-molding.[26] In 1998 the first PolyDiMethylSiloxane (PDMS) microfluidic device was fabricated by the group of Whitesides, giving rise to the era of soft-lithography. [27] PDMS in an optically transparent elastomer, that is permeable to gas and vapor. It is widely adopted in bio-microfluidic applications due to its relatively low-cost, ability to tune its hydrophobic-hydrophilic properties, reversible and irreversible bonding to glass and other materials and its elasticity. [24, 25] There is a wide range of microfabrication techniques for producing microfluidic devices. The most commonly used fabrication process is photolithography, a set of techniques initially developed by the semiconductor industry. Photolithography involves the use of a photosensitive polymer, so-called photoresist, to pattern the microfluidic structure. Two types of photoresist exists, positive and negative . When a positive photoresist is exposed to UV light, the exposed region becomes soluble and the unexposed region is polymerized. In the case of negative photoresist, the opposite occurs, the exposed region becomes polymerized, and the unexposed area is soluble in an appropriate solution. During the photolithography process, a layer of resist, generally SU-8, a commonly used epoxy-based negative photoresist, is spin-coated onto a substrate, silicon, or glass wafer. Then, it is structured with a photomask, creating the targeted channel layout. After patterning, the un-polymerized photoresist is removed by rinsing with an appropriate solvent, leaving the microfluidic design patterned on the wafer. Subsequently, the glass or silicon can be selectively etched using hydrofluoric acid (wet-etching) or with reactive ion etching (dry etching),

to form the structures in the substrate. [28] But, as previously reported, silicon and glass are not suitable materials for biological applications.

The most widely used approach to fabricate microfluidic devices is soft-lithography. The success of the technique is related to its simplicity, the materials properties, its relative low cost, the advantageous surface chemistry and replication accuracy. In this process, instead of using the wafer material to fabricate the chip, the wafer is now used as a mold with a positive channel structure relief. A thermosetting elastomer is poured over the mold and allowed to polymerize, reproducing the microfluidic layout (**Figure 1.5**).

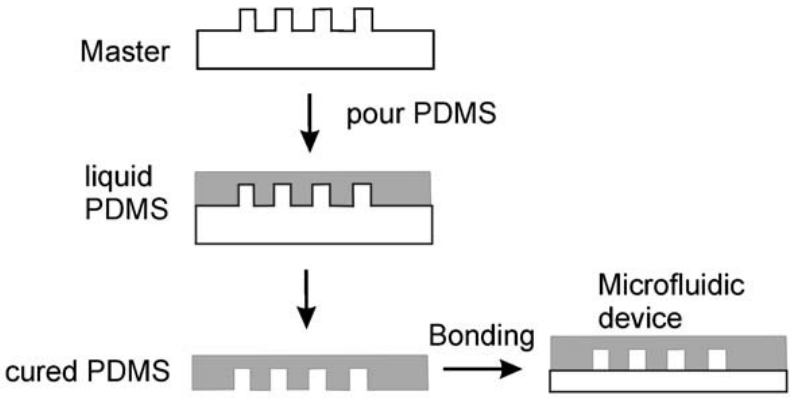

Adapted from *Beker et al., Anal Bioanal Chem, 2008*

Figure 1.5. Creation of microfluidic devices. A soft-lithography approach is used to create the microfluidic pattern. PDMS is poured over the master template generating a stamp. The stamp can be irreversibly bonded to a basement substrate to generate closed microfluidic channels for perfusion studies. [22]

The most used material in microfluidic devices is PDMS. Typically, ten parts of the elastomer and one of the curing agents are mixed together, forming three-dimensional bonds through an organometallic crosslinking reaction.[29] The mixture is then degassed, poured over the master template, and cured at room temperature for at least 48h. Using higher temperatures reduced the

curing time. After polymerization, the elastomer with embedded structure is peeled off the wafer, building three-dimensional structures that can be closed by placing another piece of elastomer or glass *via* bonding procedures. [25, 28]

In biological research, animal studies remain the gold standard for the preclinical validation of drugs in pharmaceutical development. However, besides the well-known ethical limitations, several studies from the Food and Drugs Administration (FDA) and the National Institute of Health (NIH) revealed a failure of ~90% in the results of drug testing from animal models. [30] On the other hand, *in vitro* cell cultures lack the *in vivo* tissue architecture, physiological functions, complex tissue and organ-level structure, and the interplay between multiple organs. As alternative models to animal studies, organoids have been proposed. However, these 3D models

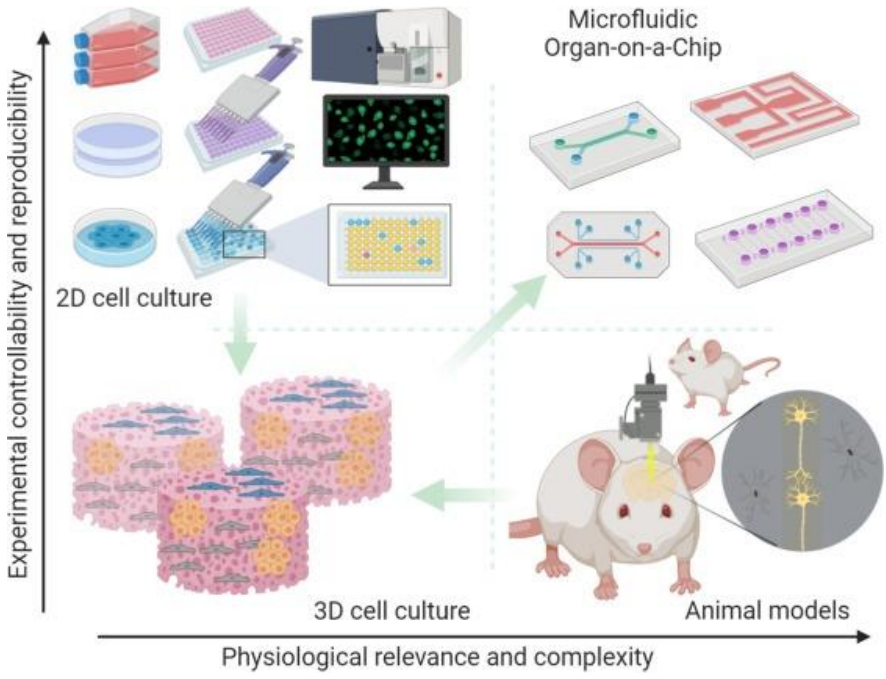

Adapted from *Ma et al ,Trends in Pharmacological Sciences, 2021*

Figure 1.6. Microfluidic technologies. Organ-on-chips bridge the gap between *in vitro* (2D and 3D) and *in vivo* conditions giving the possibility of mimic organotypic cellular architecture and functions. [27]

lack tissue-tissue interfaces, vascular flow, and mechanical cues. Thus, to bridge the gap between *in vivo* and *in vitro* conditions, starting from the early 2000s, microfluidic technologies have been applied (**Figure 1.6**). [31, 32]

Microfluidic Organ-on-Chip can recapitulate vascular perfusion, tissue-tissue and tissue-matrix interactions aiming to reproduce organotypic cellular microenvironment and functionality for disease modeling and drug screening.[33] These can be lined with most of the cell sources available, such as primary cells, induced pluripotent stem cells (iPSC), or cells derived from patients for personalized medicine. In the last years, several microfluidic models have been proposed in order to recapitulate human physiological features, disease state and drug screening. [34] Single Organ-on-Chip recapitulate a specific tissue or organs, but it is also possible to fluidically link multi organ-on-chip in order to model the so-called "Body-on-chip". These platforms showed better response than animal models as drug screening platforms for pharmacokinetics and pharmacodynamics study, giving evidence that microfluidic patforms can be employed as potential alternative to animal models. [35]

1.4 Vasculature-on-chip

From an engineered point of view, the human vascular tree ranges from the centimeter-scale aorta to micrometer-scale capillaries. To engineer the complex capillary network and endothelial barrier functions, numerous strategies have been developed to capture the complexity of the vascular niche. Over the past decades, tissue-engineers fabricated large vessels ranging from 1 to 10 mm for vascular grafts and artery repair through different biomaterial-based approaches. However,

when it comes to microvascular networks, design and fabrication techniques employing lithography, 3D printing and laser ablation techniques need to be revised. Microvasculature is structured as a dense network of micro-sized capillaries (~5-10 μm) located <100 μm from one another. [36] It was the 1980, when Judah Folkman and Christian Haudenschild observed for the first time the formation of vascular lumen *in vitro*. In the assay, endothelial cells (ECs) formed tubes onto an extracellular matrix (ECM) by using collagen, fibrin or Matrigel. [37] Years later, development of microfluidic systems offered the possibility of integrating angiogenesis-on-chip introducing additional stimuli as flow, biochemical gradients, and compartmentalized co-culture. Based on fabrication methods, microfluidic vessels can be divided into three main categories:

1. 2D layer of endothelium in microfluidic model;
2. 3D lumenized microvasculature adopting the wall patterning method;
3. 3D lumenized microvasculature based on self-morphogenesis.

The first two categories are based on top-down fabrication approach, while a bottom-up fabrication approach is the base of the third one (**Figure 1.7**). [38]

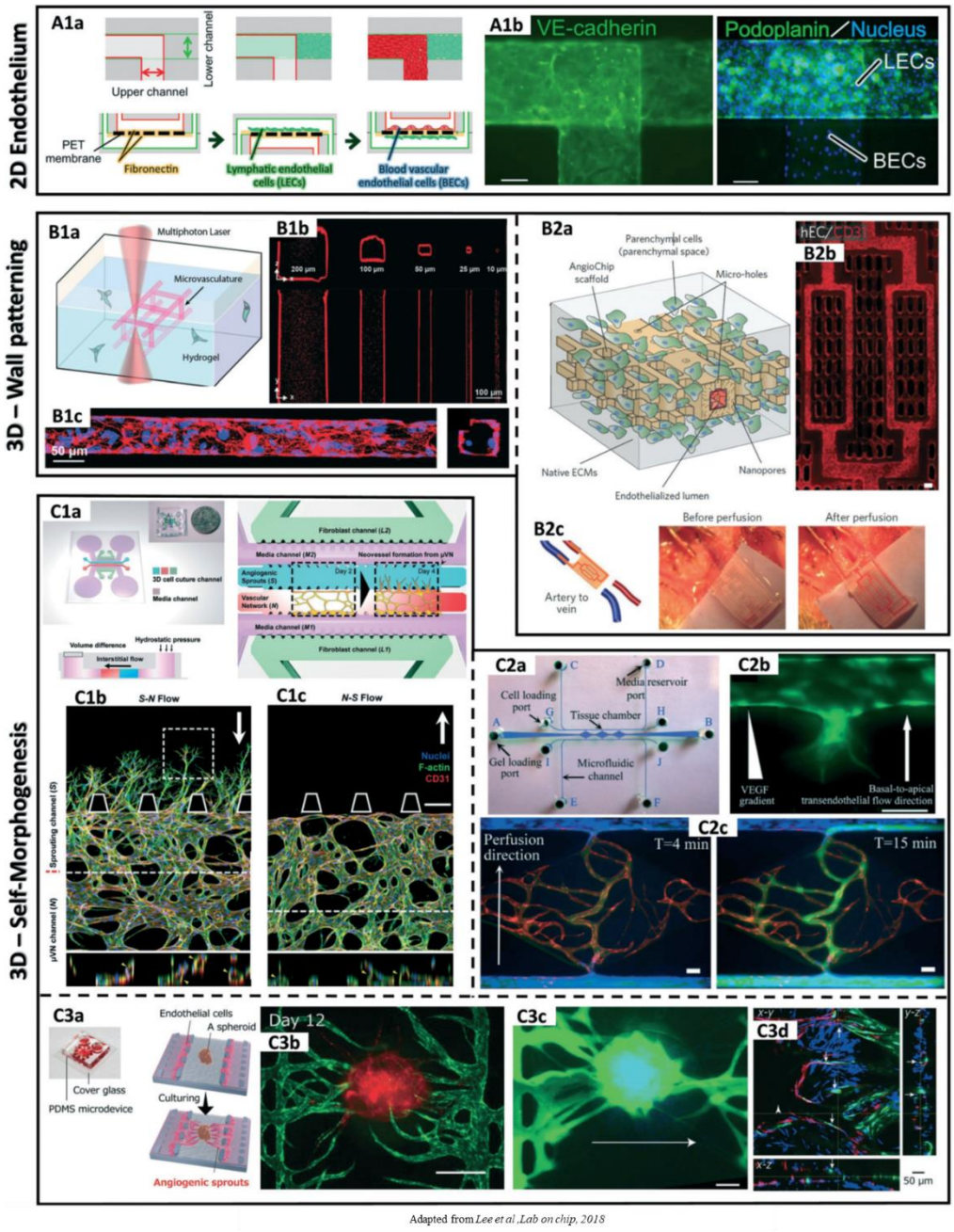

Adapted from *Lee et al ,Lab on chip, 2018*

Figure 1.7. Vessel-on-chip main categories. A). 2D layer of endothelium in microfluidic device. B) 3D lumenized microvasculature based on the wall patterning method. C) 3D lumenized microvasculature based on the self-morphogenesis. [31]

In 2D layer of the endothelium in microfluidic devices, ECs are attached to the microfluidic channels' walls. Though ECs are not directly cultured into a 3D matrix, they gained specialized features from contact with the ECM, from a co-culture with parenchymal cells that can be loaded into a parallel channel, or from the flow. Another significant advantage of this type of

configuration is the possibility of measuring the permeability of the vessel. In this context, Kamm's group gave a masterful example. They developed a microfluidic vascular-tumor interface for precise quantification of endothelial barrier function. Endothelial permeability was measured across HUVEC monolayer in the presence or absence of tumor cells, and tumor cell migration was calculated under control and inflammatory conditions. [39] A drawback of this technique is the non-physiological rectangular shape of the channels.

To address this issue, 3D lumenized microvasculature can be generated by sacrificial molding or wall patterning method. In this approach, particular attention is given to reconstituting microvessels in a 3D structure. A hollow capillary network in 3D ECM can be generated employing different techniques. One of the earliest techniques developed was needle molding. Tien group in 2006 was a pioneer in developing perfusable vessel structures by casting a hydrogel around a removable needle. Upon removing the needle, ECs were introduced into the channel and allowed to adhere to the hydrogel walls. [40] A different technique to model complex 3D vasculature is by sacrificial molding. A sacrificial material is cast into molds to form the desired layout. Subsequently, the material is embedded within a hydrogel and, after its solidification, the sacrificial material is washed away, leaving behind the desired structure. Kaplan group combined gelatin sacrificial molding and a layer-by-layer approach to fabricate a silk hydrogel microfluidic system. Briefly, a negative PDMS stamp was used to form a positive gelatin microchannel that was subsequently transferred into the silk hydrogel solution. This step was repeated two times in order to form a complex 3D structure layer-by-layer. After the assembly, the gelatin mold was melted and flushed away by incubating the devices at 37°C. [41] More recently, microchannels

have been directly generated in hydrogels by photoablation or photodegradation. Lasers with enough energy to break down covalent bonds can ablate microscale voids in various soft hydrogels, such as collagen, fibrinogen, and silk protein hydrogel. [42] The Slater group generated a complex, dense and tortuous vascular network by laser-based degradation and image-guided laser control onto a poly-(ethylene glycol) diacrylate (PEGDA) hydrogel recapitulating accurately the *in vivo* microvasculature. [43] Because of the broad application potentials, 3D printing has gained great attention in the last decades. 3D printing techniques can be divided in two main categories: directing printing, where a cell-laden material is deposited onto a surface, and indirect printing, where a sacrificial material is embedded into a large cell-laden material. [36] Dvir group reported a 3D-print thick, vascularized and perfusable cardiac tissue. [44] Starting from a biopsy of omental tissue, a patient-specific extracellular matrix was developed as bio-ink. Cells, derived from the same biopsy tissue, were reprogrammed into pluripotent stem cells, and differentiated to cardiomyocytes and endothelial cells. Subsequently, the two cell types were combined with the bio-ink to print the parenchymal cardiac tissue and blood vessels. [44]

Vascular networks can also be formed by a bottom-up approach as in 3D lumenized microvasculature based on the self-morphogenesis. Instead of seeding cells into predefined structures, ECs can exploit angiogenesis and vasculogenesis processes to generate functional and stable microvascular structures. By balancing angiogenic factors and a suitable ECM, 3D microvasculatures are assembled into microfluidic devices. Kamm group generated a 3D microvascular network into a fibrin extracellular matrix by co-culturing endothelial cells and stromal cells. The designed microenvironment favored vasculogenesis, by forming endothelial connections, branch and anastomosis, resembling the *in vivo* vasculature. Moreover, the 3D network showed the presence of continuous tight junctions between endothelial cells, a functional

glycocalyx, and size and charge-selective barrier to the passage of solutes. [45] Recently, 3D-self assembled microfluidic vasculature has been applied to overcome one of the major limitation of organoids and spheroids, meaning, the development of a functional and perfusable vasculature. [46] Recently, it was reported a spheroid model containing a perfusable vascular network by defining the cellular interaction between the spheroid and endothelial cells [23]. Yokokawa group developed a tumor spheroid with an integrated perfusable vascular network to recapitulate the *in vivo* tumor microenvironment. Tumor spheroids were perfused over 24h through the vascular network, and anti-cancer drug assays were performed. [47]

A plethora of perfusable microvessel models have been developed. They can be classified based on the fabrication method used in 2D layer of the endothelium in a microfluidic model, 3D lumenized microvasculature by wall patterning method and 3D lumenized microvasculature by self-morphogenesis. Microfluidic vessels vary in complexity and physiological relevance, but provide a powerful kit for the study of vascular phenomena and methods to vascularize artificial organs.

1.5 Cancer-on-chip

As reported by the International Agency for Research on Cancer (IARC), cancer is the second leading cause of death globally, accounting for an estimated 9.6 million deaths in 2018. [48] Testing potential anticancer drugs in tumor cell cultures is the first step in cancer therapeutics preclinical development. Subsequently, animal models are necessary to proceed into preclinical evaluation. In animal studies, tumor models could be implanted at a subcutaneous level or tumor

xenograft could be implanted into the same organ from which the tumor is derived, obtaining an orthotopic cancer model. However, both cell culture models and animal studies do not replicate the complex tumor microenvironment (TME), resulting in poor or altered therapeutic treatment response. [49] To bridge the gap between 2D *in vitro* cell culture and animal models, a new class of *in vitro* tools came into the arena. Integration of organotypic tumor cell culture with microfluidic devices, so-called "cancer-on-chip," allowed the recreation of TME. This allows researchers to understand tumor cell behaviors, investigate cancer cell interactions with other organs and spatio-temporal dynamics of tumor cascade. [50] Researchers for over 50 years used 2D cell cultures to assess the effect of drugs on tumor growth.

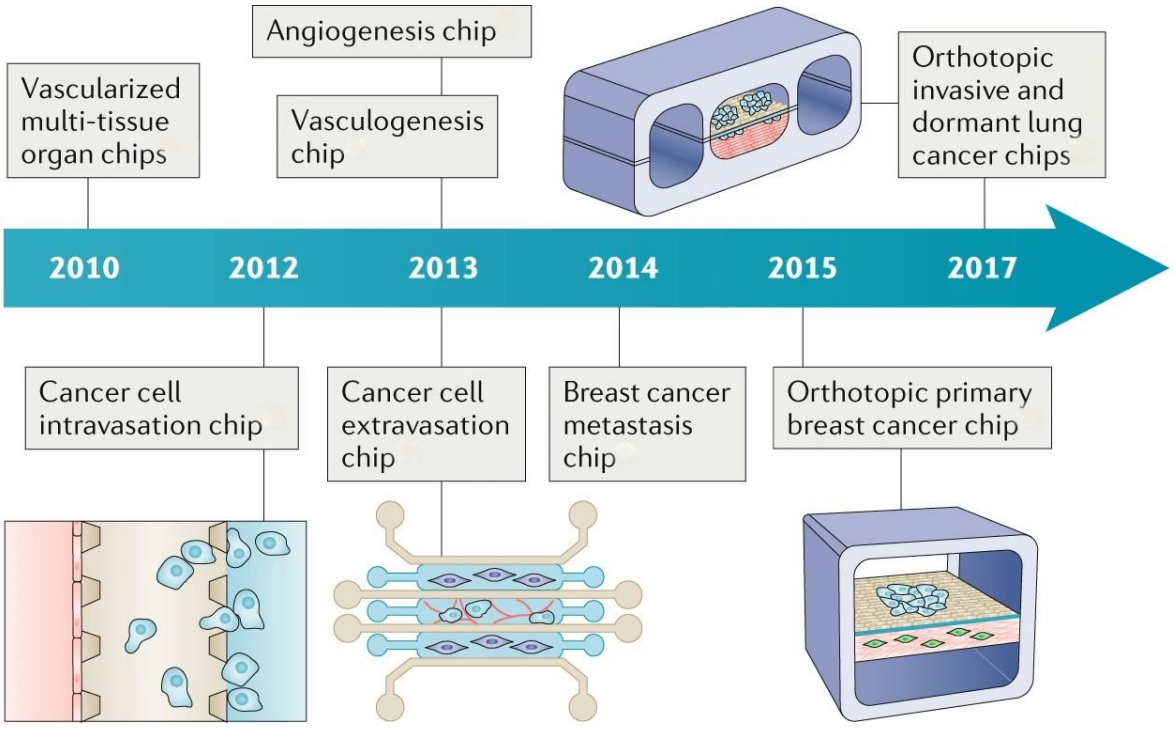

Adapted from *Sontheimer- Phelps et al., nature Reviews Cancer, 2019*

Figure 1.8. Timeline of cancer-on-chip development. Steps of tumor cascade replicated into microfluidic devices starting from 2010, with studies on tumor cell invasion. [42]

Over the past years,more complex systems have been developed in the Transwell system using tumor spheroids, aggregates of cells cultured in non-adherent conditions, to replicate a 3D tumor model. However, these models failed to recapitulate essential mechanical cues: shear stress, hydrostatic pressure, and tissue deformation. Microfluidic cancer-on-chips offer the possibility of integrating multicellular tissue-tissue interfaces, relevant microenvironment, perfusion and controlled biophysical, cellular and molecular stimuli. Cancer-on-chips offer the advantage of replicating specific step of the tumor cascade, as tumor growth and expansion, invasion and metastasis (**Figure 1.8**). [51]

Takayama group demonstrated the effective formation of tumor spheroids in microfluidic devices, recapitulating the niche microenvironment of prostate cancer metastases into the bone. They engineered a two-layer microfluidic system including prostate cancer cells, osteoblasts and endothelial cells. The fabricated micro-trap ensured the uniform incorporation of all cell types into the spheroid that was kept in place over one week. The culture system faithfully recapitulated the *in vivo* growth of cancer cells within the bone metastatic prostate cancer microenvironment. [52]

Interaction between tumor cells and its microenvironment is a key regulator of tumor progression, particularly in the formation of a premetastatic niche. For integrating tissue-specific cell cultures, microfluidic devices are a powerful platform for recapitulating the complicated metastatic tumor cascade. Kamm group presented a microfluidic platform in which they combined a microvascular network assembled via vasculogenesis, different cancer cell lines and a highly controlled microenvironment. They assessed the extravasation of cancer cells from the microvascular network in real-time, gaining insights into tumor cell extravasation mechanisms. [53] More recently, Cho group realized a liver-on-chip model to reconstruct the premetastatic niche and

investigate the mechanism of tumor cell homing, colonization, and proliferation in distant organs. [54] Interactions of cancer cells with microenvironment are extremely important to evaluate the effectiveness of anti-cancer drugs. Still, it is also important to assess the side effects of anti-cancer drugs on other organs. In fact, many drugs that pass preclinical tests are often withdrawn due to side effects detected during clinical trials or even after entering the market. Vunjak-Novakovic's group developed a multi-organ-on-chip platform by integrating two bioengineered human tissues, a bone tumor tissue and heart muscle, in order to evaluate the anti-tumor efficacy and cardiotoxicity of linsitinib. This anti-cancer drug showed promising results in patient-derived orthotopic xenograft models but failed in clinical trial Phase II. Their results showed that only engineered tumor tissues recapitulating bone microenvironment and integrated with heart muscle tissue were comparable with results from clinical trials, demonstrating that multi organ-on-chip could improve the predictive accuracy for direct and off-target effects of drugs. [55] For personalized anti-cancer treatments, patient-derived cancer cells have been analyzed in microfluidic models. The Wang group realized a 3D co-culture platform to evaluate drug sensitivity for a mono-lung cancer cell line, a mixture of lung cancer and stromal cell lines, and cells freshly derived from lung cancer tissues. In the co-culture condition, stromal cells and cancer cells gradually clustered to form a 3D spheroid, recreating a well-organized *in vivo*-like microenviroment. Moreover, the apoptosis rate of lung cancer cells decreased around two times when co-cultured with stromal cells, compared to mono-culture cells. In order to provide effective clinical guidance for individualized treatment, the anti-cancer drug sensitivity tests were carried out on fresh tissues of cancer. They defined the appropriate chemotherapeutic scheme for eight patients by generating a gradient concentration of anti-cancer drugs across the microfluidic device. [56]

Overall, organ- and cancer-on-chip could provide more significant insights into anti-cancer drug screening and toxicity before entering clinical trials. Cancer-on-chip can be linked with different physiological compartments, helping to predict drug side effects on different organs like the heart, liver and kidneys. Moreover, personalized cancer-on-chip could elevate personalized medicine to higher level, by recapitulating patient-specific pathophysiology and therapy response.

1.6 Brain-on-chip

In the central nervous system (CNS), the brain is the central player. Composed by 100 billion of neurons and 1 trillion of supporting glial cells finely arranged from the molecular to the organ level, the brain orchestrates and regulates the functions and mechanisms of the CNS in a delicate balance between the delivery of nutrients and energy supply for neuronal activity. [57] Neurophysiology and neuropathology studies are based on various model organisms, such as *Caenorhabditis elegans (C.elegans)*, *Drosophila*, rodents and non-human primates. The models offer advanced understanding of the brain and brain-related disorder pathophysiology, but critical issues remain. For example, manipulating small organisms such as *C.elegans* and *Drosophila* requires a certain level of expertise and is labor-intensive. On the other hand, rodent and non-human primates, despite significant similarities with humans, fail to recapitulate the essential features of the brain. [58] Together with animal models, 2D neural cell cultures are model systems broadly used.

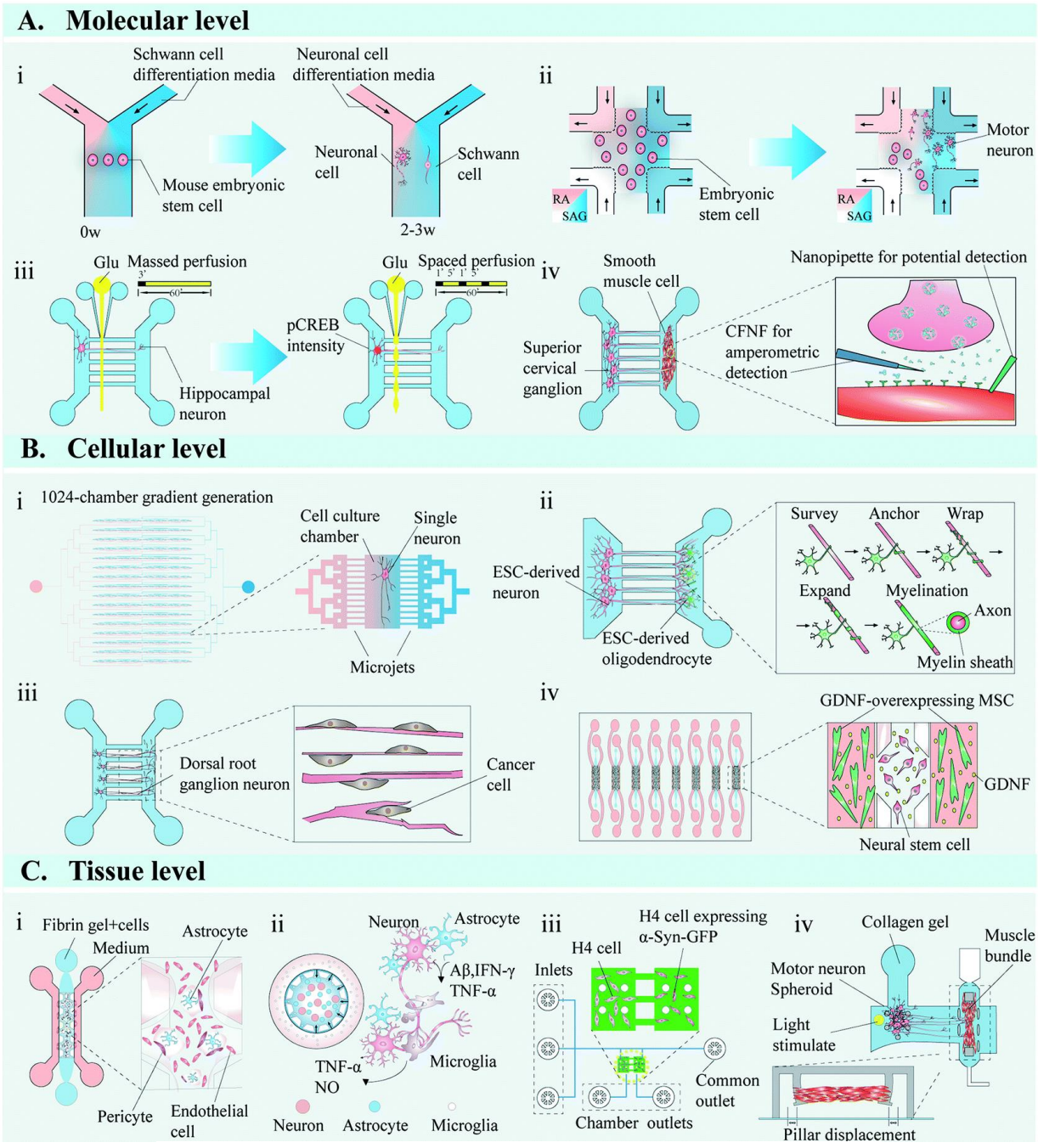

Adapted from *Zhao et al., Lab on Chip, 2020*

Figure 1.9. Microfluidic chip for neurobiology. (A) Microfluidic applied at the molecular level to direct neural differentiation, generate neurochemical gradients and neurotransmitter profiles. B) Microfluidic applied at the cellular level to study neural and non-neural cell crosstalk and neuro-guide formation. C) Microfluidic applied at the tissue level to recapitulate blood-brain-barrier (BBB) model and neuropathological disorders. [53].

Advances in 3D culture and neural differentiation led to new relevant models as 3D-scaffold neural structures, neuro-spheres and cerebral organoids. However, self-assembly of organoids and neuro-spheres does not resemble the exact position of neural cells. There is limited control of the 3D microenvironment in terms of neurochemical signals, neural cell type and ECM. [59] The coming era of microfluidic technologies offered the possibility of developing new neuro-microfluidic platforms to accommodate sophisticated mechanisms of neural cell cultures and controlled microenvironments. Brain-on-chip can (i) mimic the spatio-temporal dynamics of neurochemical signals; (ii) facilitate single neuron analysis and multi-cellular interactions; (iii) emulate neurophysiological and neuropathological conditions, accelerating the research and development of therapies for brain-related diseases such as Parkinson's, Alzheimer and brain tumors (**Figure 1.9**). [60]

Microfluidic chips at the molecular level provided a fine-tuned technology for generating gradient concentration of neurochemical molecules and determining neural fate. It is also possible to integrate into microfluidic devices opto- and electrochemical sensors coupled with real-time monitoring and analysis equipment. Lu and co-workers developed a microfluidic platform to culture stem cell aggregates under differently perturbed flow conditions. Particularly, they focused on the effect of device geometry and media exchange frequency. Discontinuous perfusion demonstrated optimal growth of stem cell aggregates and modulation of the device geometry-generated gradients of cell-secreted factors reflected in spatial differentiation patterns. [61]

Microfluidic devices can modulate neural activities and functions by fine-tuning cellular interactions and the surrounding microenvironment at the cellular level. Volontè's group studied neurite outgrowth by tuning the geometry of biophysical cues on a microfluidic device.

Micropillar-shaped geometry, micropatterned line-grating geometries and microfluidic channels were fabricated. They showed that primary microglia tended to be multipolar, extending protrusions in all directions and forming distinct pseudopodia on pillar-shaped geometries. Conversely, on both line-grating geometries and microfluidic channels, microglia presented a stretched and flattened morphology, assuming a filopodia-bearing bipolar structure. [62]

At the tissue level, microfluidic setup recapitulated key features of neurophysiological and neuropathological conditions, as Alzheimer's disease (AD), [63] Parkinson's disease (PD), [64] and amyotrophic lateral sclerosis (ALS).[65] Significant efforts have been made to recapitulate the blood-brain-barrier (BBB) on-chip and accelerate the development of new therapeutic strategies for brain-related disorders. Ingber group reported the development of a BBB organ-on-chip formed by induced pluripotent stem cell (iPSC)-derived human brain microvascular cells, primary human brain astrocytes and pericytes. To obtain highly differentiated and stabilized brain microvascular endothelial cells, iPSCs were cultured in hypoxic-condition, producing significant increases in the mRNA levels for the endothelial cell-to-cell adhesion molecules, VE-cadherin (vascular endothelial cadherin) and PECAM-1 (platelet endothelial cell adhesion molecule, also known as CD31), as well as the influx transporter GLUT-1 (BBB-specific glucose transporter), efflux transporter P-gp (permeability glycoprotein), and VEGF-A (angiogenic vascular endothelial growth factor-A), relative to control under normoxic conditions. The developed BBB-on-chip demonstrated low barrier permeability values similar to those observed in human brain for more than 2 weeks *in vitro*, reversible opening of the BBB using hypertonic mannitol solutions *in vitro*, as is done *in vivo*. The delivery of an FDA approved therapeutic antibody, mimicking a clinically relevant drug delivery strategy and mimic transporter-mediated drug efflux including appropriate

substrate specificity was achieved. These results provide significant advancement in drug screening applications. [66]

Microfluidic brain-on-chip offers great opportunities for neuroscience research and for personalized treatments of brain diseases. These neurological platforms could help discover the contributions of different cells and cytokines to neuropathological disorders and how cues in neuronal microenvironment regulate cell differentiation, neuronal development and progression of neurological disorders.

1.7 Conclusions

Microfluidic systems provide the technology to develop *in vivo*-like environments for the study of a broad variety of physiological and pathophysiological models. Integration of 3D extracellular matrix into microfluidic channels gives the opportunity to move from 2D culture models to 3D and multi-organ systems. Vasculature-on-chips represent a powerful tool for fundamental research into angiogenesis as well as vasculogenesis. Specifically, formation of functional vascular systems offer the possibility of screening biomolecules, drugs and nanoparticles in drug delivery application. In addition, cell motility and movement across vascular barriers are of great interest, in particular for research into metastasis. In cancer biology, organ-on-chips have resulted in highly complex three-dimensional systems that mimic a variety of different types of cancer, such as breast, lung, liver or bone cancer, with main application in anticancer drug screening and fundamental research into cancer metastasis. In neurobiology, most microfluidic devices are based on a combination of multidisciplinary research, providing complex lab-on-a-chip systems with

microstructures for cell separation, surface micropatterns that guide the adhesion and migration of cells and cell manipulators for studies of trauma and regeneration, as well as biosensors for non-invasive monitoring of cell-to-cell interactions.

To conclude, microfluidics is a powerful tool and set of techniques for controlling and analysing cell-to-cell interactions on different levels of complexity, such as single cells as well as microtissues.

Chapter 2

A permeable on-Chip microvasculature for assessing the transport of macromolecules and polymeric nanoconstructs

2.1 Introduction

The human vascular system has a remarkable ability to maintain tissue and cellular homeostasis in the body through a complex network of arteries, capillaries, and veins. The smallest vessels – the capillaries – are responsible for distributing nutrients and collecting waste from every single organ. As such, their walls comprise of only the basal membrane and a monolayer of endothelial cells.[67] Transport across capillaries, from the vascular to the extravascular compartment, occurs via the paracellular pathway, exploiting openings at the interface among adjacent endothelial cells; and the transcellular pathway, using receptors and intracellular vesicles as shuttles to connect the two compartments. Depending on the vascular district and the biophysical properties of the agent to be transported – small molecules, macromolecules and nanoparticles – the transcellular pathway could be more relevant than the paracellular pathway.[45, 68] For instance, very tight intra-endothelial cell junctions that limits the paracellular pathway in favor of a more selective transcellular transport, resulting in an overall modest vascular permeability, characterize the brain capillary network.[69-71] On the other hand, capillaries in the kidneys, intestine, and liver – the

liver sinusoids – are characterized by a discontinuous or even fenestrated endothelium that facilitates the paracellular transport, resulting into a high vascular permeability.[72, 73]

A variety of pathologies, including cancer, atherosclerosis, thrombosis, and more in general, inflammatory diseases, are associated with alterations in vascular permeability. [74, 75] For its dysregulated and chaotic growth, the cancer neo-vasculature presents a tortuous capillary network and large openings – fenestrations – that could range up to several hundreds of nanometers. This results in lower perfusion, and blood flow velocities, and higher vascular permeability as compared to healthy capillary networks.[76, 77] Similarly, the inflamed vasculature is associated with more relaxed endothelial junctions to favor the recruitment of circulating monocytes and other cells of the immune system from the vascular network to the diseased tissue.[78] Incidentally, these alterations in vascular permeability have been extensively exploited to facilitate the passive accumulation of a variety of therapeutic agents at diseased sites. For instance, in cancer therapy, the Enhanced Permeability and Retention Effect (EPR) has been invoked over the last 20 years to design liposomes, polymeric and metal-based nanoparticles that could accumulate within the malignant tissue through the vascular fenestrations and remain in there because of the inefficient lymphatic drainage.[77, 79] A similar approach has been also adopted in targeting atherosclerotic plaques and the hyper-permeable vascular network in the inflammatory bowel disease.[78, 80]

Traditionally, *in vitro* models such as the Boyden chamber and *in vivo* experiments have been used to assess the transport properties of macromolecules and nanoconstructs. However, trans-well membrane system (Boyden chamber) cannot replicate the complex *in vivo* tri-dimensional cell

organization and flow conditions.[81] Animal models also present well-known ethical and technical limitations.[82] More recently, researchers have been generating functional, endothelial networks within microfluidic devices in order to accurately and effectively, study the transport of macromolecules and nanoconstructs under different controlled conditions.[83-90] However, most vascular systems developed so far comprise of large channels, with a characteristic size much larger than 100 μm, which are well above that of arterioles and capillaries[84]. Also, microchannels formed in tridimensional gels upon the spontaneous organization of endothelial cells sufferfrom poor geometrical control and stability over time.[40, 91] Indeed, these systems could be thought of as more authentic representations of a microvascular network, but the lack of control on geometry, and therefore flow, limits their use in systematic analyses. Furthermore, microfluidic systems have been realized with vertically arranged channels replicating a trans-well system. However, in general, these systems cannot be efficiently used to quantify vascular permeability of molecules and nanoparticles because transport occurs across different optical planes. [88, 92-94]

In this work, the vascular permeability of macromolecules and polymeric nanoconstructs, both rigid and deformable, was analyzed utilizing a tridimensional model of a human microvessel. This was realized in a so-called double-channel microfluidic device where the vascular compartment and the extravascular chamber lay on the same geometric plane. Cyclic adenosine monophosphate (cAMP), Mannitol and Lexiscan were employed to modulate the vascular permeability from physiological to pathological conditions, demonstrating the full potential of the system. After assessing the integrity of the vascular endothelial barrier against the FITC-fluorescent Dextran macromolecules (250 kDa), the microfluidic device was employed to study the vascular transport,

adhesion and permeability of 200 nm nanoparticles and 1,000 × 400 nm discoidal polymeric nanoconstructs.

2.2 Materials and Methods

2.2.1 Chemicals, reagents, and cells

The following chemicals and reagents were used for the fabrication of the microfluidic chip: AZ5214E positive photoresist and the corresponding solvent AZ726MF from Microchem (Italy), Chrome etch 18 from OrganoSpezialChemie GmbH (Germany), N-Methyl-2-pyridone from Sigma-Aldrich (Italy) as PG Remover and 1H,1H,2H,2H-Perfluoro-octyltrichloro-silane, 97% from Alfa Aesar (Germany). For the lithographic process, the following materials were employed: a laser-writing machine (DLW6000), an ICP-RIE (Si 500, Sentech Instruments GmbH, Germany) for the Bosh process and a Plasma System (Gambetti, Italy) for oxygen plasma treatment. The soft lithography process was conducted using polydimethylsiloxane (PDMS) (Sylgard 182) from Corning (Italy), glass coversheets No. 1.5H from Deckalaser and biopsy punches with OD = 1 mm from Miltex (Italy). As endothelial cell model Human Umbelical Vein Endothelial Cell (HUVEC) from PromoCell (USA) were used and cultured in endothelial growth medium according to the manufacture's guideline. [3-4,5-dimethylthiazolyl)-2,5-diphenyltetrazolium bromide] (MTT) ≥97% from Sigma-Aldrich was used for viability experiment together with a microplate reader from Tecan (CH). For integrating the vasculature on the microfluidic chip, the following reagents were used: collagen type I solution (≥95%) from bovine skin and Human Fibronectin from Sigma-Aldrich and Matrigel© High Concentration from Corning. Permeability experiment were

performed by using the following reagents and instruments: 250 kDa FITC-Dextran (0.5 µg/mL) from Sigma-Aldrich, Fluoresbrite® YO Carboxylate Microspheres 200 nm (2.27 x 10^9 particles/mL) from Polysciences (USA), a syringe pump model Harvard Pump 11 Elite from Harvard Apparatus (USA), a multirack syringe pump model 230 from Kd Scientific (USA), polyethylene tubes (BTPE-50, ID= 0.58 mm, OD=0.97 mm) from Instech Laboratories (Germany) and an epi-fluorescent inverted microscope from Leica (Germany) model Leica 6000 (objective 10x, 0.22 N.A.). For modulating the permeability of the endothelial barrier, the following reagents were used: N^6,2′-O-Dibutyryladenosine 3′,5′-cyclic monophosphate sodium salt (db-cAMP) (≥98.5%), Mannitol (≥98%) and Lexiscan (≥98%) from Sigma-Aldrich. In order to characterize the vasculature in the microfluidic device the following instruments were employed: Scanning Electron Microscope JSM-6490LV from FEI Company (USA), a Critical Point Drier (CPD) K850WM (UK) and a sputter coater model 550 from Emitech (Italy), and an A1-Nikon Confocal Microscope from Nikon Corporation (Japan). For immunofluorescence staining protocols, the following antibodies and reagents were used: PFA 4% from Santa Cruz Biotechnologies (USA), Ms anti-human VE-Cadherin (1:200), AlexaFluor 488 anti-mouse secondary antibody (1:500) from Abcam (UK), Hoechst (1 mg/mL) (1:1000) and AlexaFluor 488 Phalloidin from Invitrogen (USA).

2.2.2 Microfluidic device fabrication

Double-channel microfluidic device was fabricated *via* two lithographic steps, as previously reported by the authors with some modifications [95]. Briefly, using a laser-writing machine, a negative optical mask for the two-parallel channels and a positive optical mask for the micropillars

membrane were realized. In the first step, the AZ5214E photoresist was used as a positive photoresist and spin-coated at 4,000 rpm on a Cr surface. The sample was then baked a 110 °C for 60 s to clean the resist. The mask including the micropillars was impressed using a mask-aligner on the resist at 80 mJ. To develop the resist, the solvent AZ726MF was used. The impressed pattern was transferred from the resist to the Cr mask by using a Cr etchant. The residual resist layer was then removed from the unexposed surface via PG remover at 80°C for five minutes and a cleaning step procedure with ultrapure water. An ICP-RIE Bosh process was performed to dig the micropillar membrane over the Si etching down by 5 μm. The obtained Si wafer with the impressed micropillar membrane was used in the second step in order to transfer the channels. In this second step, the AZ5214E was used as negative photoresist. AZ5214E was spin-coated on the residual Cr layer and baked at 110°C for 60 s. Subsequently, the channels mask was aligned on the micropillar membrane and then exposed at 95 mJ. Because the resist was used in the reversal mode, the wafer required an additional baking phase at 120°C for 120 s and an exposure phase at 300 mJ. The development was performed as for the micropillars. A second ICP-RIE Bosh etching was performed down to 50 μm, the actual andfinal height of the channels, in order to get both pillars and channels on the Si layer. At the end of the lithographic process, the silicon template was covered with a layer of silanes by using a desiccator for 1h. The PDMS replica were obtained by mixing base and curing agent in a ratio 1:10 (w/w). The PDMS solution was casted on the silicon template, degassed until all bubbles were removed and cured at 80°C overnight. The PDMS replicas were cleaned with a scotch-tape and inlet and outlet ports were created with a biopsy punch. Before bonding the PDMS to a glass coversheet, the PDMS replicas were autoclaved (dry autoclave) and dried at 80°C for 4h. In addition, also the glass cover sheets were autoclaved and dried in order to get the same temperature of PDMS replicas and prevent collapse of the

micropillars structure during the bonding step. Oxygen (O_2) plasma treatment (pressure = 1.0 mbar, power = 20 W, time = 20 s) was performed and PDMS replicas were bonded to the glass coversheets. The obtained microfluidic chip had a rectangular cross section of 210 μm (width), a height of 50 μm and a port-to-port length of 2.7 cm. The micropillar membrane, positioned in the middle part of the channels, had a length of 500 μm and a width of 25 μm, with a gap-size between pillars of 3 μm.

2.2.3 Extracellular matrix realization

To mimic the extravascular space, different extracellular matrices (ECM) were realized by mixing increasing amount (vol/vol) of Matrigel with a solution of type I collagen. Starting from a stock solution of collagen type I (6 mg/mL), a final collagen concentration of 2 mg/mL was obtained by using deionized water, 10x EMEM, HEPES buffer 1M and 1M NaOH solution. Seven different types of ECM were prepared, starting from 100% of collagen type I and then adding increasing volumes of Matrigel© (i.e., 10, 20, 30, 50, 95%) up to 100% of Matrigel©. During the matrix manufacturing process, all components were kept at 4˚C to avoid matrix polymerization. In order to characterize the ultrastructure, the obtained composite matrices were placed in a petri dish and allowed to polymerize in an incubator for at least 30 min (37°C, > 95% humidity).

Extracellular matrix characterization: Scanning Electron Microscopy (SEM). Matrix ultrastructure was analyzed using a scanning electron microscope. Samples of the selected matrix composition were fixed in 2% glutaraldehyde in 0.1M sodium cacodylate buffer, pH 7.3 for 2

hours at room temperature, and then post-fixed in 1% OsO_4 phosphate buffer for two hours. Then, samples were dehydrated through an ascending series of ethanol solutions (30 up to 100%), and critical point dried for 1h using CO_2. The obtained matrices were sputter-coated with 10 nm of gold, and multiple images were acquired with an accelerating voltage of 10 kV and a magnification of 5,000×. To characterize the structural features of the 3D matrix network, SEM images were analyzed using the free software ImageJ. The porosity of the ECM was quantified by using three independent images from each sample, binarizing them and calculating the areas of black (pores) over the white (fibers) pixels, within the binary images.

Extracellular matrix characterization: permeability study. Microfluidic devices were autoclaved at 120°C for sterilization (wet autoclave) and then dried overnight (>15h) at 80°C. Before extracellular matrix filling, microfluidic devices were stored for 1h at 4°C. During the whole procedure, matrix solutions were kept on ice. At this point, 10 µL of the selected matrix was introduced into the extravascular channel and the loaded devices were transferred at 37°C for 30 minutes to allow matrix gelation. To characterize the transport of biomolecules within the extracellular matrix, 250 kDa FITC-Dextran (0.5 µg/mL) and Fluoresbrite® YO Carboxylate Microspheres 200 nm (2.27×10^9 particles/mL) were used. The avascular channel was connected to a syringe pump *via* polyethylene tubing. For all the experiments, the working solutions were infused in the avascular channel at a volumetric flow rate of 100 nL/min. Dextran or 200 nm beads were infused through the inlet port, allowing to fill completely the avascular channel before starting the time-lapse fluorescence acquisition (5s intervals *via* an epi-fluorescent inverted microscope). Time-lapse images were analyzed using ImageJ software, selecting Regions of Interest (ROI) in the avascular and extravascular channels. To calculate the permeability coefficient, it was assumed that the convective contribution was negligible since it was ensured no

pressure difference between the channels. Therefore, the permeability coefficient was calcuted considering solely diffusion as transport mechanism of solutes across the endothelial monolayer. In this experiment, the flux of solute across the monolayer is defined as the rate of exchange of dextran molecules or particles within the extravascular region. The concentration is therefore directly proportional to the fluorescence intensity. When the avascular channel was fully filled with the solution, the permeability coefficient *P* (µm /s) was calculated as, readapting the equation reported in [88]:

$$P = \frac{A_{ECM} . (\frac{I_{f-} I_i}{\Delta t})}{w_{pillars} . (I_{vascular} - I_{pillars})_{t=0}}$$

where A_{ECM} refers to the surface area of the ROI within the extravascular space reported in μm^2; I_f is the total fluorescence intensity of the extravascular region at the final time and I_i at t=0; $w_{pillars}$ is the width of the pillars across which diffusion occurs, expressed in µm; $I_{vascular}$ is the total fluorescence intensity of the vascular channel once completely filled and $I_{pillars}$ is the total fluorescence intensity of the interface between the vascular region and the ECM region, both at t = 0. Δt is the time interval between t = 0 and the final time of the experiment, expressed in s.

2.2.4 Vascular endothelium in the microfluidic device

To mimic the extravascular compartment, a 80% collagen type I - 20% Matrigel© matrix was selected. Next, the vascular channel was filled with 50 µg/mL of a human fibronectin solution and

incubated for 2h at 37°C. HUVEC were cultured till confluence (~80%) and then trypsinized, counted and concentrated to 5×10^6 cells/mL. Cells were used until passage 6 (P6). For complete coverage of the PDMS walls, a double seeding procedure was used. In the first step, 10 µL of cell suspension was added through the inlet port of the vascular channel and immediately the microfluidic chip was flipped facing upside-down to promote endothelial cells adhesion to the top of the channel. In this configuration, microfluidic chips were incubated at 37°C, 5% CO_2 for 1h. A second cell-seeding step was performed, without flipping the microfluidic chip, allowing the adhesion of the endothelial cells to the bottom of the channel. Devices were incubated at 37°C for 2h. Micropipette tips, filled with 200 µL of culture media, were connected to inlet ports of the vascular channel, while empty tips were placed in the corresponding outlets. The inlet and outlet ports of the extravascular channel were connected with tips filled with 50 µL of culture media. Cell culture medium was changed every 12h. HUVEC were cultured to reach confluence (approximately 2 days) in order to form a continuous monolayer before conducting permeability experiments.

db-cAMP treatment to tune the vascular permeability. In order to strengthen, the endothelial barrier, HUVEC were treated with increasing concentrations of N^6,2′-O-Dibutyryladenosine 3′,5′-cyclic monophosphate sodium salt (db-cAMP). After 2h from the cell seeding, endothelial cells were treated until confluence with 25, 50, 100 or 200 µg/mL of db-cAMP, respectively. Due to the reduced paracellular permeability observed, in the following experiments HUVEC were cultured with 25 µg/mL of db-cAMP.

Endothelial cells viability. To assess the effect of db-cAMP on HUVEC viability and proliferation, an MTT assay was performed. The assay detects the reduction of MTT by mitochondrial

dehydrogenase to blue formazan product. Briefly, 10^5 cells/well were seeded in 96-well plates and incubated at 37°C, 5% CO_2, for 24 h. Next, the medium was replaced with Endothelial Cell Growth Medium containing the corresponding concentrations of db-cAMP (25, 50, 100 and 200 µg/mL). After 24, 48 and 72 h of incubation, the MTT solution (5.0 mg/mL PBS) was diluted in Endothelial Cell Growth Medium (0.25 µg/mL), added to each well and incubated at 37°C for 4 h. The resulting formazan crystals were dissolved by adding ethanol (200 µL/well), and the absorbance was read at 570 nm using a microplate reader. Controls (i.e., cells that had received no treatment) were normalized to 100% and readings from treated cells were expressed as the percentage of viability inhibition. Five replicates were considered for each data point.

Mannitol and Lexiscan treatment to tune the vascular permeability. For modeling the opening of the vascular endothelium, Mannitol 1M was infused in the vascular channel for 5, 15 and 30 minutes after achieving cell confluence. 1µM of Lexiscan was infused into the vascular channel and permeability calculated after 5, 15, and 30 minutes of treatment. Permeability analyses were conducted as previously reported.

2.2.5 Discoidal polymeric nanoconstructs (DPN) permeability and adhesion study

Discoidal polymeric nanoconstructs (DPN) were synthesized by employing a top-down fabrication process, as already reported by the authors [96-99]. For the experiments, two types of DPN were fabricated, soft, deformable DPN (sDPN) and rigid DPN (rDPN). Briefly, a polymeric mixture composed by poly(lactic-co-glycolic acid) (PLGA) and polyethylene glycol (PEG) was casted in

the wells of the sacrificial PVA template and exposed to UV-light for polymerization. PVA templates were dissolved in water and particles collected through centrifugation. Lipid Rhodamine B (Avanti Polar Lipids, USA) was added to the polymeric paste composing the DPN for permeability experiments, while Lipid-Cy5 synthetized by the authors was used for adhesion experiments [100]. On day two post seeding, the permeability of HUVEC monolayers to both DPN configurations (500×10^6 particles/mL) was tested as reported previously. For the adhesion study, a multi-rack syringe pump was placed inside a cell incubator and loaded with 1 mL syringes. The vascular channel was perfused with sDPN and rDPN (50×10^6 particles/mL) with and without endothelial cells at 0.1 µL/min (0.2 dyne/cm^2) , 0.25 µL/min (0.7 dyne/cm^2) and 0.5 µL/min (1 dyne/cm^2), corresponding to the tumor flow rate, an intermediate flow rate and physiological flow rate, respectively.[101] Channels were then flushed with culture medium to remove non-adhering particles and fixed with 4% PFA for 15 min. Nanoconstruct adhesion was immediately investigated using an A1-Nikon confocal microscope.

2.2.6 Electron Microscopy Imaging

Vascularized microfluidic chips were imaged *via* scanning electron microscopy. Cells in the vascular channels were fixed in 2% glutaraldehyde in 0.1M sodium cacodylate buffer, pH 7.3 for 1h at room temperature. Subsequently, the PDMS chips, with endothelial cells adhered to the channel walls, were detached from the glass coversheets and post-fixed in 1% OsO_4 phosphate buffer for two hours. The samples were then dehydrated through ascending series of ethanol solutions (30% up to 100%), followed by a solution of 1:1 ethanol:hexamethyldisilazane (HMDS, ≥99% Sigma-Aldrich), and 100% HMDS and dried overnight at room temperature. The obtained

microfluidic chips were sputter-coated with 10 nm of gold and images acquired with accelerating voltage of 10 kV.

2.2.7 Cells immunofluorescence staining

Endothelialized vascular channels were fixed with 4% of PFA for 20 min at room temperature. Following fixation, channels were washed three times with cold PBS, permeabilized with a solution of Triton X 0.3% in PBS for 15 min and incubated with 20% of goat serum solution diluted in PBS for 1h at 4 °C. Endothelial Cadherins were targeted with antihuman VE-cadherin antibody overnight at 4°C with 10% of goat serum. The unbound antibody was removed with three washes of cold PBS. After that, microfluidic chips were incubated with a solution of Alexa Fluor 488 anti-mouse secondary antibody (1:500) with 10% of goat serum for 2h at 4°C. Cells were washed again three times with cold PBS and incubated with a solution of PBS and 1:1000 Hoechst for 30 min at room temperature. F-actin cytoskeleton was stained in green using Alexa Fluor™ 488 Phalloidin according to the supplier instructions. Images were acquired using an A1-Nikon confocal microscope.

2.2.8 Statistical analysis

All data are presented as the mean ± SD using GraphPad Prism5 software. Calculation of porosity was analyzed via 1-way ANOVA. p – values < 0.05 were denoted with * ,p – value < 0.01 with **. Permeability studies and DPN adhesion studies were evaluated via 2-way ANOVA analysis of variance followed by *ad hoc* Bonferroni post-test. p – values < 0.05 were denoted with *, p – values

< 0.01 with **, and p – values < 0.001 with ***. For all experiments, at least 5 independent repetitions were conducted.

2.3 Results

2.3.1 Architecture of the double-channel microfluidic device: the vascular compartment

A soft-lithographic approach was employed to create an optically-clear poly(dimethyl siloxane) (PDMS) double-channel microfluidic device (**Figure 2.1A**), following previous works by the authors. [87, 95] The microfluidic device is composed of two parallel channels interconnected in the central section via an array of micropillars, realizing a permeable membrane (**Figure 2.1B**). Specifically, this central permeable section has a characteristic length of 500 μm and an inter-pillar gap size of ~ 3 μm, as detailed by the scanning electron micrograph shown in the right inset of **Figure 2.1B**. As previously reported [87], curved pillars provide higher bending stiffness, lower adhesive interactions and smaller inter-channel separation distance. Specifically, the 10- μm wide curved pillars, laying parallel to the flow, offer higher mechanical stability. Such a configuration realizes a physical separation between the two channels supporting the identification of the two different biological compartments – the vascular and the extravascular space – without hampering the transport of molecules, nanoparticles and cells.

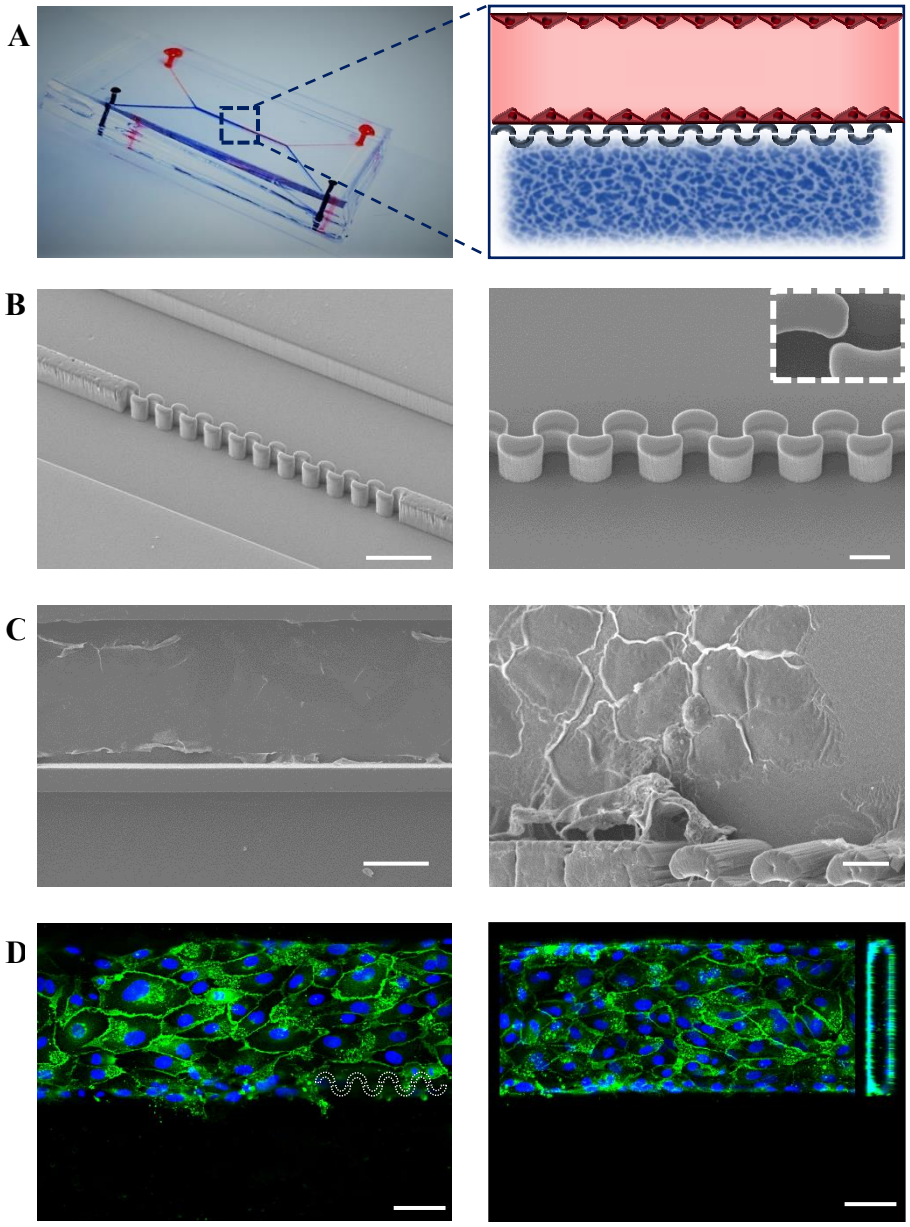

Figure 2.1. Recapitulating human vasculature in the double channel microfluidic device. A) Photograph (left) and schematic illustration of a double-channel microfluidic device with HUVEC cultured on all surfaces of the vascular channel. B) SEM images showing the double-channel microfluidic structure and the micropillars geometry (Scale bar 100 µm and 5 µm for inset on the right) . C) SEM micrographs of endothelial cells adhering to the PDMS walls (Scale bar 100 µm left image, 20 µm right image) . D) Immunofluorescence images of HUVEC barrier. In the microfluidic device nuclei (blue) and VE-cadherin (green) were stained. Cross sectional view (left) of the endothelial channel. (Scale bar = 100 µm)

To build a physiologically relevant and vascularized organ-on-chip, the upper channel was designed to accommodate endothelial cells (the vascular compartment) while the bottom channel was filled with extravascular matrix components (the extravascular compartment).

Human umbilical vein cells (HUVEC) were cultured in the vascular compartment over a fibronectin-coated PDMS surface and let to spread, grow and stably adhere, as documented in **Figure 2.1C**. Specifically, HUVEC were seeded in the upper channel after treating the PDMS surface with 50 µg/mL of human fibronectin for 2 hours.

A double-step cell seeding procedure was employed to entirely cover the walls of PDMS channel. After fibronectin coating, HUVEC were gently pipetted into the vascular channel, and the microfluidic chip was immediately flipped. In this configuration, HUVEC were left to adhere to the top surface of the channel for 1h, at 37°C. Then, the microfluidic chip was flipped again, HUVEC were pipetted into the vascular channel in order, this time, to cover the bottom surface. A detailed analysis with confocal fluorescence microscopy revealed the formation of a continuous endothelial monolayer covering the bottom, top and later walls of the vascular compartment even next to the pillar membrane (**Figure 2.1D)**. The right inset of **Figure 2.1D** also shows a lateral projection of the confocal microscopy images demonstrating that the endothelial cells uniformly coat the vascular compartment's surface along its entire rectangular cross section. Moreover, the staining of the VE-Cadherin proteins (green) demonstrates the formation of inter-endothelial cell junctions that are important regulators of vascular integrity and permeability (**Figure 2.1D**).

2.3.2 Architecture of the double-channel microfluidic device: the extravascular compartment

On the other side of the micropillar membrane, the extravascular compartment was filled with components of the extracellular matrix (ECM), including Matrigel© and Collagen type I. To finely modulate the ECM permeability, the relative ratio between the two components was varied from 100% Matrigel© (8.6 mg/mL) to 100% Collagen (2 mg/ml) realizing seven different matrix configurations (see **Table 1**).

Extracellular matrix		**Protein concentration**		
Collagen % (v/v)	Matrigel % (v/v)	Collagen [mg/mL]	Matrigel [mg/mL]	Total [mg/mL]
100%	-	2	-	2
90%	10%	1.8	0.86	2.66
80%	20%	1.6	1.72	3.32
70%	30%	1.4	2.58	3.98
50%	50%	1	4.3	5.3
5%	95%	0.1	8.17	8.27
-	100%	-	8.6	8.6

Table 1. Extracellular Matrix Characterization. Table recapitulating collagen type I and Matrigel© concentrations used for recapitulating the biologically derived matrix.

Representing scanning electron microscopy images of four matrix configurations are shown in **Figure 2.2A**, specifically for the case of 100% Collagen (**left**); 80% Collagen and 20% Matrigel©; 50% Collagen and 50% Matrigel©; 100% Matrigel© (**right**). This series of images qualitatively

shows that the progressive increase in Matrigel© content is associated with a decrease in matrix permeability.

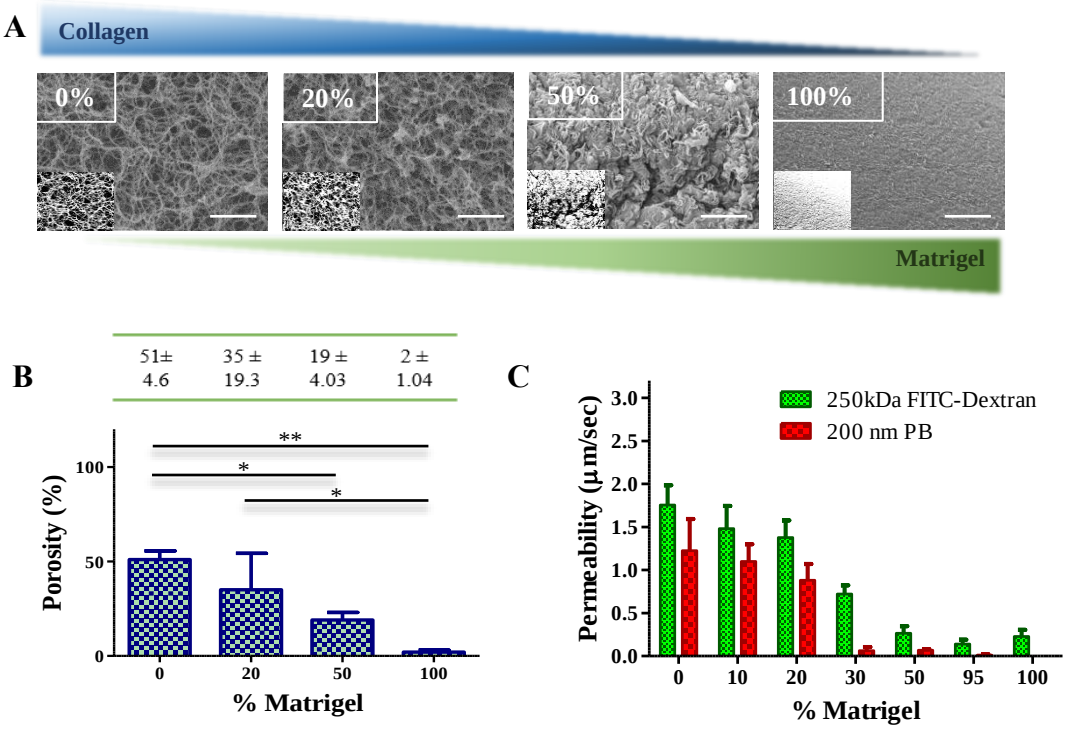

Figure 2.2. Extracellular matrix characterization. A) SEM micrographs of the extracellular matrix showing the increasing Matrigel© content and the relative porosity (Scale bar 5 µm). C) Porosity percentage was calculated via ImageJ analysis (n=3). D) Permeability of 250kDa-FITC Dextran and Microspheres 0.2 µm (n≥5).

The first image on the left, which is associated with a Collagen only matrix, shows fibrils arranged to form pores over multiple scales and certainly comparable in size to that of a cell. As the Matrigel© content increases, the Collagen fibers appear to entangle more forming denser structures. At 20% (v/v) Matrigel©, the gel is composed of thicker fibers still preserving the original porosity of the network. At 50% (v/v) Matrigel©, the collagen fibers are packed into a dense matrix with a drastically reduced network porosity as compared to the previous configurations. Finally, the image on the right, which is associated with a Matrigel© only matrix,

shows a continuous network in which individual pores and fibers cannot be distinguished anymore at the considered magnification.

The electron microscopy images were further analyzed using ImageJ to extract quantitative information on the matrix porosity (**Inset Figure 2.2A**). **Figure 2.2B** shows the porosity variation as the Matrigel© content in the extracellular matrix increases. As expected, the porosity of the hydrogel reduces from 51 ± 4.6% for a Collagen only matrix to 2 ± 1.04 % for a Matrigel© only matrix. Here it is important to highlight that SEM images, and the corresponding porosity analyses, were obtained on dehydrated matrices, as required by the imaging technique.

	250kDa FITC-Dextran	Spherical Beads 200nm
Average Diameter	12.86 ± 3.74	181.8 ± 31.33
PDI	0.2	0.186

Table 2. Summarizing average diameter and PDI for 250kDa FITC-Dextran and 200nm PB.

To investigate further the gel porosity in an actual functional assay, permeability studies were conducted on the seven matrix configurations using two different fluorescent tracers, namely the 250 kDa FITC-Dextran (green) and 200 nm polystyrene beads (red). These tracers were infused from the vascular compartment and observed as they slowly permeated the extravascular space. Dynamic Light Scattering (DLS) analyses of the two tracers returned a hydrodynamic diameter of 12.86 ± 3.74 nm for the Dextran molecules and 181 ± 31 nm for the beads (**Table 2**). The estimated permeability values are given in **Figure 2.2C** and confirm that, for both tracers, the gel permeability drops progressively with the Matrigel© content. Indeed, the permeability associated

with the larger 200 nm polystyrene beads is overall smaller than that registered for the ~ 10 nm Dextran molecules. A rapid decrease in permeability was observed between 20 and 30% of Matrigel© content. For higher Matrigel© contents, the permeability of the 200 nm polystyrene beads went to zero whereas it plateaued around ~ 0.2 μm/s for the Dextran molecules. Based on these observations and data from the current literature [90, 102], an extracellular matrix with a 20% Matrigel© content was selected for the extravascular compartment of the microfluidic chip to recapitulate the ECM composition through fibrillar collagen type I and proteins associated with Matrigel©. This matrix configuration offered a proper balance between molecule and particle permeability, while ensuring that the extravascular compartment was enriched with unique growth factors for cell culture.

2.3.3 Reducing the vascular permeability to circulating agents

The integrity of the endothelial barrier across the micropillar membrane was tested using the same two fluorescent tracers adopted for the ECM characterization. The tracers were slowly infused through the vascular compartment and their permeation into the extravascular space was assessed via fluorescent microscopy in the absence (– HUVEC) and presence (+ HUVEC) of endothelial cells. From the post-processing of the fluorescent microscopy acquisitions, it resulted that the 250 kDa FITC-Dextran molecules would readily flow across the micropillar membrane returning a permeability of 1.35 ± 0.3 μm/s. The formation of a continuous monolayer of endothelial cells (+ HUVEC) significantly reduced this permeability value to 0.93 ± 0.30 μm/s, thus confirming the presence of a functional, vascular barrier (**Figure 2.3A**).

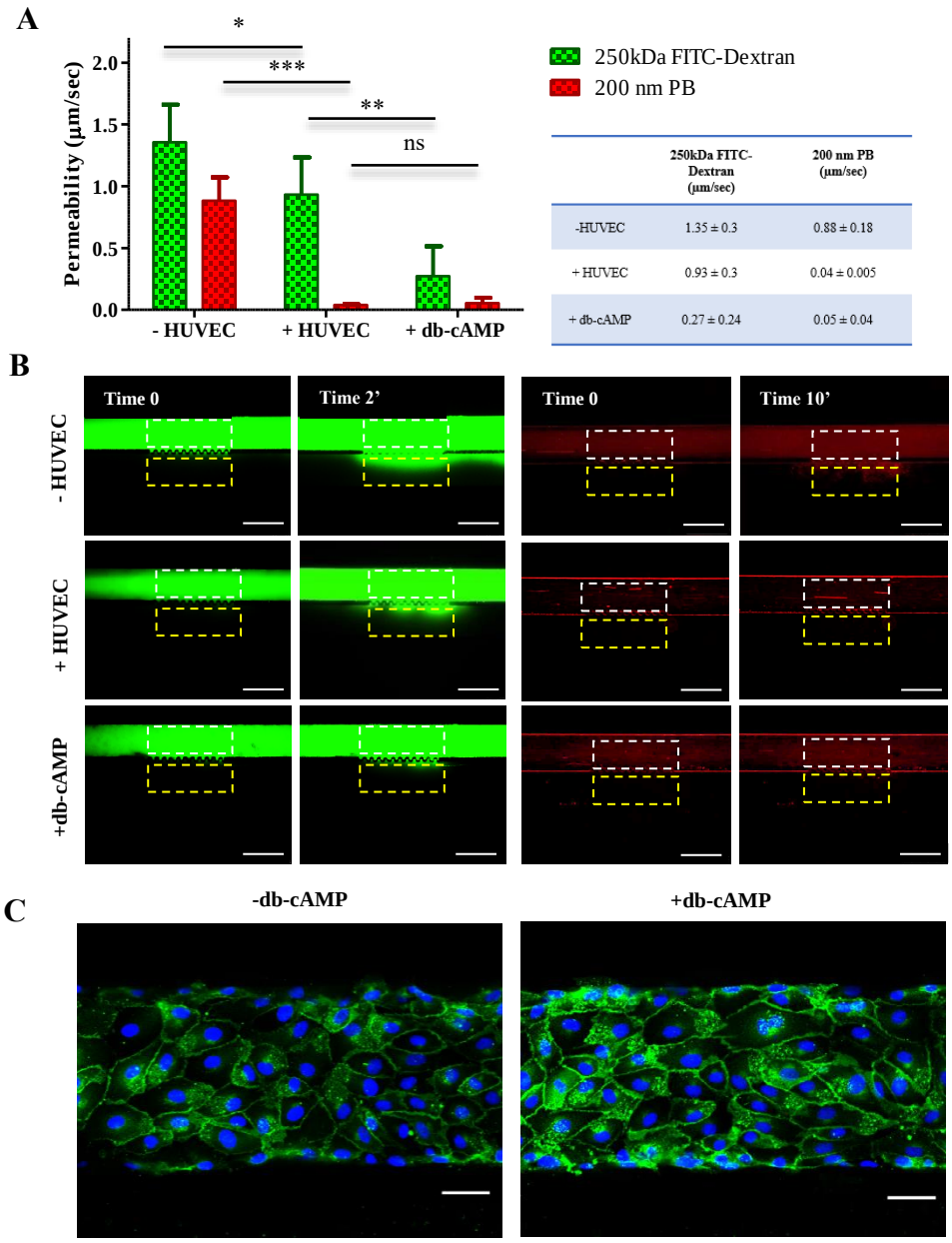

	250kDa FITC-Dextran (µm/sec)	200 nm PB (µm/sec)
-HUVEC	1.35 ± 0.3	0.88 ± 0.18
+ HUVEC	0.93 ± 0.3	0.04 ± 0.005
+ db-cAMP	0.27 ± 0.24	0.05 ± 0.04

Figure 2.3. Strengthening of endothelial barrier. A) Permeability coefficients calculated for 250kDa-FITC Dextran and Microspheres 0.2 µm on microfluidic chip without HUVEC (-HUVEC), on endothelialized microfluidic chip (+ HUVEC) and on endothelialized chip treated with 25 µg/mL of db-cAMP (+db-cAMP) (n≥5). B) Representative fluorescence images of Dextran (left) and Spherical beads (right) diffusion at 0.1 µL/min without endothelial cells (- HUVEC), with untreated endothelium (+ HUVEC) and with db-cAMP at a concentration of 25 µg/mL (Scale bar 250 µm) . C) Immunofluorescence images of human umbilical vein endothelial cells (HUVEC) with and without db-cAMP expressing VE-Cadherin (green). Scale bar 50 µm.

For the 200 nm beads, the permeability value in the absence of HUVEC was 0.88 ± 0.18 µm/s and reduced dramatically to 0.04 ± 0.005 µm/s in the presence of HUVEC (**Figure 2.3A**). Importantly, in the absence of HUVEC, the permeability of the Dextran molecules and 200 nm beads into the extravascular space werecomparable. However, the addition of HUVEC induced a much larger decrease in permeability for the 200 nm beads as opposed to the 10 nm macromolecules, resulting in a 30% vs 95% reduction, respectively. This demonstrated the size-dependent selectivity of the micropillar membrane.

To further modulate the permeability of the endothelial layer, cells were treated with Dibutyryl-cAMP (db-cAMP). This is an activator of cAMP-dependent protein kinases that is known to reduce vascular permeability by inducing changes in the endothelial cell-cell junctional proteins, like VE-cadherin [103]. Endothelial cells were treated with db-cAMP, ranging from 25 to 200 µg/mL, and tested for the permeability to 250 kDa FITC-Dextran molecules.

A 3-fold decrease in permeability was observed already at 25 µg/mL db-cAMP, from 0.93 ± 0.30 to 0.27 ± 0.24 µm/s (**Figure 2.4A**). Similar permeability values were reported at higher db-cAMP concentrations (**Figure 2.4A**). Moreover, cell viability studies showed that treating endothelial cells with 25 µg/mL db-cAMP did not induce any significant toxicity up to 72h. On the other hand, some moderate toxicity returning a cell viability of ~ 70% was documented at the higher db-cAMP concentrations and longer incubation times **Figure 2.4B**). For this reason, all the experiments were conducted by culturing endothelial cells with 25 µg/mL db-cAMP. Note also that, not surprisingly, the reduction in permeability observed for the ~ 10 nm FITC-Dextran molecules was not recapitulated for the larger 200 nm polystyrene beads. For these larger agents, a dramatic reduction in vascular permeability was already documented with the sole addition of the HUVEC. The pre-

treatment with 25 µg/mL db-cAMP returned a permeability of 0.05 ± 0.04 µm/s, which was statistically similar to the untreated case (0.04 ± 0.005 µm/sec – p = 0.6890).

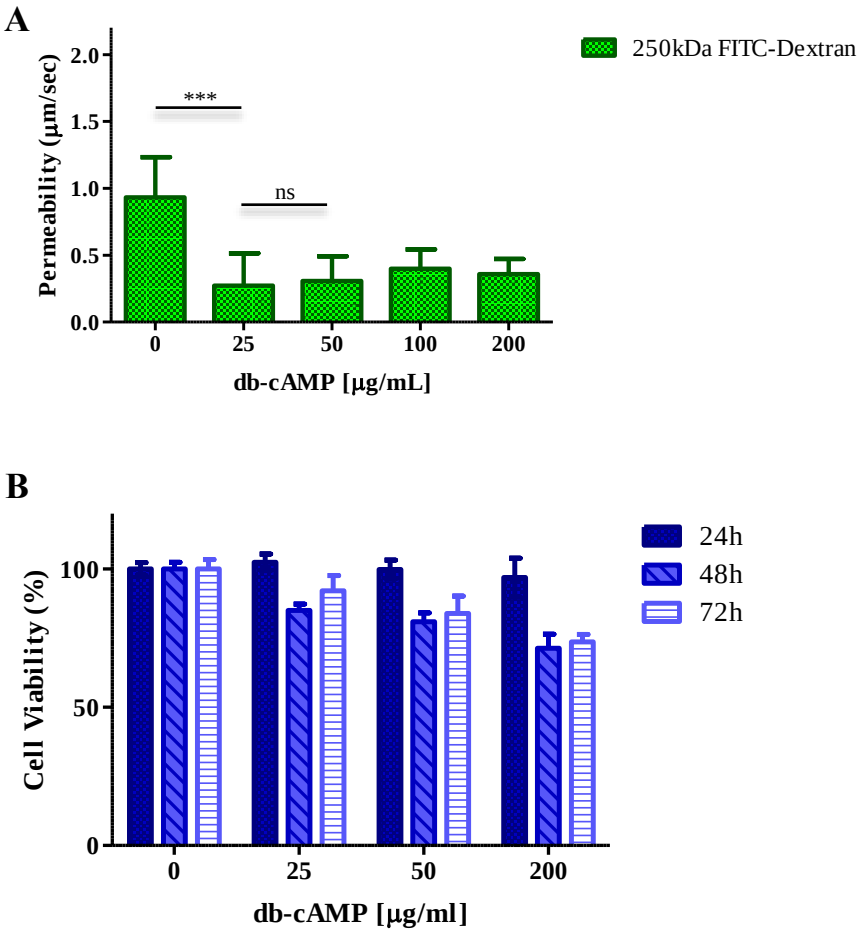

Figure 2.4. db-cAMP treatment on endothelial cells. A) Permeability coefficient for 250kDa-FITC Dextran after treatment of endothelial monolayer with different concentration of db-cAMP. (n≥5). B) Cell viability of HUVEC over 72h with increasing concentration of db-cAMP. (n=10).

Confocal images of endothelial cells treated with 25 µg/mL of db-cAMP documented a higher density of VE-cadherin proteins (green) as compared to the untreated case (**Figure 2.3C**), further confirming the generation of tighter inter-endothelial bonds.

2.3.4 Increasing the vascular permeability to circulating agents

In drug delivery and biomedical imaging, the transient and reversible opening of the blood vessel walls is key to support the accumulation of molecules and nanocarriers in the diseased tissue. Therefore, to further characterize the functionality of the vascular endothelium in the microfluidic chip, two different permeation enhancers were considered, namely Mannitol and Lexiscan.

The first agent, Mannitol, is clinically used to reduce excessive intra-tissue pressure, especially in the brain as its application causes an osmotic shrinkage of the endothelial cells and enhances the BBB permeability.[104] In accordance with other studies, a 1M Mannitol solution was infused into the vascular compartment under physiological conditions (37°C, 5% CO_2, > 95% of humidity) for 5, 15 and 30 minutes. Then, the permeability of the endothelial layer was assessed, following the same protocol described above, by infusing 250 kDa FITC-Dextran molecules and 200 nm polystyrene beads at 0.1 µL/min (**Figure 2.5A**).

The osmotic opening of the endothelial layer resulted in an increased, time-dependent extravascular accumulation for both 250 kDa FITC-Dextran molecules and 200 nm beads. For the Dextran molecules, the permeability values (+ HUVEC and +db-cAMP) increased from 0.27 ± 0.24 to 0.56 ± 0.10 µm/s, to 0.78 ± 0.09 µm/s and 0.99 ± 0.06 µm/s after 5, 15 and 30 minutes of continuous infusion of mannitol, respectively (**Figure 2.5A**). A 30-minutes treatment with Mannitol increased the permeability by over 3 times. Notice that in the absence of HUVEC, the permeability of Dextran was equal to 1.37 ± 0.2 µm/s indicating that the Mannitol treatment was almost equivalent to transiently removing the endothelial layer. For the 200 nm beads, the permeability values (+ HUVEC and +db-cAMP) increased from 0.029 ± 0.01 to 0.06 ± 0.02 µm/sec, 0.15 ± 0.01 µm/s and 0.20 ± 0.006 µm/s after 5, 10 and 30 minutes of mannitol treatment,

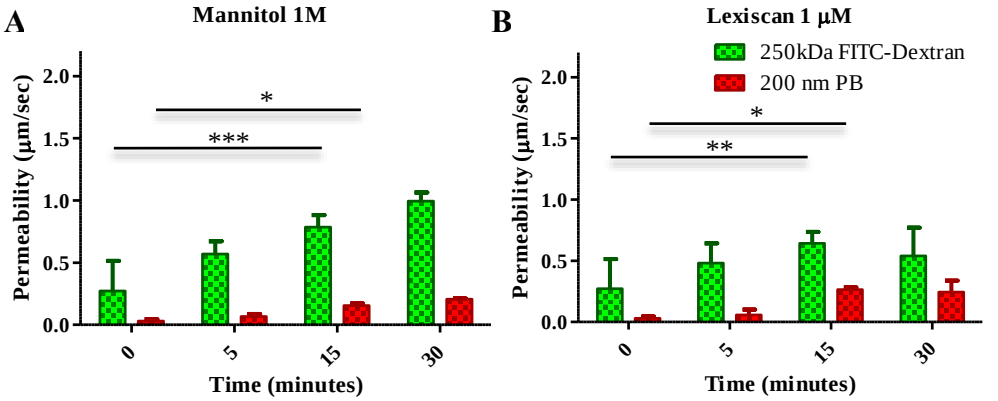

Time (minutes)	Mannitol 1M		Lexiscan 1µM	
	250kDa FITC-Dextran (µm/sec)	200 nm PB (µm/sec)	250kDa FITC-Dextran (µm/sec)	200nm PB (µm/sec)
0	0.27 ± 0.24	0.02 ± 0.01	0.27 ± 0.24	0.02 ± 0.01
5	0.56 ± 0.10	0.06 ± 0.02	0.48 ± 0.16	0.05 ± 0.04
15	0.78 ± 0.09	0.15 ± 0.01	0.64 ± 0.09	0.26 ± 0.01
30	0.99 ± 0.06	0.2 ± 0.006	0.54 ± 0.23	0.24 ± 0.09

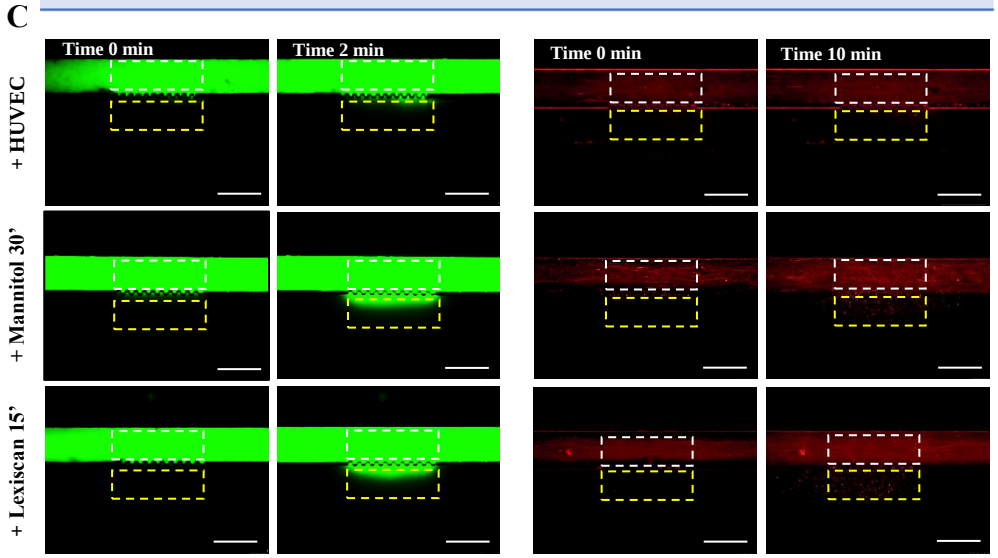

Figure 2.5. Modulation of Vascular Permeability. Endothelial barrier integrity under hyperosmotic conditions (A) and under Lexiscan treatment (B) monitored by measuring permeability coefficient via fluorescence microscopy (n≥5). Representative fluorescence images of Dextran (left) and 200nm Polystyrene Beads (right) diffusion at 0.1 µL/min with untreated HUVEC, after 30 minutes treatment of Mannitol and after 15 minutes treatment of Lexiscan (Scale bar 250 µm).

respectively (**Figure 2.5A**). This resulted in a 10-fold increase in the accumulation of 200 nm beads into the extravascular compartment (**Figure 2.5C**).

Despite multiple successes with mannitol, the non-uniform effect among different brain regions and negative side effects (e.g., epileptic seizure) has limited the clinical application of this procedure. [105] A more recent approach is based on the manipulation of the Adenosine Receptors (AR) using the FDA-approved A_{2A} AR agonist (Lexiscan®). As with Mannitol, Lexiscan

modulates cytoskeletal organization reflecting a down-regulation of both adherent and tight junctions. [106, 107]

In the proposed microfluidic device, a Lexiscan treatment (1 μM) was conducted as per the Mannitol. For 250 kDa FITC-Dextran, a plateau in permeability was reached already at 15 min of treatment returning a value of 0.64 ± 0.09 μm/s. At 30 minute of treatment, the permeability slightly but not significantly decreased down to 0.54 ± 0.23 μm/s ($p = 0.5124$) (**Figure 2.5B**). Thus, for dextran macromolecules, the infusion of Lexiscan induced an overall 2-fold increase in vascular permeability. A similar trend was also observed for the 200 nm beads for which a plateau was reached after 15 minutes of treatment with a permeability value of 0.24 ± 0.01 μm/s (**Figure 2.5B**). No change in permeability was documented at the longer treatment time of 30 minutes. However, differently from the 250 kDa FITC-Dextran, this was still sufficient to realize a 10-fold increase in vascular permeability. Indeed, no significant statistical difference was observed in terms of enhanced permeabilization for the 200 nm beads with Lexiscan or Mannitol.

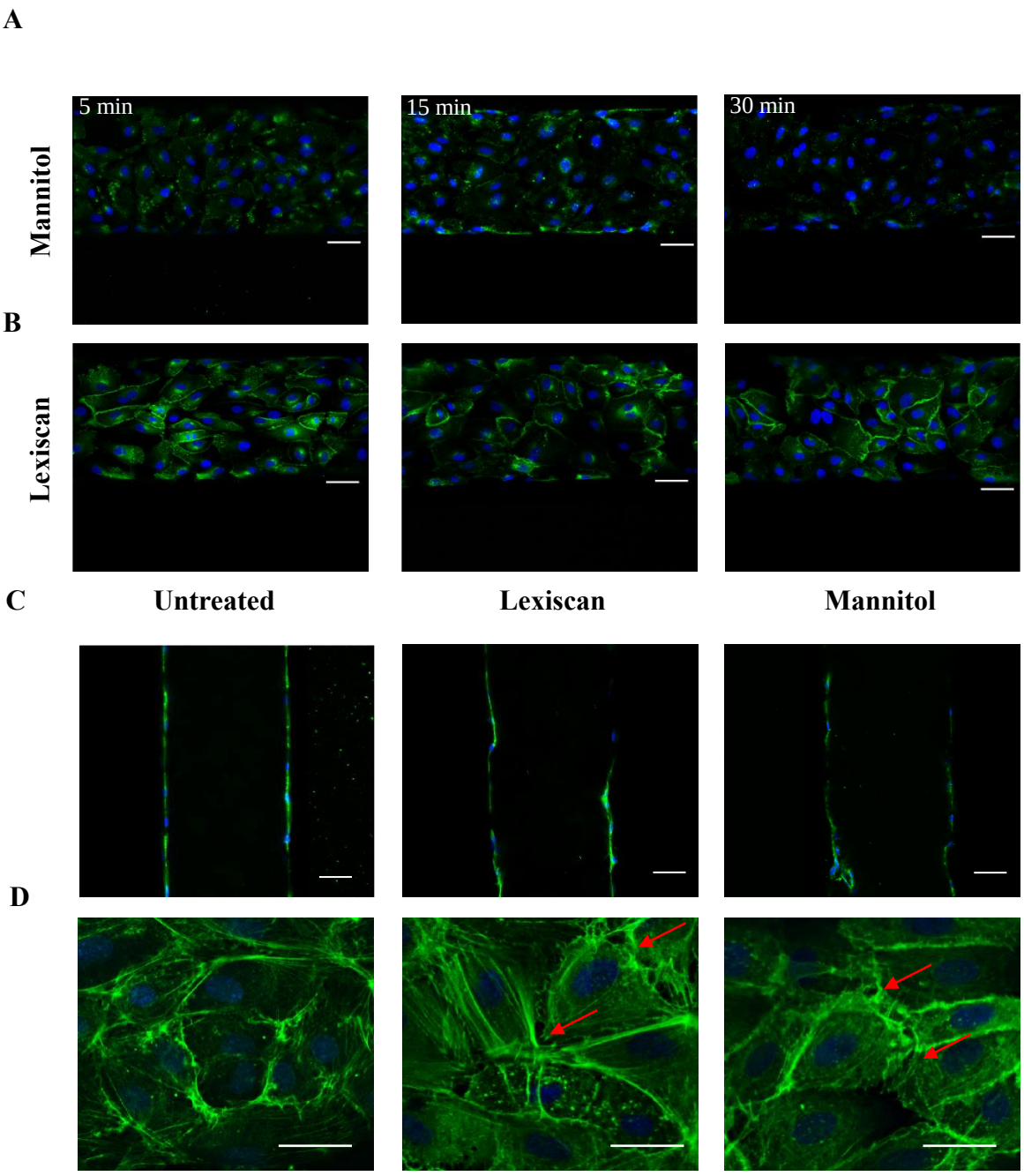

Figure 2.6. Remodeling of AJs. Immunofluorescence images of endothelial adherent junctions remodeling after treatment with A) 1M Mannitol and B) 1µM Lexiscan overtime. VE-cadherin are stained in green. Scale bar 50 µm. C) Cross sectional view of endothelial vascular channel and remodeling after vascular opening. Scale bars 50 µm. D) Actin remodeling (in green). Scale bars 25 µm.

The effect of the two vascular permeabilizers on the expression of VE-Cadherins and the organization of the actin cytoskeleton was then analyzed. The exposure of endothelial cells to hyperosmotic agents – Mannitol – resulted in the detachment of adjacent cells as documented by the drop in VE-cadherin expression after just 5 minutes of treatment (**Figure 2.6A**).

A similar behavior was also documented with Lexiscan (**Figure 2.6B**). However, in the case of Lexiscan, the opening of endothelial barrier was reversible and at 30 minutes of treatment, VE-Cadherin proteins started to appear again on the cell membrane and reassemble to form new intracellular bonds (**Figure 2.6B**). These results confirmed the enhanced paracellular permeability observed within the first minutes of Lexiscan treatment but also document the reversibility of the process.

2.3.5 Assessing the vascular dynamics of circulating polymeric nanoconstructs

The proposed microfluidic device was used to study the transport of blood-borne nano- and micro-particles from the vascular to the extravascular compartments. In this context, three different types of particles were tested and compared: 200 nm polystyrene beads (PB), soft discoidal polymeric nanoconstructs (sDPN), and rigid discoidal polymeric nanoconstructs (rDPN). DPN are disc shaped nanoconstructs, with a 1,000 nm diameter and 400 nm height, and were fabricated following a soft lithography templating technique (**Figure 2.7A-B**).[96-99]

These particles resulted from mixing together the biocompatible and biodegradable polymers, poly (lactic-co-glycoli acid) (PLGA) and polyethyleneglycol diacrylate (PEG-DA). Previous studies have shown that the mechanical stiffness of these particles could be modulated by tailoring the content of PEG-DA in the formulation. [97]

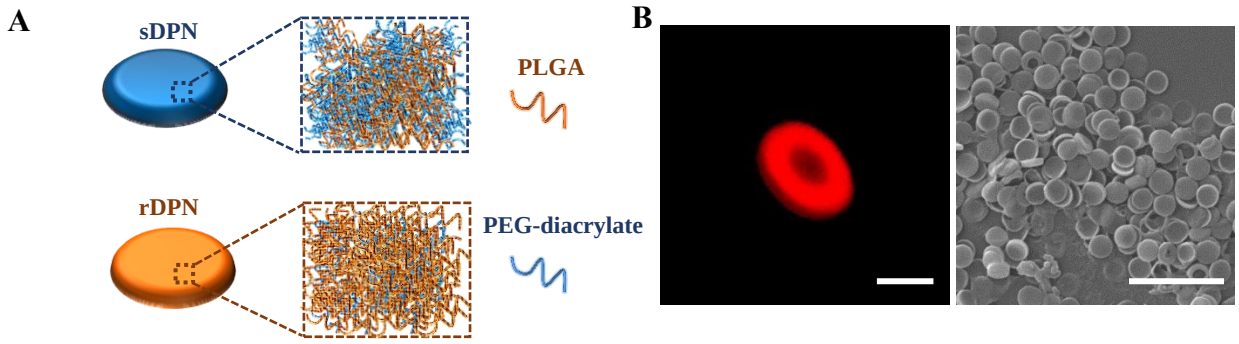

Figure 2.7. Polymeric Nanoconstructs. A) Schematic illustration of sDPN (blue) and rDPN (orange). (B) Confocal image (left) and SEM micrograph (right) showing DPN geometry (Scale bar 5 µm).

First, vascular permeability experiments were carried out with soft and rigid DPN under low flow conditions. Both sDPN and rDPN were not able to cross the endothelial layer, even following Mannitol or Lexiscan treatment (**Figure 2.8A**).

Specifically, in the absence of HUVEC, the permeability values were equal to 0.019 ± 0.002 μm/sec and 0.014 ± 0.001 μm/sec ($p = 0.595$) for the sDPN and rDPN, respectively. After the inclusion of endothelial cells, the vascular permeability reduced further falling in the range of 0.007 ± 0.001 μm/sec, with no significant difference between the two nanoconstructs. Treatments with Mannitol and Lexiscan did not enhance the permeation of DPN. In addition, the 200 nm PB beads generally returned a vascular permeability about two orders of magnitude higher than that observed for DPN under all the tested conditions. Representative images for the different tested conditions are provided in **Figure 2.8B-D**. Indeed, the permeability values documented in **Figure 2.8A** were expected given the size of the discoidal nanoconstructs, which have been designed to target the malignant vasculature rather than extravasating at sites of vascular hyperpermeability. [96, 99]

Then, vascular adhesion experiments were performed under three different conditions: a low capillary flow condition (low flow), which is characterized by a flow rate of 0.1 μL/min (wall shear stress ~ 0.03 Pa; average velocity ~ 0.2 mm/s) as opposed to a physiological capillary flow condition (physiological flow), which is characterized by a flow rate of 0.5 μL/min (wall shear stress ~ 0.15 Pa; average velocity of ~ 1 mm/s); and an intermediate flow condition characterized by a flow rate of 0.25 μL/min (wall shear stress ~ 0.071 Pa; average velocity ~ 500 μm/s).

A

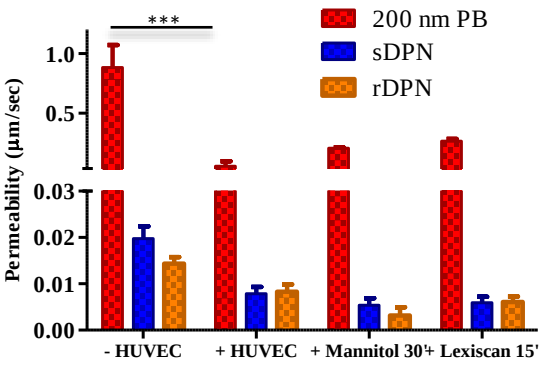

	200 nm PB (µm/sec)	sDPN (µm/sec)	rDPN (µm/sec)
-HUVEC	0.88 ± 0.18	0.019 ± 0.002	0.014 ± 0.001
+ HUVEC	0.05 ± 0.04	0.007 ± 0.001	0.008 ± 0.001
+ Mannitol	0.2 ± 0.006	0.005 ± 0.004	0.003 ± 0.002
+ Lexiscan	0.26 ± 0.01	0.005 ± 0.003	0.006 ± 0.001

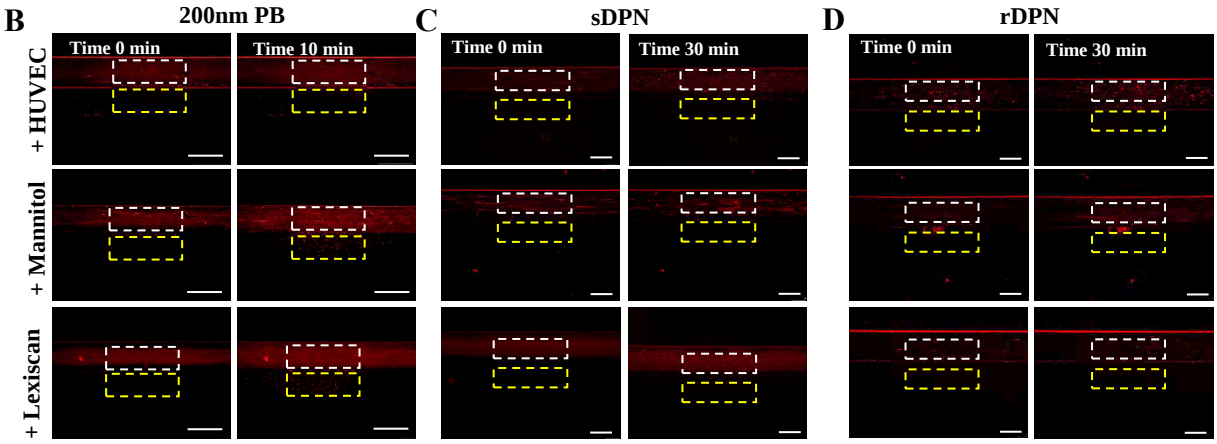

Figure 2.8. Permeability of Polymeric Nanoconstructs. A) Permeability coefficient and endothelial modulation for 200nm Polystyrene Beads, sDPN and rDPN ($n \geq 5$). $p<0.001$ denoted with ***. B) Representative fluorescence images of 200nm Polystyrene Beads diffusion at 0.1 µL/min with untreated HUVEC, after 30 minutes treatment of Mannitol and after 15 minutes treatment of Lexiscan (Scale bar 250 µm). C) Representative fluorescence images of sDPN (left) and D) rDPN (right) diffusion at 0.1 µL/min with untreated HUVEC, after 30 minutes treatment of Mannitol and after 15 minutes treatment of Lexiscan (Scale bar 250 µm).

Interestingly in the absence of HUVEC, DPN appeared to be attracted and entrapped at the micro-pillar membrane rather than adhering on the fibronectin-coated PDMS of the main channel (**Figure 2.9A** sDPN – **top row**; rDPN – **bottom row**).

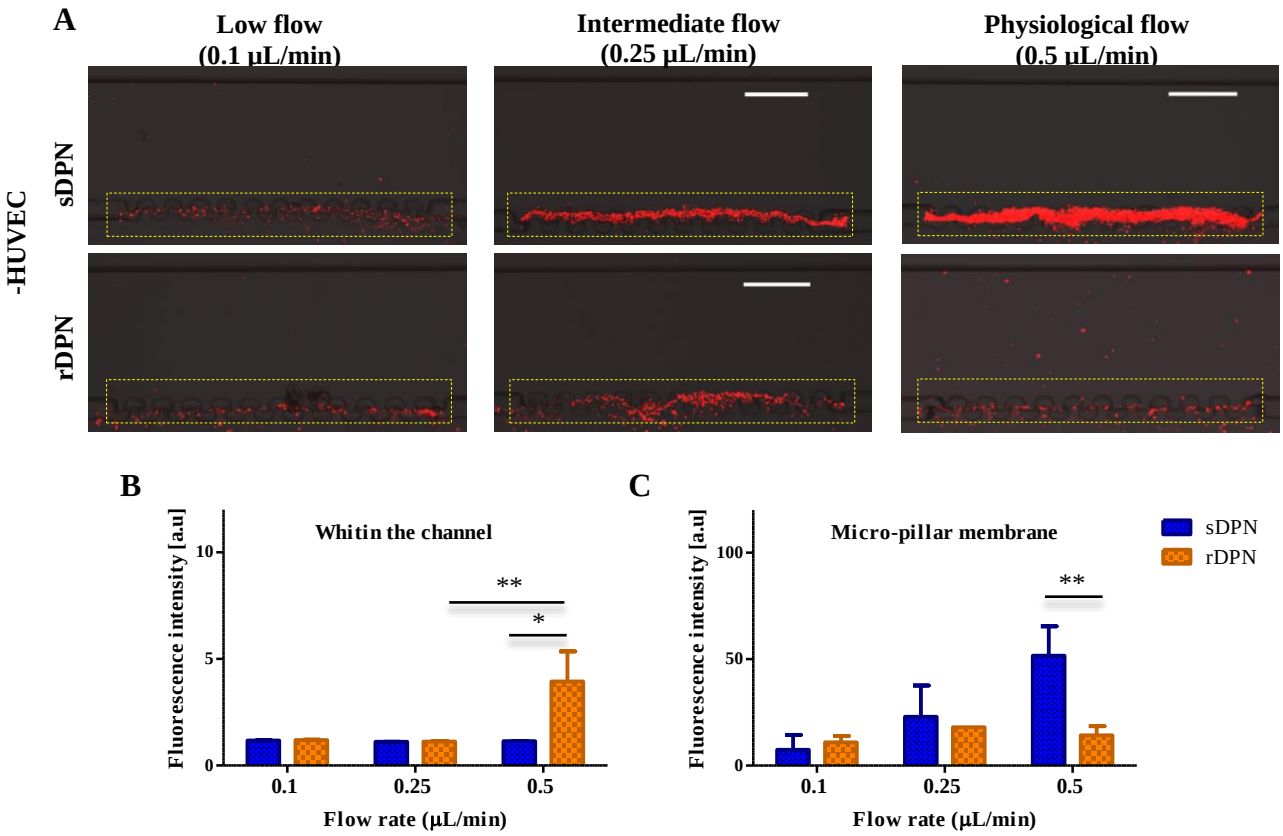

Figure 2.9. Adhesion of DPN. A) Representative confocal fluorescence images of sDPN, rDPN labeled with Cy5 adhering to the PDMS walls without HUVEC under tumor flow condition, intermediate and physiological flow condition(Scale bar 100 µm). B) Adhesion of sDPN and rDPN within the channel under different flow conditions in the absence of the endothelial layer ($n \geq 3$). C) Adhesion of sDPN and rDPN at the micropillar mebrane under different flow conditions in the absence of the endothelial layer ($n \geq 3$).

Note that the matrix filling the extravascular compartment would favor the formation of 'openings', similar to fenestrations in a malignant vasculature, at the micro-pillar interface where DPN could be trapped. The number of entrapped DPN increased with the flow rate for both the

soft and rigid configurations. However, the soft DPN showed a stronger tendency than the rigid DPN to be entrapped at the micro-pillar interface forming almost a continuous layer of particles at the highest flow rates (**Figure 2.9A**). The bars in the chart of **Figure 2.9B-C** return the amounts of adherent DPN, expressed in terms of fluorescent intensity, within the channel and at the micro-pillar interface, respectively, for the different tested flow rates.

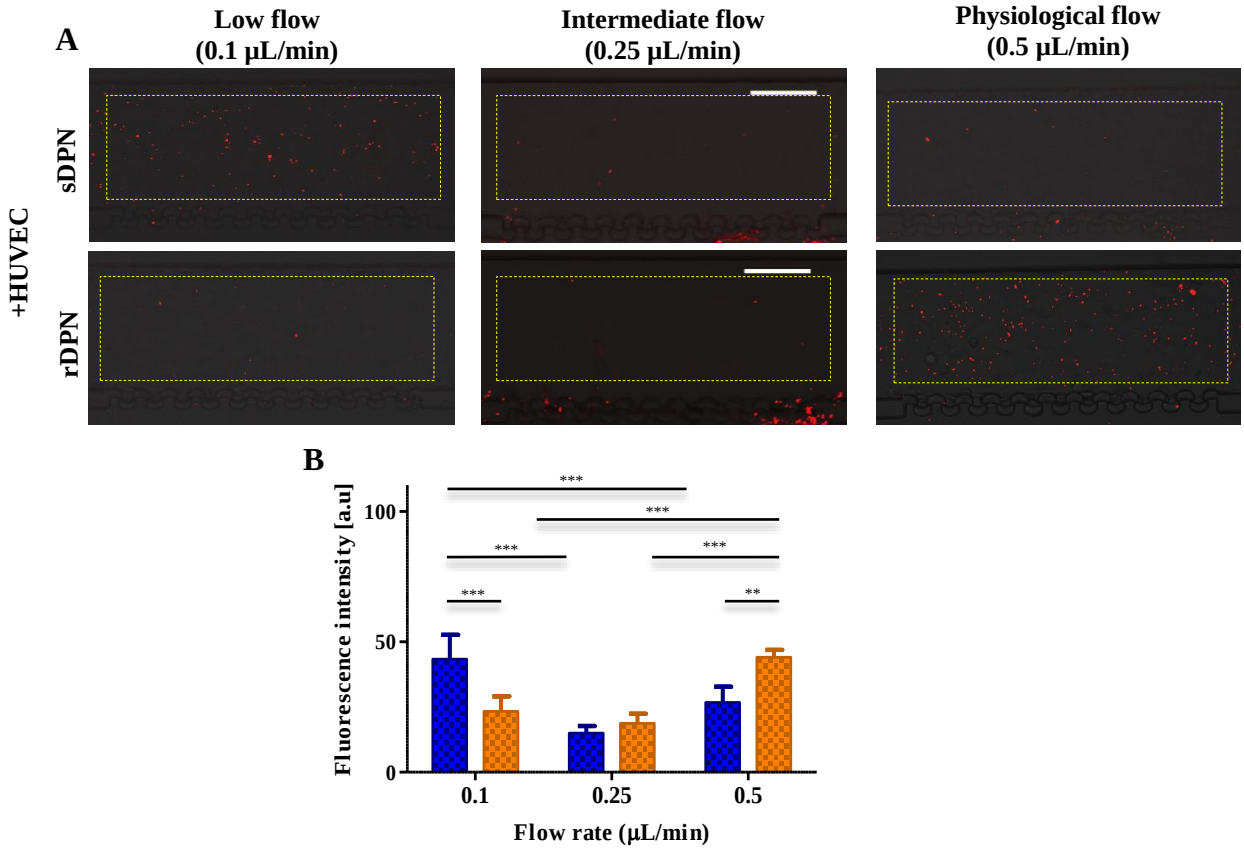

Figure 2.10. Adhesion of DPN to the endothelium. A) Representative confocal images of sDPN and rDPN labeled with Cy5 adhering to the endothelial layer under tumor, intermediate and physiological flow conditions. B) Adhesion of sDPN and rDPN to the endothelial layer under different flow conditions ($n \geq 6$). $p < 0.05$ denoted with *, $p < 0.01$ denoted with **, $p < 0.001$ denoted with ***.

In the presence of endothelial cells, a different behavior was observed. Under this condition, the micro-pillar membrane was no more an attractor for DPN as the vascular cells would prevent the formation of openings. Adhesion within the channel on the HUVEC was instead preferred by DPN (**Figure 2.10A,** sDPN – **top row**; rDPN – **bottom row**).

Interestingly, the soft DPN were observed to adhere at low flow rates more than rigid DPN. The opposite trend was instead observed at the higher flow rates. This is summarized in the bar chart of **Figure 2.10B**. Under low flow conditions, a fluorescence intensity value equal to 43 ± 9.35 AU was measured for sDPN as opposed to 23 ± 5.77 AU for rDPN ($p = 0.0006$). Under physiological flow conditions, adhering rDPN were associated to a fluorescence intensity of 44 ± 2.8 AU while for the sDPN the value was almost two times lower 26 ± 6.0 AU ($p = 0.004$) (**Figure 2.10B**). Under intermediate flow conditions, sDPNand rDPN displayed no difference in vascular adhesion documenting a smooth transition from low to high flow rate conditions.

2.4 Discussion

In drug delivery and biomedical imaging, systemically administered molecules and nanomedicines must either escape the vascular compartment and distribute within the diseased tissue (tissue targeting) or firmly adhere to the diseased vasculature (vascular targeting) in order to properly exert their curative and diagnostic functions. This process is strictly regulated by several factors including the local hydrodynamic conditions and vascular permeability. As such, assessing the efficacy of drug delivery systems *in vitro* requires the design and realization of microfluidic devices where flow rates and vascular permeability can be accurately and independently

modulated reproducing physiological and pathological conditions. This need has inspired the engineering of a double-channel microfluidic device (**Figure 2.1**) that integrated a vascular compartment and an extravascular chamber. The vascular compartment, with a width of 200 μm and a height of 50 μm, matched the characteristic dimensions of arterioles and large capillaries and was coated by endothelial cells [108, 109]. The extracellular matrix underlying the vascular endothelium provides simultaneously a mechanical function, supporting the blood vessel walls, and a biological function, mediating signals involved in endothelial cell proliferation, migration, morphogenesis, survival, and angiogenesis. This is achieved by multiple properly mixed components, including collagen I, III and IV, different laminin types, perlecan and other less abundant proteins and fibers. Matrigel© is rich in laminin, collagen type IV, and perlecan, thus approximating the composition of the vascular basement membrane. This observation triggered the realization of a biologically inspired ECM composed of collegen type I and Matrigel© **(Figure 2.2)** [110, 111]. Seven different collagen/Matrigel© combinations were considered and characterized for their permeability, as documented in **Figure 2**. The combination 80% of collagen and 20% of Matrigel© returned physiologically relevant permeabilities to 250 kDa FITC-Dextran molecules. Higher Matrigel© concentrations were excessively impermeable to molecules and cells, whereas a 100% collagen type I matrix would have lacked collagen type IV, laminin and other fiber and proteins that are contained in Matrigel© as well as in the vascular basement membrane.

With such a system, first, the formation of a continuous endothelial barrier in the vascular compartment was assessed using electron microscopy, to demonstrate the assembly of a confluent

endothelial barrier (**Figure 2.1C**); confocal fluorescent microscopy, to document the expression of VE-cadherin molecules (**Figure 2.1D and Figure 2.6**); and dynamic assays to quantify the vascular permeability of 250 kDa Dextran molecules and 200 nm polystyrene beads (**Figure 2.2C**). The proper deposition and culturing of HUVEC within the microfluidic device prompted the formation of a continuous endothelial layer on the micro-pillar membrane leading to permeability values as low as 0.93 ± 0.30 μm/s for the 250 kDa Dextran molecules and 0.04 ± 0.005 μm/s for the larger 200 nm polystyrene beads. The vascular permeability for the macromolecules (250 kDa Dextran molecules ~ 10 nm particles) was further reduced to 0.27 ± 0.24 μm/s upon exposing the endothelial cells to db-cAMP (**Figure 2.3,2.4**). These permeability values were in line with those documented for other vascular microfluidic platforms [39, 112-114] and only slightly higher than those measured *in vivo* in the case of macromolecules [115]. Indeed, the current microfluidic device configuration includes only a layer of endothelial cells without perivascular supportive cells, such as pericytes, smooth muscle cells and fibroblasts that would reduce further the vascular permeability. [116, 117] Despite this, it should be highlighted that the treatment with db-cAMP did not affect the permeability for the 200 nm particles, suggesting that the proposed endothelial barrier could be accurately and efficiently employed to study the vascular transport of nanoparticles. The ability to modulate the vascular permeability was demonstrated further by infusing directly into the microfluidic devices Mannitol and Lexiscan. The exposure of the otherwise continuous endothelial layer to these permeabilizing agents resulted in an increase in permeability for both Dextran molecules and, at a lower extent, the 200 nm polystyrene beads (**Figure 2.5**).

After demonstrating the ability to precisely tune the vascular permeability from physiological to pathological values, the microfluidic device was used to study the dynamics of blood borne polymeric nanoconstructs. Specifically, in addition to the commercially available 200 nm polystyrene beads (PB), soft and rigid 1,000 × 400 nm discoidal polymeric particles (DPN) were considered. Here it is important to recall that while conventional nanoparticles, with a characteristic size of 100 – 200 nm, are expected to cross the hyperpermeable endothelial layer, DPN were designed to drift across the streamlines, in a process known as margination; firmly stick to the diseased vasculature; and release thereof their therapeutic cargo and imaging molecules.[99] In this context, the microfluidic device was used to evaluate the ability of soft and rigid DPN to marginate and adhere to the endothelial barrier under different flow and permeability conditions. In particular, the DPN behavior was tested at flow rates ranging from 0.1 µL/min (~100 µm/s), mimicking sub-physiological, quasi-tumoral flow conditions, to 0.5 µL/min (~ 1 mm/s), reproducing more physiologically relevant flow conditions.[101] As expected, neither the sDPN nor the rDPN were able to cross the micropillar membrane and diffuse deep into the extravascular compartment.

In the absence of endothelial cells, all the walls of the microfluidic device were solely coated by a layer of fibronectin and appeared as relatively flat interfaces. Differently, however, the micro-pillar membrane zone appeared as a wavy interface with repetitive valleys and crests, still coated by the fibronectin layer. In this configuration, both rDPN and sDPN were observed to preferentially accumulate at the micro-pillar membrane as opposed to the top, bottom, and lateral walls of the device (**Figure 2.9A-C**). The number of entrapped rDPN was almost constant over a wide range of flow rates. Although, at higher flow rates, rDPN were also observed to adhere at the bottom of the device. Interestingly, sDPN were entrapped in the micro-pillar membrane at a much

higher extent than rDPN, in a shear flow dependent manner (**Figure 2.9C**). Also, differently from rDPN, no significant accumulation of sDPN was observed on the bottom of the device, even at higher flow rates (**Figure 2.9B**). This preferential accumulation of DPN at the micro-pillar membrane, in the absence of endothelium, should be associated to the direct geometrical entrapment of those nanoconstructs moving in proximity of the irregular, wavy interface. Also, the deformable sDPN could be more easily entrapped, as opposed to their rigid counterpart, as the local shear rate increased. However, this could only partially explain the dramatic difference observed when comparing soft versus rigid DPN (**Figure 2.9C**). Possibly, an additional contribution to sDPN accumulation could be derived by a direct, hydrodynamic-based attraction of these nanoconstructs to the micro-pillar membrane. While it is well known that deformable particles moving in proximity of a flat wall would tend to be pushed towards the center of the channel by dominating lift forces [118], only recently computational analyses have demonstrated that deformable particles moving in proximity of a wavy interface could migrate away from the center toward the wall. [119] This hydrodynamic-based attraction would depend on the amplitude ε of the wall waviness, the ratio between the wavelength λ and the characteristic size R of the particle, and the local flow conditions. Importantly, this hydrodynamic-based attraction would only apply to deformable particles. Indeed, only an *ad hoc* computational analysis accounting for the specific micro-pillar membrane geometry, flow conditions and particle properties could help evaluate the relative importance of hydrodynamic-based attraction over geometrical entrapment.

For an endothelialized vascular compartment, the waviness of the micro-pillar membrane is massively reduced and DPN geometrical entrapment cannot occur anymore (**Figure 2.10A**). Notice, incidentally, that this was an additional demonstration of the proper endothelial coating of the micro-pillar membrane. Under this condition, the top, bottom, and lateral walls of the device

formed a continuous monolayer with a moderate waviness whose amplitude is now related to the cell nuclei. For the soft DPN, hydrodynamic-based attraction would be minimal and could outperform lift forces at the wall only at low flow velocities. This could explain the higher deposition observed for the sDPN at low flow rates (**Figure 2.10B**). For the rigid DPN, the margination velocity would tend to grow with the flow rates thus explaining the larger particle deposition at higher flow velocities.[120] Even in this case, only an *ad hoc* computational analysis could help to univocally identify the governing mechanisms regulating the behavior of different DPN. However, this is beyond the scope of the current work and certainly constitutes the starting point for future studies on vascular dynamics of soft versus rigid, non-spherical particles.

2.5 Conclusions

A double-channel microfluidic device was demonstrated to study the transport of macromolecules and nanoconstructs under different vascular conditions. A vascular compartment was covered by a continuous layer of endothelial cells, whereas an extravascular chamber was filled with a mixed collagen-Matrigel© matrix. After demonstrating the integrity of the endothelial barrier using different complementary techniques, the vascular permeability of macromolecules (250 kDa FITC-Dextran), nanoparticles (200 nm polystyrene beads), and polymeric nanoconstructs (1,000 × 400 nm discs) was characterized under physiological and pathological conditions. First, it was shown that the proposed microfluidic device could replicate physiologically relevant values of permeability down to the order of 0.1 μm/sec for the ~10 nm Dextran macromolecules. Then, it was documented that the vascular permeability could be modulated, and specifically increased, by

using two clinically relevant agents, Mannitol and Lexiscan. To the best of our knowledge, this is the first time that Lexiscan have been tested on a microfluidic platform. Finally, it was observed that soft discoidal polymeric nanoconstructs could more efficiently adhere to the vascular walls under pathological vascular conditions than their rigid counterparts. Collectively, these results demonstrated that the proposed double-channel microfluidic device could be efficiently and effectively used to test the vascular behavior of a variety of drug delivery systems under various conditions.

Chapter 3

Efficacy of molecular and nano-therapies on brain tumor models in compartmentalized microfluidic devices

3.1 Introduction

The preclinical screening of new therapies still relies on simplified, two dimensional (2D) *in vitro* models that cannot replicate the biochemical and biophysical complexity of the human diseases.[121, 122] Three-dimensional (3D) cell assembly, such as cancer spheroids and organoids, provide authentic representation of the *in vivo* tissue organization but cannot reproduce some dynamic mass transport processes. These processes are crucial for different therapies as they regulate the intra-tissue accumulation of systemically delivered therapeutic agents, the diffusion of nutrients, chemokines and cytokines, as well as the migration and spatial re-arrangement of malignant and healthy cells.[123-125] Microfluidic devices emerged as more accurate tool for screening novel therapies in cancer and other diseases because can replicate both the 3D tissue organization as well as mimic the delivery of therapeutic agents or cell migration, thus offering a more accurate tool for screening novel therapies in cancer and other diseases [126-131]. With this objective in mind, microfluidic devices have been designed to model a variety of disorders, including cancer, cardiovascular and chronic inflammatory diseases; as well as diverse biological

barriers, such as those arising at the interfaces between the blood vasculature and the brain tissue (blood brain barrier), the intestine (intestinal mucosal barrier) and the pulmonary alveoli (alveolar capillary barrier).

In general, microfluidic devices for disease modeling can be realized with one, two or multiple compartments to replicate the architectural complexity of the native tissue and include tissue/vascular and tissue/tissue biological barriers. The single compartment configuration, typically, comprises of one channel that is filled by a natural hydrogel carrying the cells of interest. The therapeutic agents are administered through one inlet port and slowly diffuse towards the opposite outlet. These microfluidic devices have been extensively used to test the vascular transport and adhesion of macrophages[132-134], cancer cells[135-137], and nanoparticles[98, 138-141] under diverse disease conditions. The two- and multi-compartment configurations comprise of multiple channels to separate out different tissue districts and more accurately replicate biological interfaces and barriers. In two-compartment configurations, one channel acts as the extravascular compartment (tissue), which is filled by a natural hydrogel carrying the cells of interest, while the second channel acts as the vascular compartment (blood vessel), which is continuously perfused by cell culture medium. The therapeutic agents are infused through the vascular compartment to simulate systemic administrations or through the extravascular compartment to model direct intra-tissue injections. Thus, the two-compartment configuration replicates a single biological interface, either a vascular/tissue or a tissue/tissue interface [142-146]. Multi-compartment based microfluidic devices comprise of more than two channels with different architectures to replicate a variety of biological interfaces.[130, 147-150] The two and more-compartment microfluidic devices have been efficiently used to model cancer tissues.

Selecting out a few notable examples from the literature, the group of Huh realized a two-compartment device comprising of an upper channel, reproducing the ductal lumen with pre-assembled breast carcinoma spheroids, and a lower channel, perfused by cell culture media to replicate the breast microvaculature.[143] A thin natural membrane with a layer of stromal cells was interposed between the two compartments. The system was validated by quantifying the anti-proliferative effect of paclitaxel on breast cancer cells. Compartmentalized microfluidic systems were also used by Kamm and collaborators [147, 151, 152], and other authors[95] [153] to study the vascular dynamics of circulating cancer cells and their extravasation/intravasation potential. Previous work from Decuzzi group used a two-compartment microfluidic device to quantify the metastatic potential of breast cancer cells under different environmental conditions, including the use of inflammatory factors as chemo-attractants.[95] Other authors used multi-compartment systems to model the complex biological features regulating the selective operation of the blood brain barrier or the alveolar capillary barrier.[128, 154, 155] Habibovic and Reis groups described a “tumor-on-a-chip" model for assessment of gemcitabine-loaded nanoparticle efficacy on colorectal cancer.[144] The viability studies together with live imaging demonstrated a dose dependent effect of gemcitabine loaded nanoparticles to colorectal cancer cells (HCT-116) embedded in Matrigel© inside the microfluidic chip.[144]

Herein, single- and double-channel microfluidic devices were employed for *in vitro* testing of model and innovative therapeutic compounds. In the single-channel device, a 3D tumor model simulated the direct injection/application of chemotherapy at the tumor site (i.e. *in situ*). In double-channel microfluidic chip, in which the two parallel channels are connected by micropillars, - a vascular and parenchymal-cancer compartment simulated the systemic administration of

chemotherapy. Glioblastoma multiforme (GBM) cancer was selected among numerous pathologies because it is referred as the most aggressive and lethal brain tumor in adults.[156] Previously, free docetaxel (DTXL) and spherical polymeric nanocontructs (SPN) loaded with DTXL (DTXL-SPN) were investigated for the treatment of cancer cells in conventional (2D) cultures and *in vivo*.[157-160] DTXL lacks specificity towards tumor cells and triggers huge side effects on patients.[161, 162] Its severe systemic toxicity together with its low solubility, leads to short blood circulation time in the body, erratic absorption patterns and thus, requires frequent administrations [163] ideally at the tumor site. Notwithstanding, a new promising selective chemotherapeutic, *N*-(fluorenylmethoxycarbonyl)-glucosamine-6-phosphate (Fmoc-Glc6P), has demonstrated a potent anti-cancer efficacy on osteosarcoma and breast cancer cells.[164-166] In this work, the efficacy of several therapeutic agents such as free DTXL, nanoparticles loaded with DTXL (DTXL-SPN), and Fmoc-Glc6P was tested for comparative purposes.[164-166]

3.2 Materials and Methods

3.2.1 Fabrication and Characterization of the Microfluidic Chips

Two different microfluidic chip designs were employed in this study: a single and double channel chip, described in detail by Manneschi *et al.* [145]. Briefly, a single channel silicon master template was obtained from a negative template of SU8-50 photoresist. The silicon template was replicated using a mixture of polydimethylsiloxane (PDMS) Sylgard 182 from Corning (Italy) by mixing base and curing agent in a ratio 1:10 (w/w). The PDMS solution was casted on the silicon template, degassed until all bubbles were removed and cured at 80°C overnight. The PDMS replicas were

cleaned with a scotch-tape and inlet and outlet ports were created with a biopsy punch. Oxygen (O_2) plasma treatment (pressure = 1.0 mbar, power = 20 W, time = 20 s) was performed and PDMS replicas were bonded to the glass coversheets. This chip had a length of 27 mm, a height of 42 µm and a width of 210 µm. For the fabrication of the double channel chips, an optical mask of glass was used together with a two lithographic steps to pattern first the micropillars and then the double channels into the silicon master chip. The obtained silicon master template was then replicated *via* soft lithography, as reported previously. The final PDMS template was composed by two microfluidic channels with a length of 27 mm, interconnected in the middle part by an array of micropillars with 500 µm in length with a gap size of 3 µm. The two channels had a height of 50 µm and a width of 200 µm. These chips had two parallel channels: the top channel corresponded to the vascular part where the treatment solutions (*e.g.* drugs, nanoparticles, and active compounds) were added; and the bottom channel corresponded to the extravascular part and contained a hydrogel with embedded cells to mimic the 3D structure of a tumor. Each channel had one inlet and one outlet and were connected by a permeable micropillar membrane.

3.2.2 Scanning Electron Microscopy (SEM)

SEM images of microfluidic chips were obtained using the equipment JSM-6490LV, JEOL and Helios Nanolab 650, FEI Company. These images were acquired after curing the PDMS on the silicon master template and peeling of the PDMS replicas. The microfluidic chips were sputter-coated with gold. Low-magnification and high-magnification SEM images were obtained with accelerating voltage of 15 and 5 kV, respectively.

3.2.3 Culture of Human Glioblastoma Multiforme (U87-MG) Cells and Primary Human Astrocytes

The cancer cells were previously transfected with GFP to easily visualize them *in situ* longitudinally with time. U87-MG GFP+ cells were cultured in Minimum Essential Medium Eagle (EMEM, Gibco, ThermoFisher Scientific) supplemented with 10% heat-inactivated fetal bovine serum (FBS) and 1% penicillin/streptomyocin (P/S). Human cortical astrocytes (#1800, ScienCell Research Laboratories, US) were cultured with astrocytes medium with 1% P/S. U87-MG GFP+ and human astrocytes were cultured in T150 flasks until confluence. After the trypsinization, human astrocytes were stained with Vybrant™ DiI Cell-Labeling Solution (#V22885, ThermoFisher Scientific), according to the manufacture's protocol. Then, the cells were washed 3 times with PBS (1X) to remove the excess dye. After proper optimization of matrix's concentration and cell density, a concentration of 50:50 Matrigel©/cells in EMEM medium were prepared to a final number of 100,000 cells embedded in Matrigel© per chip (Corning). Single- or double channel chips were used to culture U87-MG GFP+ cells or astrocytes with Matrigel© for 24 hours to form a confluent 3D cell network and after that different treatment solutions were added for 24, 48 and 72 hours. After each time point, the cell viability was analyzed by confocal microscopy.

3.2.4 Human Glioblastoma Multiforme (U87-MG) Cells in static culture conditions

Static cultures on 96-well plates (10,000 cells/ well) were performed with U87-MG cells for 24 hours. After that, different treatment solutions (0.001, 0.01, 0.5, 0.1, 1 and 10 µM free DXTL and 0.5 mM free Fmoc-Glc6P were added and metabolic activity, DNA and ALP measurements were

conducted after 24, 48 and 72 hours. Cellular metabolism in 2D monolayers was evaluated using MTT assay and following supplier's instructions. U87 MG cells were seeded into a 96-well plate and after 24 hours, the cells were treated with different DTXL concentrations (0.001, 0.01, 0.5, 0.1, 1 and 10 µM) and for upto 72 hours. These studies were performed by changing or without changing the DXTL solutions every day. The optical density (O.D.) was read at 490 nm on a multiwell microplate reader. Cell viability was calculated as the difference of optical density (O.D) values obtained for the controls (cell-seeded conditions without treatment) and the O.D. measured values of the cell-seeded conditions treated with different DTXL concentrations assessed after 24, 48 and 72 hours. These values were then converted in % of viable cells. The half-maximal (50%) inhibitory concentration (IC_{50}) was estimated as the 50% of cell viability relative to the negative control of cell death (cells grown in TCPS – without treatment, only EMEM medium).

The DNA concentration of the cell lysates was quantified by using the Quan-iT™ PicoGreen® dsDNA assay kit (Molecular Probes/Invitrogen) following the manufacturer's instructions.

3.2.5 Treatment Conditions using Single and Double Channel Microfluidic Chips

Microfluidic chips were sterilized in an autoclave at 120°C. Then, the channels were aspirated within the biohood and the chips were left inside the incubator overnight to remove the water from the channels. U87-MG GFP+ cells or human astrocytes embedded in Matrigel were injected into microfluidic chips and were cultured for 24 hours to form a 3D brain tumor-like tissue.

Single channel microfluidics chips were used to screen several concentrations of DTXL.A stock solution of DTXL (42 mM) was prepared in dimethyl sulfoxide (DMSO). This solution was diluted

with EMEM to 0, 0.01, 0.5, 0.1, 1 and 10 µM solutions. To assess the cytotoxicity of the anti-cancer drug DTXL, EMEM with different drug concentrations (0.01, 0.5, 0.1, 1 and 10 µM) was added to the channel inlet and left to diffuse across the 3D brain tumor-like tissue. The therapeutic solution was added every single day to the chip, for upto 72 hours. EMEM was used as a control in this set of experiments.

In the double-channel microfluidic device, three different treatments were investigated: (1) free DTXL (0.01, 0.1, and 10 µM); (2) spherical nanoconstructs (SPNs) loaded with DTXL (10 µM) (DTXL-SPN); and (3) 500 µM free *N*-(fluorenylmethoxycarbonyl)-glucosamine-6-phosphate (Fmoc-Glc6P). All solutions were prepared in EMEM. The DTXL-SPN were fabricated as previously described by us.[160] Fmoc-Glc6P compound was synthesized following the procedure described by Pires *et al*.[164] The different therapeutics or just EMEM medium (control) were injected into the vascular (top) channel every day. After 24, 48 and 72 hours, each (bottom) channel with U87-MG GFP + cells embedded in Matrigel was observed using the confocal microscope.

3.2.6 Confocal Microscopy Analysis

Confocal fluorescent microscopy (Nikon A1R+/A1+; objectives Nikon, 10X or 20X) has been extensively used to document the 3D organization of U87-MG GFP+ cells or human astrocytes embedded in Matrigel throughout the microfluidic chips as well as its viability over time. After each time period, single and double channel microfluidic chips cultured with U87-MG GFP + cells and human astrocytes stained with Dil and embedded in Matrigel were observed and analyzed using a confocal laser microscope where a z-stack throughout the height of the channels was performed. Images were recorded using automated acquisition for Z-stack and multicolor channel.

Each experiment involved at least five chips per condition and was repeated three times. The same region of interest (ROI) was analyzed after each time point. High-resolution Z-stack images were processed for 3D reconstruction and measurement of fluorescence intensity were performed using NIS-Elements AR (Nikon) software. Cell viability, with EMEM only (control) and after different treatments, was determined measuring the mean fluorescence intensity exhibited by green fluorescent protein (GFP+) cells. Cell viability was presented as percentage, calculated from the fluorescence intensity after 24, 48 and 72 hours. The half-maximal (50%) inhibitory concentration (IC_{50}) was estimated as the 50% of cell viability relative to the negative control of cell death (cells grown in 2D monolayers in TCPS). Also, for the estimation of IC_{50} of increasing concentrations of DTXL on cells cultured in 2D and in single channel microfluidic chips at 24, 48 and 72 hours, a study for the best regression models that would fit the curvature of the data obtained was performed. A logarithmic curve was considered as the best fitting (nonlinear regression) and the IC_{50} for each time point of both experiments was estimated.

3.2.7 Statistical Analysis

Data are expressed as mean ± standard deviation. Single factor analysis of variance (ANOVA) was used to determine statistical significance within a data set. If ANOVA detected a significant difference within the data set, Tukey's honestly significantly different (HSD) multiple comparison test was used to determine significant differences between groups and conditions.

3.3 Results

Two different microfluidic device configurations were used to reproduce *in vitro* the complex 3D organization of cancer cells: a single-channel **(Figure 3.1A)** and a double-channel **(Figure 3.1B**) configurations. The first device comprised of a channel with a total length of 27 mm and a rectangular cross section of 210 μm (width) by 42 μm (height). The second device comprised of two parallel channels with a total length of 27 mm and a rectangular cross section of 200 μm (width) by 50 μm (height). In the center of the double-channel device, the two channels were connected through a series of micropillars over a length of 500 μm (**Figure 3.1B, bottom-right inset**). The micropillars realized a membrane with openings of about 3 μm in size.

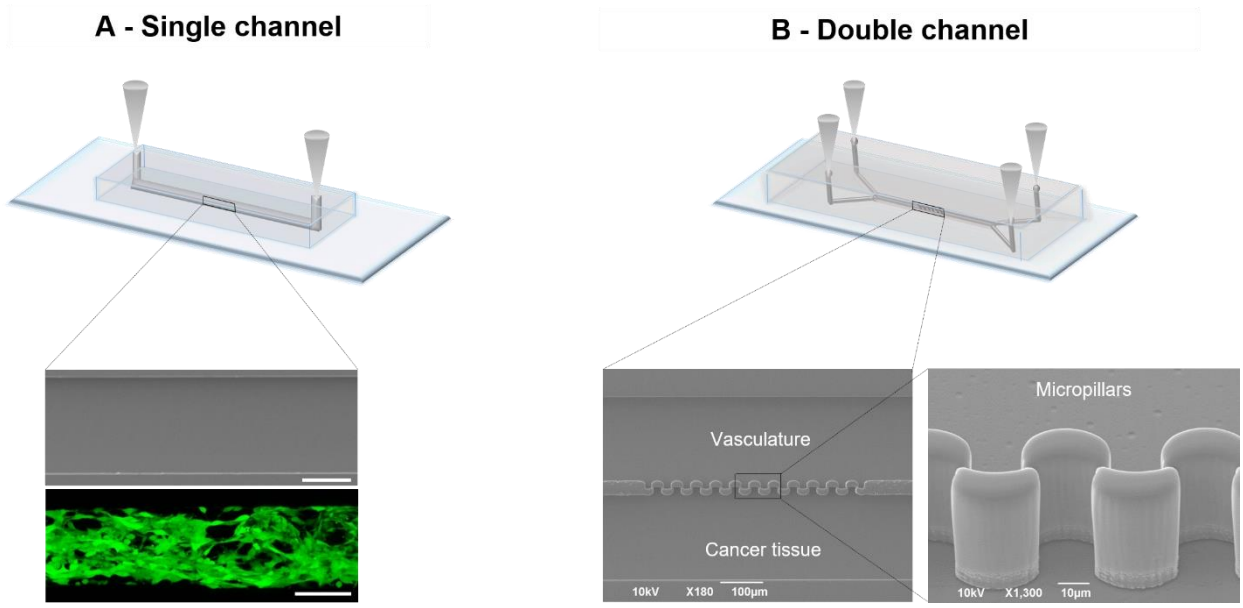

Figure 3.1. Microfluidic devices. A) Schematic representation of the single-channel device, including a scanning electron microscopy (SEM) micrograph of the channel and a confocal image of U87-MG GFP+ cells cultured in Matrigel matrix. B) Schematic representation of a double-channel device, including a SEM micrograph of the two-channels (extravascular and vascular compartments). The bottom-right inset gives a SEM image of the micropillars realizing the permeable membrane between the two-compartments. (Scale bar: 100 μm, except for the micropillar image - bottom right - 10 μm).

Within these devices, 3D-like tumor tissues were realized using green-fluorescent protein transfected (GFP+) human glioblastoma multiforme cancer cells (U87-MG) embedded in a Matrigel matrix. In the single-channel configuration (**Figure 3.1A**), the U87-MG embedded in Matrigel was deposited along the channel length. This configuration mimiced an *in situ* administration of chemotherapeutic agents at the tumor site, similar to a conventional organoid or tumor spheroid, where nutrients, chemokines and therapeutic agents diffuse across the malignant mass following concentration gradients. In the double-channel configuration, simulating the systemic administration treatment (**Figure 3.1B**), the matrix with the cancer cells was deposited in the extravascular channel – cancer tissue – whereas the second channel was traversed by medium – emulating blood flow. The series of micropillars served to realize the blood/tissue interface that confines the Matrigel matrix on the extravascular compartment while supporting the extravasation of nutrients, molecules and nanoparticles. Here it is important to note that, typically, the biological barriers in the largest majority of microfluidic devices are realized by placing in between two adjacent channels or compartments pre-fabricated porous membranes to locally reproduce a Boyden chamber. Consequently, the two compartments lay on different focal planes and cannot be imaged simultaneously under a microscope. Differently, the compartments in the present microfluidic device lay horizontally on the same focal plane.[95, 145]

Different therapeutic agents (**Figure 3.2**), including free docetaxel (DTXL), DTXL-SPN, and the free aromatic N-glucoside Fmoc-Glc6P, were infused in the microfluidic device to assess their cytotoxic potential on cancer cells under different conditions. The very potent anti-cancer drug DTXL was considered as a model drug. The DTXL-SPN were fabricated following protocols

already published by the authors.[160] Similarly, the Fmoc-Glc6P compound was synthesized based on the work of Pires *et al*. [164].

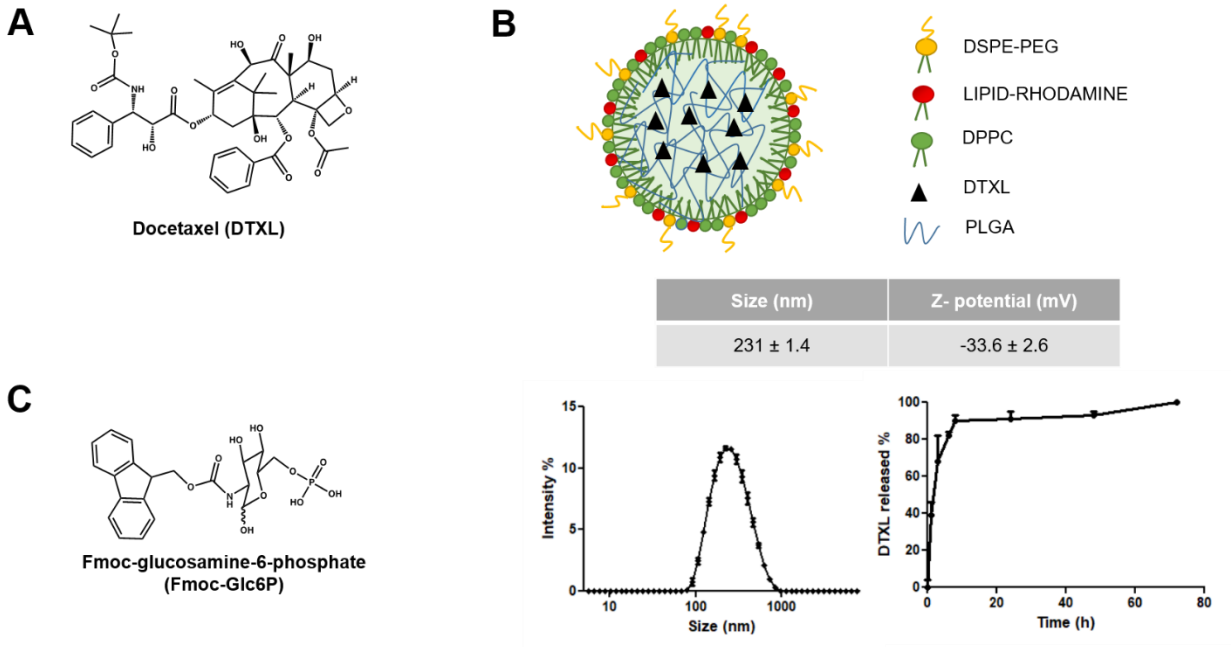

Figure 3.2. Therapeutic agents. A) Chemical structure of docetaxel (DTXL). B) Schematic representation of the spherical polymeric nanoparticles (SPN) composed by 1,2-Distearoyl-sn-glycero-3-phosphoethanolamine-Poly(ethylene glycol) (DSPE- PEG), Lipid-Rhodamine as a fluorofore, dipalmitoylphosphatidylcholine (DPPC), poly(lactic-co-glycolic acid) (PLGA), and loaded with docetaxel (DTXL-SPN); diameter and Z-Potential, size distribution measured by Dynamic Light scattering (DLS), the release profile at 37 °C in physiological solution (PBS, pH 7.4); and (C) 500 µM Fmoc-Glc6P for 24, 48 and 72 hours. C) Chemical structure of the aromatic N-glucoside N-(fluorenylmethoxycarbonyl)-glucosamine-6-phosphate (Fmoc-Glc6P).

In the single-channel configuration, the therapeutic agents were slowly infused through an inlet port and allowed to diffuse across the whole tumor matrix to reach the outlet port. In the double-channel configuration, the therapeutic agents are slowly infused in the blood channel and perfuse into the extravascular compartments by crossing the micropillar membrane.

3.3.1 Assessing the cytotoxic potential of therapeutic agents in the single-channel microfluidic device

In the single-channel configuration (**Figure 3.1A**), 3D tumor-like tissues were obtained using U87-MG GFP+ embedded in a Matrigel matrix and then the different therapeutics were injected directly throughout the 3D structure. The cancer cells were transfected with GFP to easily visualize them *in situ* longitudinally with time. A sufficiently large number of cells (100,000) were mixed with Matrigel to realize a confluent tridimensional cell network (**Figure 3.1A** and 3.**3A-E**, time 0 hours – without DTXL). To assess the cytotoxic potential of the anti-cancer drug docetaxel (DTXL), medium with different drug concentrations (0.01, 0.5, 0.1, 1 and 10 µM) was added to the channel inlet and left to diffuse across the 3D tumor-like tissue. The therapeutic solution was added every single day into the chip, for upto 72 hours. The viability of the tumor cells was estimated by analyzing the variation of the green fluorescent intensity over time: an increase in fluorescence intensity was associated with a higher cell density, thus indicating cell viability; whereas a decrease in fluorescence intensity was associated with a lower cell density, thus indicating cell death.

The fluorescent images of **Figure 3.3A-E** report the variation in cancer cell density within a representative section of the channel (~ 2.9 mm) over time (from 0 to 72 hours) and for different DTXL concentrations. As expected, the cell viability reduced upon DTXL administration in a time- and concentration-dependent fashion. At the lowest concentration of DTXL (0.01 µM), the cell density started to decrease significantly only after 72 hours **(Figure 3.3A)**. On the other hand, the cell density was already dramatically reduced after the first 24 hours at the highest tested concentrations of 1 and 10 µM **(Figure 3.3D, E)**. The cell viability percentage for all the different treatment conditions and time points presented in **Figure 3.3F** and quantitatively documented the progressive increase in cell death with time and drug concentration. IC_{50} values were also

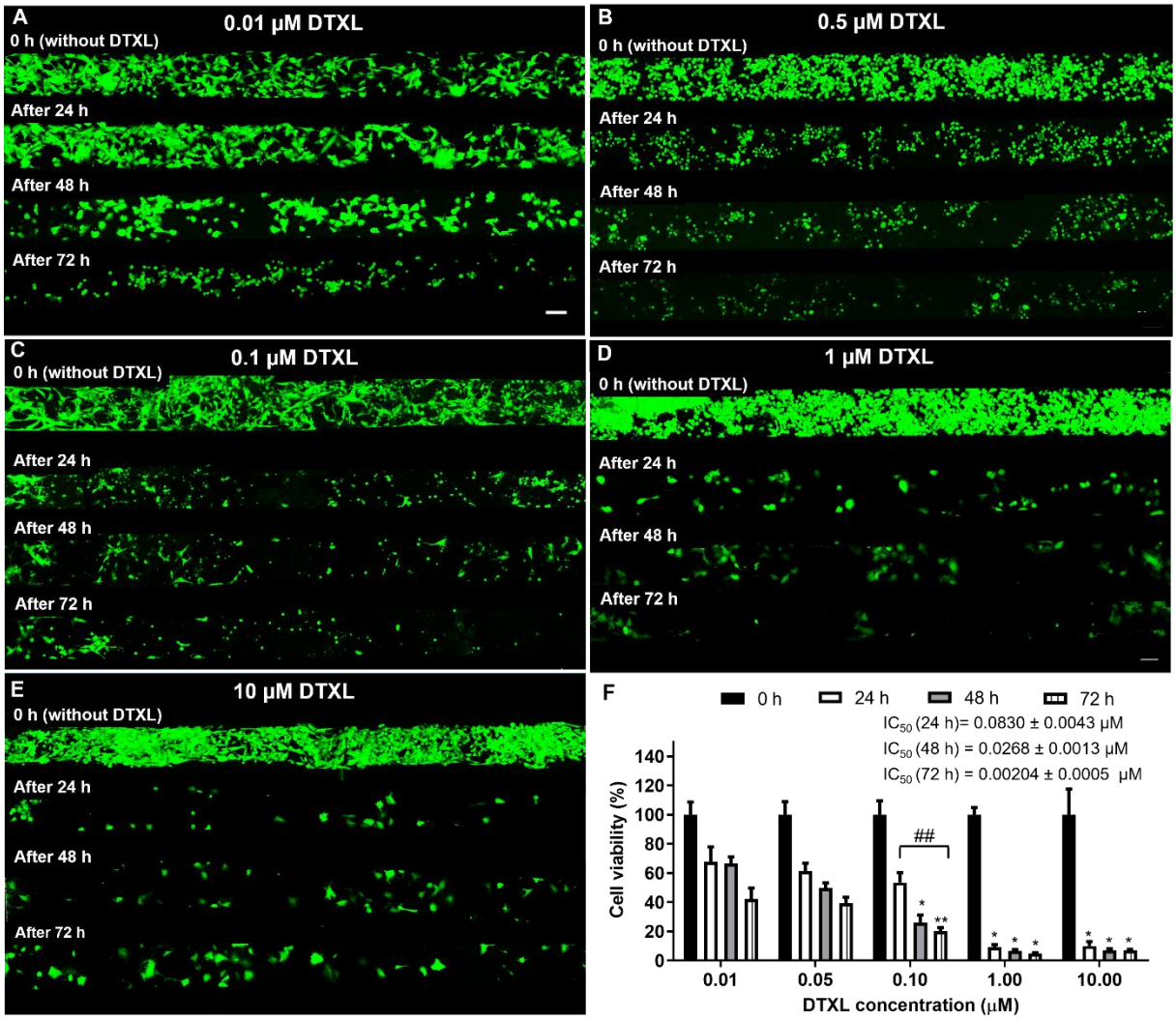

Figure 3.3. Human brain tumor cell viability analysis in single-channel microfluidic device– free DTXL. A-E) Representative confocal fluorescent microscopy images of U87-MG GFP+ cells cultured in Matrigel and exposed to different doses of free DTXL (0.01, 0.05, 0.1, 1 and 10 µM) at different time points (24, 48 and 72 hours). The scale bar is 50 µm and applies to all images. F) Cell viability analyses and IC_{50} values determined for the different time points. Results are expressed as mean ± SD (n = 5 per time point). All concentrations presented a significant difference over time compared to control (no treatment) except at 0.01 µM after 24 and 48h hours. *: $p < 0.01$ and ** $p < 0.05$ between different concentrations in the same time point; ##: $p < 0.05$ for the same concentration of DTXL at different time points).

estimated for each different time point returning the values 0.0830 ± 0.0043, 0.0267 ± 0.0013 and 0.0020 ± 0.0005 µM µM at 24, 28, and 72 hours, respectively.

The cytotoxic effect of free DTXL was also tested on U87-MG GFP+ cell monolayers cultured in a conventional 96 well-plate system. In this case, the cell viability was assessed via a standard MTT assay (**Figure 3.4**) with and without changing the DTXL solution every day. In the first case, when the drug solution was changed daily, the measured IC_{50} values were 1.1822 at ± 0.0025 at 48 hours and 0.1083 ± 0.0008 µM at 72 hours. At the 24 hours time point, cell viability was well above 50% even at the highest tested concentration of 10 µM. A similar trend was observed at all time points when the DTXL solution was not changed for the full duration of the experiment. This observation would imply that DTXL had a higher cytotoxic potential on 3D cells as compared to 2D cell monolayers.

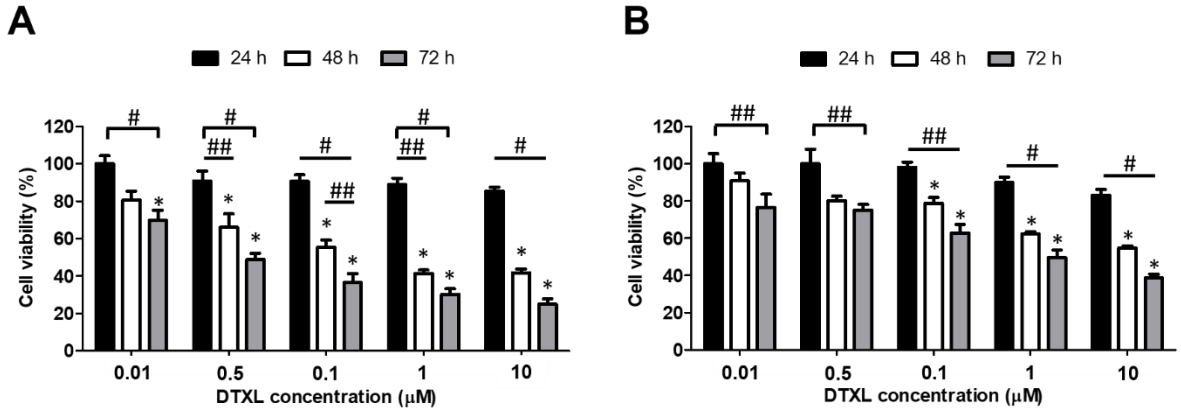

Figure 3.4. Metabolic activity of U87-MG. Cells cultured in 96-weell plates treated with increasing concentrations of free DTXL (0.01, 0.5, 0.1, 1 and 10 µM) changing (B) and without changing (A) DTXL solutions every day. Data are shown for culture of 10,000 cells per well as optical density (O.D.) values from MTT assay at 24, 48 and 72 h time points. Results are expressed as mean ± SD (n = 5 per time point). These values were then converted in % of viable cells. (*) Indicates a significant difference ($p < 0.01$) compared with the control (cells cultured without treatment); (#) a significant difference ($p < 0.01$) or (##) ($p < 0.05$) of the same condition (treatment) as a function of time.

3.3.2 Assessing the cytotoxic potential of therapeutic agents in a double-channel microfluidic device

Based on the data obtained for single-channel device, the cytotoxic potential of DTXL was examined only for the highest concentrations of 0.01, 0.1 and 10 µM. The therapeutic agents were slowly infused into the vascular compartment (upper channel) **(Figure 3.1B)** and transported partially to the extravascular compartment (bottom channel – cancer tissue compartment), filled with the Matrigel matrix and U87-MG GFP+ cells, leading directly to the chip outlet. In other words, as per the systemic administration of any compound, part of the injected dose does reach the diseased tissue (in this case the extravascular compartment) whereas the remaining portion is distributed throughout the body (here the outlet port in the chip).

In this double-channel configuration, three therapeutic agents were tested, namely free DTXL (0.01, 0.1 and 10 µM); DXTL-SPN (10 µM of DTXL); and the free compound Fmoc-Glc6P (500 µM). The viability of the U87-MG GFP+ cells were assessed at 24, 48 and 72 hours, following the variation in green fluorescence intensity as described above.

For free DTXL, no cytotoxic effect was observed at 0.01 µM DXTL for all tested time points **(Figure 3.5A)**. At 0.1 µM DXTL, a significant cell death was detected only at 72 hours **(Figure 3.5B)**. At the highest tested concentration of 10 µM, free DXTL induced cell death in a time dependent fashion **(Figures 3.5C)**. Quantitative data for the cell viability are presented in **Figure 3.5D**. Notably, in the double-channel microfluidic device, the cell viability was generally higher than 50% for the tested drug concentrations except in the case of 10 µM DTXL at 72 hours. As such, IC_{50} values could not be estimated within the considered range studied. Reconstructed 3D images of the U87-MG GFP+ cells within the microfluidic device presented in **Figure 3.5E** for

the 10 µM free DXTL treatment. These documented the progressive reduction in fluorescence intensity (cell death) moving from time 0 hours, when the extravascular compartment appears all green against a black vascular compartment, to 72 hours, when only a few sparse cell assemblies are still visible **(Figure 3.5E)**. It was noticed that at the given drug concentrations, the cytotoxic activity of DTXL on the U87-MG cells was significantly reduced in the double-channel microfluidic device as compared to the single-channel configuration. Indeed, this should be ascribed to the diminished concentration of DTXL reaching the tumor compartment as part of the infused drug was washed away via the blood compartment.

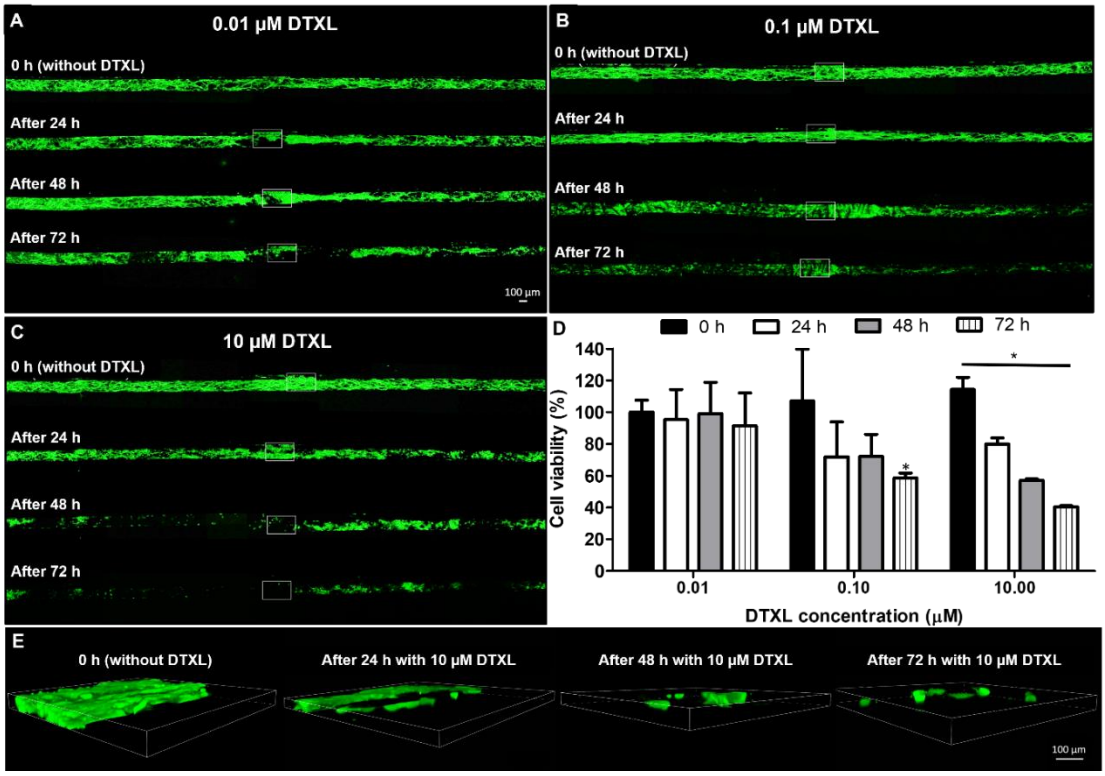

Figure 3.5. **Human brain tumor cell viability analysis in double-channel microfluidic device – free DTXL.** A-C) Representative confocal fluorescent microscopy images of GFP+ U87-MG cells cultured in Matrigel and exposed to different doses of free DTXL (0.1, 1 and 10 µM) at different time points (24, 48 and 72 hours). D) Cell viability analyses determined for the different culturing conditions. E) 3D-Reconstruction of confocal fluorescent images showing the GFP+ U87-MG cell density at different time points post exposure to 10 µM DTXL. (Scale bar: 100 µm. *: $p < 0.01$).

Differently, in the single-channel configuration, all the infused DTXL was distributed within the tumor tissue and affected the viability of the cancer cells. Also this is a fundamental difference between the double-channel microfluidic device and the cancer spheroids and organoids.

For assessing the cytotoxic potential of DTXL-SPN, only the highest DTXL dose was considered (10 μM). The confocal microscopy images of **Figure 3.6A** show a progressive reduction in green fluorescence intensity over time that was associated with cell death.

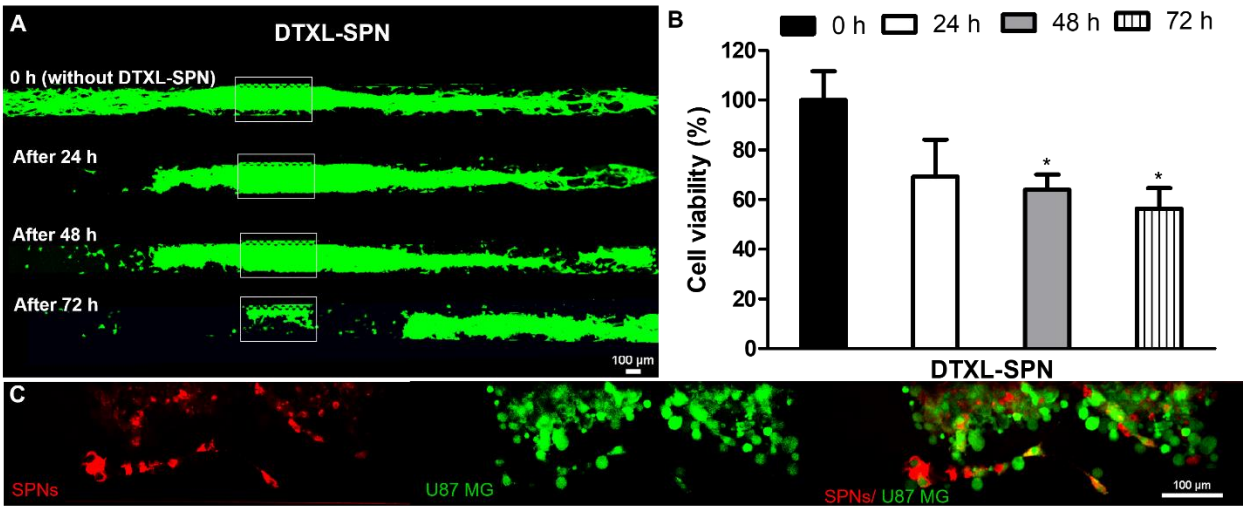

Figure 3.6. Human brain tumor cell viability analysis in double-channel microfluidic device – DTXL-SPN. A) Representative confocal fluorescent microscopy images of U87-MG GFP+ cells cultured in Matrigel and exposed to SPN loaded with 10 μM DTXL (DTXL-SPN), at different time points (24, 48 and 72 hours). B) Cell viability analyses determined for the different culturing conditions. Results are expressed as mean ± SD (n = 4 per time point). *: $p < 0.01$ compared with the control (no treatment). C) Representative confocal fluorescent microscopy images at 72 hours showing U87-MG GFP+ (green dots) and RhB-SPN (red dots) next to the micropillars. (Scale bar: 100 μm).

At all considered time points, the cell viability for the DTXL-SPN (**Figure 3.6B**) was comparable to that quantified with free DTXL (**Figure 3.5D**).

Specifically, at 24 hours, the cell viability was 69 ± 30% for DTXL-SPN vs 80 ± 6% for free DTXL. This reduced to 64 ± 12% vs 57 ± 2% at 48 hours and to 56 ± 17% vs 40 ± 1% at 72 hours for DTXL-SPN and free DTXL, respectively.

By using spherical polymeric nanoparticles SPN labeled with the red fluorescent dye Rhodamine-B (RhB-SPN), it was demonstrated that the infused nanoparticles were able to permeate across the micropillar membrane and diffuse throughout the tumor-like tissue (**Figure 3.6**). The red dots (**Figure 3.6C – left**) was associated with the RhB-SPN only and the tumor cells appeared green (**Figure 3.6C – center**). The right insets of **Figure 3.6C** shows the overlap between the red and green channels demonstrating the co-localization of the nanoparticles with the cancer cells. As expected, the nanoparticle density was particularly high in the vicinity of the permeable micropillar barrier and reduced upon moving deeper into the extravascular compartment. It should be noticed that even in the case of the DTXL-SPN, a significant dose of nanoparticles and DTXL was expected to be washed away and lost without ever reaching the malignant tissue similar to the situation *in vivo*.

Interestingly, in the case of DTXL-SPN treatment, a significant asymmetric distribution for dead versus live cancer cells were observed. **Figure 3.6A** shows that live U87-MG cells (green fluorescent) were more abundant on the right-hand side of the channel, with respect to the micropillar permeable barrier. Also, the flow in the blood compartment was directed from right to left. This would indicate that the DTXL-SPN permeation and distribution within the extracellular matrix was governed by advection in addition to diffusion. This also appeared in **Figure 3.6C** where the RhB-SPN accumulation was higher on the left-hand side of the channel with respect to the micropillar membrane. Indeed, this asymmetry is less evident in the case of the molecular

compounds for which advection is in general negligible. Importantly, this process can only be observed is the actual vascular transport of therapeutic agents towards the diseased tissue is modeled.

Finally, the double-channel microfluidic device was also used to assess the therapeutic efficacy of a novel compound – Fmoc-Glc6P for this type of cancer cells. The efficacy of this compound was originally demonstrated on osteosarcoma (SaOs-2) and breast cancer (MDA-MB-468) cell lines.[165] It acts as an efficient cancer antimetabolite by concomitantly blocking the glucose transporter 1 (GLUT1) *via* specific interactions and formation of a nanonet serving as a physical barrier between the cancer cells and their environment.[165, 166] The treatment was more efficient in spheroids compared to 2D culture due to the higher GLUT1 expression in 3D cultures.[164-166] Notably, GLUT1 was significantly upregulated both *in vitro* and *in vivo* GBM and thus, we hypothesized that this therapeutic molecule could also be efficient in GBM.[167, 168] Indeed, Fmoc-Glc6P demonstrated a strong anti-proliferative and cytotoxic effect on U87-MG cells cultured in 2D as well as in the double-channel microfluidic chips. We selected a concentration of 500 μM for our experiments based on the previous studies with Fmoc-Glc6P.[164].

Similar to the other therapeutic agents, Fmoc-Glc6P was infused directly into the vascular compartment. A significant drop in cell survival was observed over time (**Figure 3.7A**). At 72 hours only a few sparsely viable U87-MG cells were visible in the channel. This was precisely quantified in **Figure 3.7B** with a U87-MG cells showed viability equal to 46.54 ± 28.61%, 35.62 ± 9.56%, and 19.31 ± 13.82% at 24, 48 and 72 hours, respectively. This behavior

was also documented by measuring the cell proliferation rates using the Quan-iT^{TM} PicoGreen® dsDNA assay kit **(Figure 3.8)**.

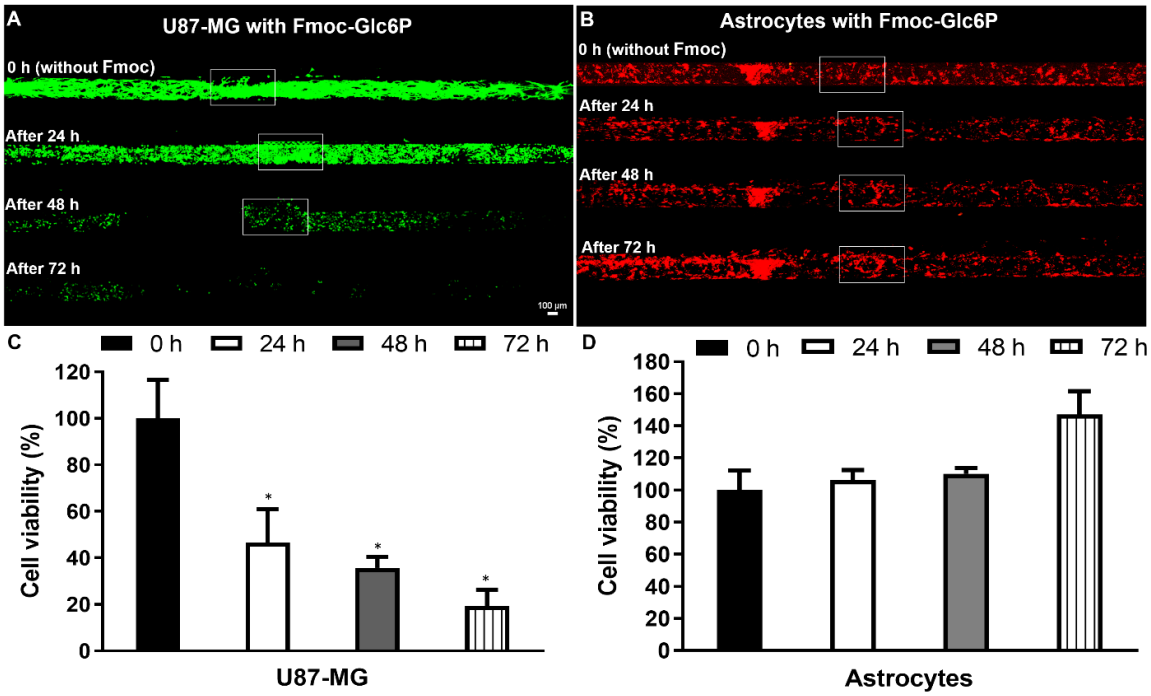

Figure 3.7. Human brain tumor cell and astrocytes viability analysis in double-channel microfluidic device – Fmoc-Glc6P. A) Representative confocal fluorescent microscopy images of U87-MG GFP+ cells cultured in Matrigel and exposed to 500 µM of Fmoc-Glc6P, at different time points (24, 48 and 72 hours). B) Representative confocal fluorescent microscopy images of astrocytes stained with Dil, cultured in Matrigel and exposed to 500 µM of Fmoc-Glc6P, at different time points (24, 48 and 72 hours). C,D) Cell viability analyses determined for the different culturing conditions of the U87-MG cells GFP+ and human astrocytes stained with Dil. Results are expressed as mean ± SD (n = 4 per time point). *: $p < 0.01$ compared with the control (only EMEM medium). (Scale bar: 100 µM).

The DNA assay showed a significant decrease ($p < 0.01$) in cell proliferation over time in the presence of 500 µM Fmoc-Glc6P. As expected, this was more effective than a 10 µM free DTXL in controlling the proliferation rates. Furthermore, the possible cytotoxic effects of Fmoc-Glc6P

compound on healthy brain cells – human astrocytes – was assessed within the same microfluidic device (**Figures 3.7C**). The astrocytes were stained with the red fluorescein molecule Dil and their viability was assessed.. Fmoc-Glc6P clearly show no toxic effect on human astrocytes (**Figures 3.7C and Figure 3.7D**) with no decrease in cell viability over time. This result would indicate the high selectivity of Fmoc-Glc6P in solely targeting and eliminating the cancer cells.

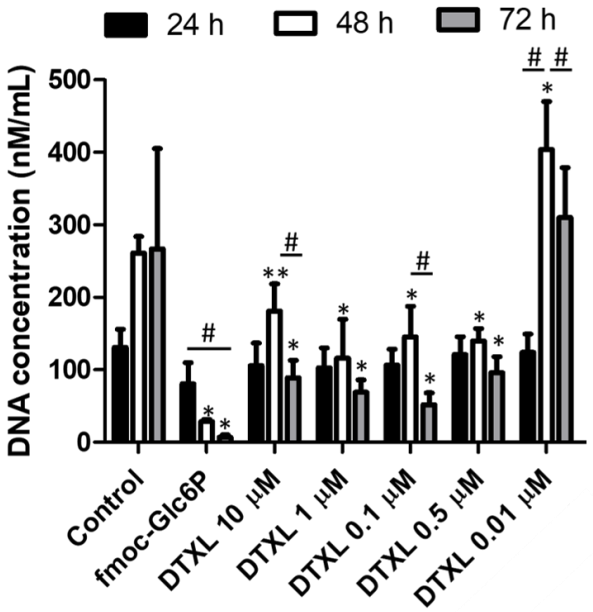

Figure 3.8. DNA concentration of U87 MG cells cultured in 96-well plates using different treatments. The therapeutic solutions consisted in: 0.5 mM Fmoc-Glc6P compound and different concentrations of free DTXL (0.001, 0.01, 0.5, 0.1, 1 and 10 µM) for 24, 48 and 72 hours. (*) Indicates a significant difference ($p < 0.01$) or (**) ($p < 0.05$) compared with the control (cells cultured without treatment); (#) a significant differe
nce ($p < 0.01$) or (##) ($p < 0.05$) of the same condition (treatment) as a function of time.

3.4 Discussion and Conclusions

Conventional cell culture monolayers poorly recapitulate the native physiology of the diseased tissue since they do not support complex 3Dcell organization and the dynamic arrangement under multiple, different physiological clues. On the other hand, microfluidic chips allow to simulate complex cell-culture microenvironments, including the realization of vascular-tissue and tissue-tissue interfaces, with spatiotemporal chemical gradients and mechanical clues of living tissues. This enables the development of new *in vitro* disease models and potentially the replacement of animal experiments [131, 169]. Indeed, microfluidic devices tend to overcome several limitations of the current animal models, including cost, labor time, reproducibility, insufficient similarity with the human physiology and undesired immune responses and indeed ethical issues. Studies have also suggested that the use of microfluidic devices might accelerate the design of drug-administration regimens for phase I clinical trials [129].

In this work, microfluidic devices with a single-channel and double-channel configurations were considered to emulate the administration of chemotherapy for brain tumor treatment *in situ* and systemically, respectively. Human U87-MG cells were dispersed into a Matrigel matrix, deposited within the channel of the microfluidic device and exposed to a therapeutic solution containing free docetaxel (DTXL), docetaxel loaded nanoparticles (DTXL-SPN) or the molecular compound Fmoc-Glc6P. In the double-channel microfluidic device, the solution with the therapeutic agent was infused in the so-called blood compartment while the tri-dimensional tumor-like tissue was deposited in the other channel (extravascular compartment). In both devices, the cancer cell viability was assessed by quantifying the intensity of the green fluorescence associated with the U87-MG GFP+ cells.

By comparing the brain cancer cell viability in the tumor chip (single-channel microfluidic device) with a conventional cell monolayer, it resulted that U87-MG cells were more susceptible to DTXL chemotherapy when they were arranged in a 3D matrix as documented by a 50 times decrease in the characteristic IC_{50} values. Free DTXL showed greater toxicity for U87-MG cells cultured into single-channel microfluidic devices compared to those cultured in conventional 2D monolayers. This confirmed the potential of free DTXL to be injected *in situ* at the tumor site. This trend of high chemosensitivity exhibited in 3D models was previously described in a study using bevacizumab. It was showen that when it was added to standard chemoradiation in phase III clinical trials it exhibited marked radiosensitizing activity in the developed 3D model of GBM but had no effect on 2D cells[170]. Moreover, a study investigating different cell lines from patients with head and neck squamous cell carcinoma revealed that LK0902 cells were more sensitive to cetuximab treatment in 3D conditions than cells grown in 2D[171]. Finally, this finding was also corroborated by Brito *et al*.[166] where they observed that the efficiency of the treatment with Fmoc-Glc6P was higher in spheroids as compared to the conventional 2D cultures due to higher expression of glucose transporter 1 (GLUT1) by the cancer cells.[166]

Blood-tumor models (double-channel microfluidic device) could also replicate flow dynamics and the actual vascular transport of systemically administered therapeutic agents. By comparing the brain cancer cell viability for the single versus the double-channel configuration, it was concluded that significant amounts of therapeutic agents were lost in the circulation and distributed to other tissue districts without ever reaching the malignant cells. This resulted in a dramatic drop in cell viability for the same given administered dose in the double- vs the single-channel configuration. Also, moving from small molecules, such as docetaxel, to larger therapeutic agents, such as docetaxel-loaded nanoparticles, advection in addition to diffusion was shown to contribute to drug

distribution and, therefore increased efficacy. This was documented by the asymmetric distribution of live vs dead tumor cells which was positively correlated with the vascular flow direction. It was also shown that DTXL-loaded nanoparticles were more efficient than the free DTXL molecules in inducing cell death. Additionally, free DXTL and DTXL-SPNs were less efficient than Fmoc-Glc6P to induce U87-MG cell death when cultured into double-channel microfluidic device. Moreover, Fmoc-Glc6P targeted specifically U87-MG cells without any deleterious effect in human astrocytes. These findings demonstrated that the double-channel can better replicate the vascular transport of systemically administered therapeutic agents and recreates closely the *in vivo*-like environment than 2D or the single-channel configuration. Also, Fmoc-Glc6P demonstrated high potential to be applied systemically because it acted specifically against cancer cells without causing adverse effects on healthy cells, combining a greater therapeutic efficacy with minor side effects.

Several chemotherapeutics, namely free DTXL, DTXL-SPN and Fmoc-Glc6P, were investigated using microfluidic chips. To elucidate the behavior and assess their anti-cancer therapeutic efficacy in a more realistic scenario, we used single- and double-channel microfluidic devices simulating *in situ* and systemic administration, respectively. Importantly, the U87-MG cells cultured in 2D conditions were clearly more resistant to DTXL treatment, presenting IC_{50} 50-fold greater, as compared to those cultured in single-channel microfluidic chips. This study also clearly demonstrated the outstanding behavior of Fmoc-Glc6P, showing a selective effect on cells inducing the death of GBM cancer cells, without eliciting deleterious effect on healthy/normal cells. Also, the effect of Fmoc-Glc6P, specifically on cancer cells cultured into double-channel microfluidic chips, showed the potential of this model to anticipate more closely the *in vivo* outcomes.

Overall, this study demonstrated the importance of microfluidic devices as excellent predictive tool for modeling the *in situ* and systemic administration conditions of chemotherapeutics, to simulate the *in vivo* microenvironment of a tumor, reproducing complex spatial cell organization and mass transport processes and to assess the efficacy of new effective molecular- and nano-therapeutic anti-cancer compounds.

Chapter 4

Three-dimensional extracellular layer mediated neural stem cell differentiation in a microfluidic device

The Central Nervous System (CNS) is comprised of neurons, the primary functional units and glial cells, the supporting cells. These cells originate from a unique class of progenitor cells, called neural stem cells (NSCs), through a process known as neurogenesis. [172] NSCs are very attractive for regeneration therapy in the nervous system. They hold an immense promise for regenerative therapy of neurological diseases, such as Parkinson's disease, Alzheimer's disease, spinal cord injury and gene delivery systems for brain tumor treatments. [173] Self-renewal of NSCs is modulated by the so-called NSCs niche, composed of cellular and acellular components. Besides the critical role of growth factors and hormones, the extracellular matrix (ECM) that supports the developing neural cells plays a fundamental role in cellular differentiation. [174, 175] Maintenance of stemness of stem cells and efficient differentiation are often difficult to manipulate, making it necessary to understand the relevant factors associated with NSCs proliferation and differentiation *in vitro*. Researchers have begun to use either ECM such as Matrigel© or individual ECM components such as collagen, laminin or fibronectin for *in vitro* neural differentiation experiments. [176, 177] Unfortunately, traditional NSCs cultures display several limitations. One major problem is the inability to precisely control the behavior of NSCs in culture. For example, precise and thorough combinatorial studies with multiple growth factors are technically infeasible using

traditional cultures, since they require relatively large volumes of media and correspondingly large amounts of costly growth factors and other reagents.[178] Microfluidic cell cultures offer the potential to overcome some of the limitations imposed by traditional culture tools. Moreover, 3D artificial microenvironments that mimic the *in vivo* microenvironments can be reconstructed for supporting the differentiation of NSCs. Several studies have characterized the physical, mechanical and biochemical cues for differentiation of NSCs by culturing these cells on micro-patterned ECMs or nano-structured substrates. [179, 180]

Here, as a proof of concept, a single-channel microfluidic system was presented for the differentiation of NSCs. The fully closed microfluidic device was designed to create *in vivo* like 3D microenvironments for NSCs by varying the deposition of a tiny layer of Matrigel© onto microfluidic walls. For this purpose, microfluidic devices were fabricated with poly(dimethylsiloxane) (PDMS) by a conventional soft lithography process, as reported previously. [135] The channel was covered with basic components of the basal lamina and NSCs were cultured into the single-channel device under a continuous supply of medium over two weeks, as depicted in **Figure 4.1**. In this study, NSCs were freshly isolated from the hippocampus of embryonic rats and dissociated first by enzymatic digestion in Trypsin-EDTA 0.25% (20 min at 37 °C) and subsequently by mechanical dissociation with a fine-tipped Pasteur pipette. The resulting tissue was resuspended in a Neurobasal medium supplemented with 2% B-27, 1% Glutamax-I, 1% Pen-Strep solution and 10% Fetal Bovine Serum. Afterward cells were plated onto a flask to form neurospheres. Neurospheres were checked under an optical microscope and ready to split when they reached 50-100um in diameters.. Afterward, neurospheres were collected from the flask, centrifuged, and resuspended in Accutase for gentle dissociation at 37°C by pipetting. Cell solution was then centrifuged again and cells were resuspended in complete DMEM

(+ 1% B27 + 1% P/S + 1% N2 + DMEM/F12 Glutamax + 20ng/ml EGF + 20ng/ml FGF) for seeding in microfluidic devices.

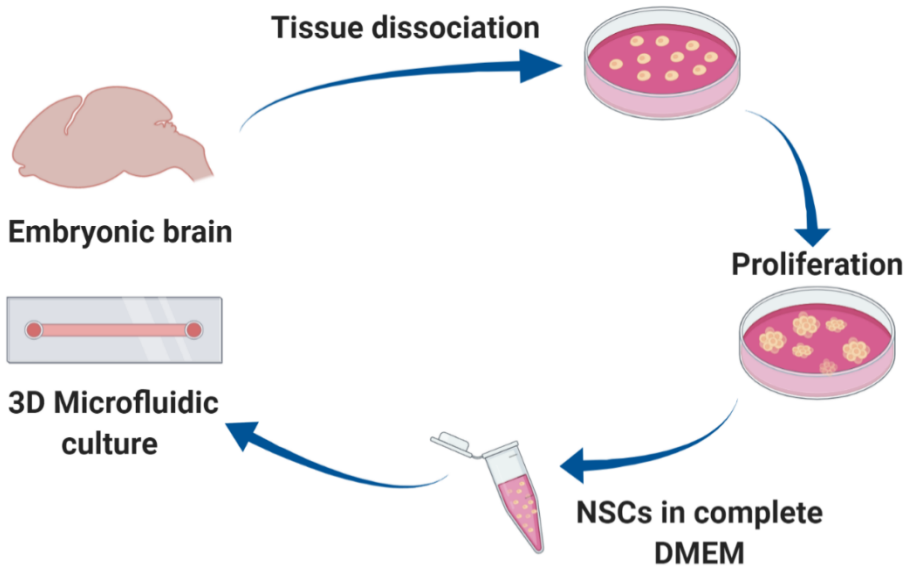

Figure 4.1. NSC differentiation in 3D microfluidic culture. Created with Biorender.com

Three types of ECM were tested for the NSC culture in a single-channel microfluidic device based on different incubation time of Growth Factor Reduced (GFR) Matrigel© diluted 1:50 (vol/vol) with complete DMEM: 40 minutes incubation (3D_40), 1 hour incubation (3D_60) and 2 hours incubation at 37°C (3D_120) (**Figure 4.2**). The main component of Matrigel is laminin; so to confirm the formation of the extracellular layer, immunocytochemical staining of laminin was employed and confocal images were acquired. The GFR Matrigel© formulation was used to examine the effect of matrix component on the NSC differentiation, excluding the effect of growth factors from the original Matrigel© formulation. Matrigel© solution was allowed to gel in the

microfluidic device, and then cells were flowed into the channel, allowing the attachment to the developed lamina.

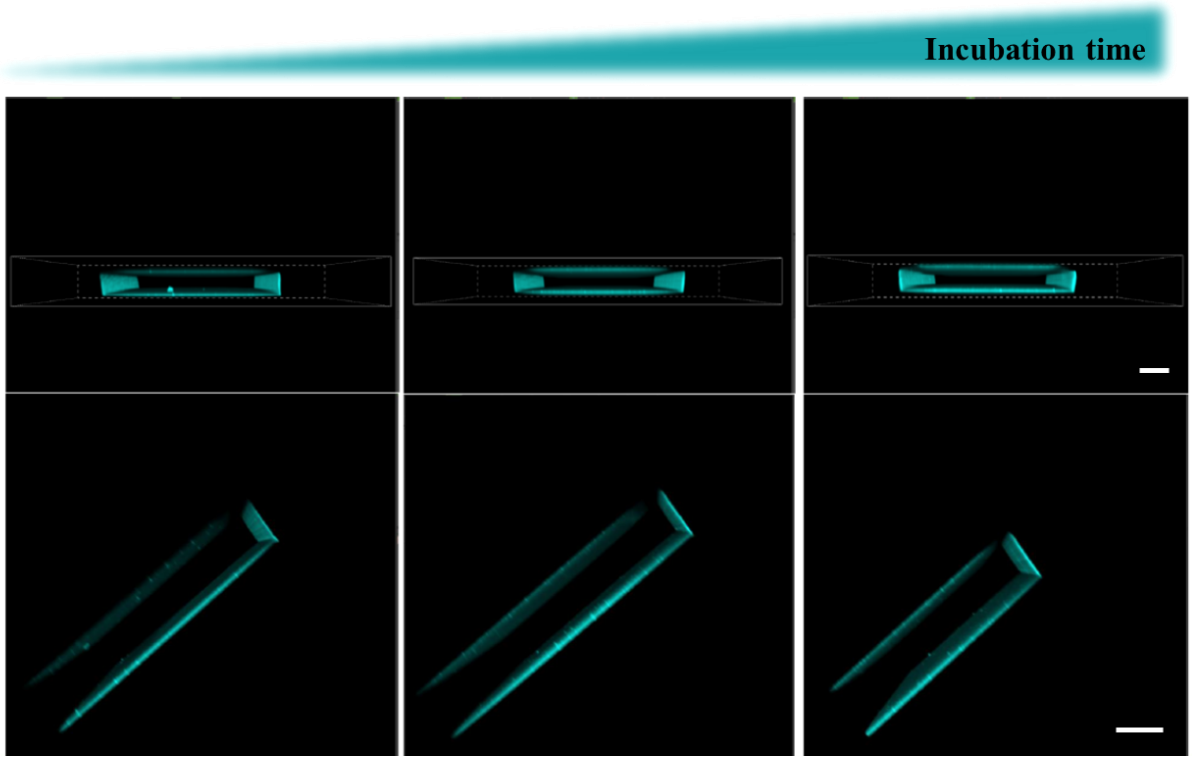

Figure 4.2. Extracellular layer in single-channel microfluidic device. GFR Matrigel (1:50) was allowed to polymerize for 40 minutes (left image), 1 hour (center image), and 2 hour (right image), forming a tiny layer of basal lamina. Scale bar is 50 µm.

NSCs were cultured for 5 days in proliferation medium and from day 5 until day16 differentiation was induced by simply flowing differentiation medium (Neurobasal medium + B-27 + 1% P/S +1% Glutamax + 50ng/ml BDNF) into the microfluidic channel and the medium was changed everyday. In the first five days, attachment and proliferation of NSCs were evaluated by microscopy analysis (**Figure 4.3**). After five days, NSCs displayed a characteristic phenotype normally observed under differentiation conditions, suggesting a possible effect of extracellular

layer component on NSCs differentiation. It was reported in several studies that laminin and laminin-enriched Matrigel© favored the differentiation of neural progenitor stem cells and neurite outgrowth. [181, 182]

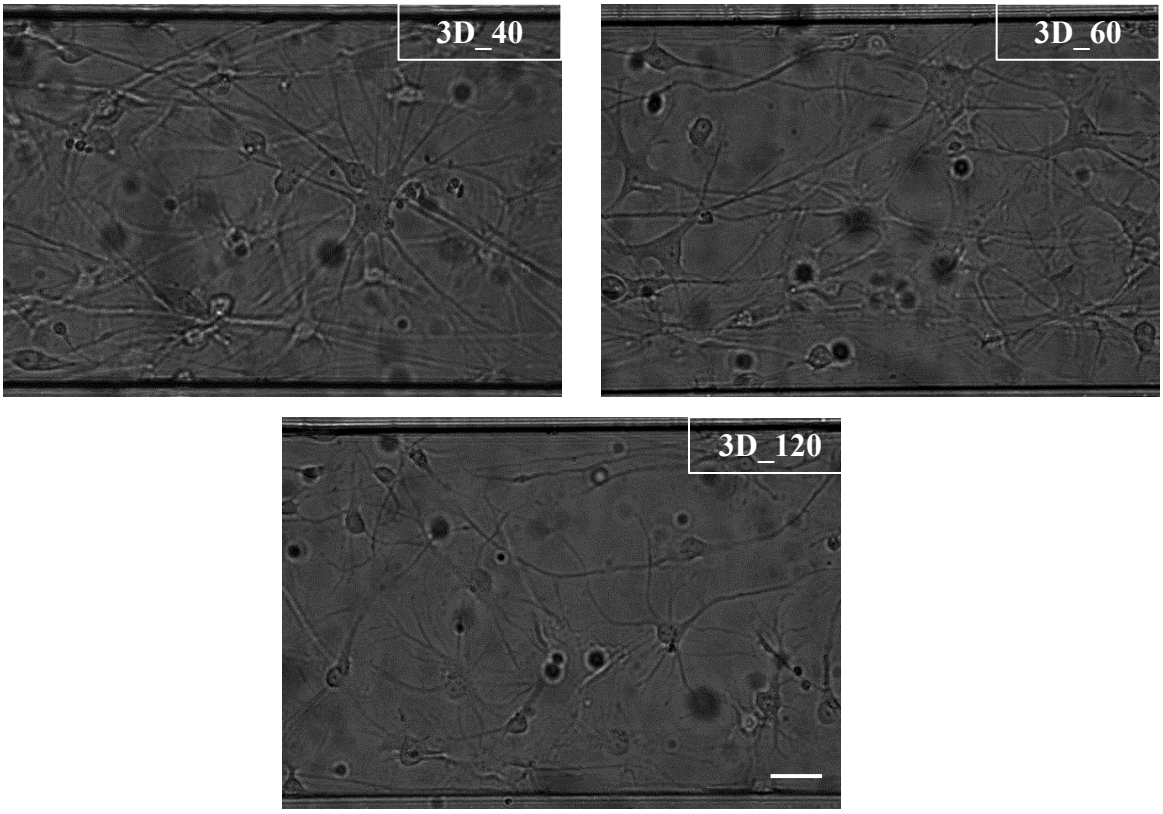

Figure 4.3. Proliferation of NSC in microfluidic device at day5. NSCs were cultured for five days in proliferation medium and the effect of extracellular layer were evaluated by microscopic analysis. Scale bar 20 μm.

From day 5 the NSCs in microfluidic devices were cultured under a differentiation medium until day 16. At the end of the experiment, immunocytochemistry analysis was performed to evaluate the differentiation of NSCs, targeting the neural stem/progenitor marker Nestin and β-tubulin III marker for mature neurons. As reported in **Figure 4.4**, NSCs in the microfluidic devices successfully differentiated into mature neurons. Laminin-enriched ECM was employed to

differentiate NSCs in the microfluidic device [183], thus confirming the preliminary results obtained in this work.

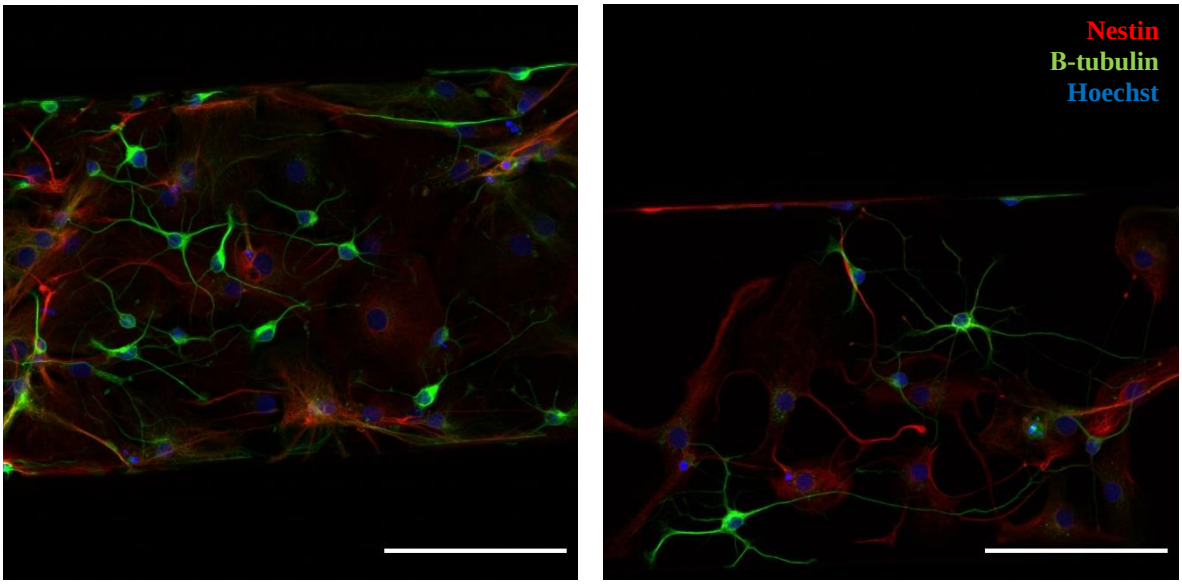

Figure 4.4. NSCs differentiation in ECM layered microfluidic device. After 16 days of culture in 3D_60 condition, NSCs differentiation was evaluated by staining of nestin (red) and beta-tubulin (green). Scale bar 100 µm.

In this study, a microfluidic system was reported as an experimental platform for culturing and differentiation of NSCs under different 3D ECM stimuli. The system provided essential *in vivo* like cues for stimulating and guiding NSC differentiation, offering the possibility of fine-tuning the neural stem cell niche. Future studies will determine how the 3D microenvironment affects the NSC differentiation and will also consider the incorporation of other ECM components (for example hyaluronic acid) and the incorporation of various soluble factors co-culturing conditions to recreate a more complex neuro-microfluidic device.

Chapter 5

Conclusion and Future Perspectives

In this thesis, single-channel and double-channel microfluidic devices were presented to reproduce *in vitro* organ-on-chip. The first chapter consists of the literature review of the microfluidic evolution of new devices' production to mimic organs-on-chip.

In the second chapter, a human microvessel-on-chip model was realized to reproduce macromolecules and polymeric nanoconstructs' vascular journey. To reproduce the human microvasculature, it was used the double-channel microfluidic chip. On one channel it was reproduced the vascular compartment, covered with endothelial cells, whereas on the second channel, it was reproduced the extracellular compartment, filled with a 3D matrix of collagen and Matrigel©. Endothelial cells formed a stable vascular barrier, replicating physiologically relevant values of permeability for small tracers and nanoparticles. It was demonstrated that vascular permeability could be modulated by specifically using Mannitol and Lexiscan as increasing permeability agents, resulting in permeability values 3-fold higher than basal value reported in physiological conditions . Also flow regime applied to the vascular barrier could be modulated from 0.2 dyne/cm^2 to mimic tumor flow conditions to 0.7 dyne/cm^2 to mimic physiological flow conditions. In this way, we recreated tumor-like conditions for testing the adhesion and margination of discoidal polymeric nanoconstructs with different mechanical stiffness. Collectively, these results demonstrated that the proposed double-channel microfluidic device

could be efficiently and effectively used to test the vascular behavior of a variety of drug delivery systems under various conditions. However, the proposed microfluidic device can be further optimized. First of all, human umbilical vein endothelial cells (HUVEC) are immortalized cell line, really easy to handle but with low resemblance of the human microvasculature and low expression of specific markers. For this reason, the next step is to consider the possibility to use primary endothelial cells or iPSC-derived endothelial cells to make the platform more similar to the *in vivo* physiology. Secondly, the extracellular compartment could be enriched with perivascular supportive cells, such as pericytes, smooth muscle cells and fibroblasts based on the vascular district's physiology that needs to be recapitulated.

In the third chapter, a glioblastoma-on-chip was realized by using both the single-channel and the double-channel microfluidic chip. The single-channel device simulated the direct injection/application of chemotherapy at the tumor site (i.e. *in situ*). In contrast, the double-channel device simulated the systemic administration of chemotherapy. Several chemotherapeutics, namely free docetaxel (DTXL), DTXL-SPN and Fmoc-Glc6P, were investigated. The study demonstrated as the 3D microfluidic chip is a more realistic environment compared to the 2D conditions, since U87-MG cells were more susceptible to DTXL chemotherapy when they were arranged in a 3D matrix as documented by a 50 times decrease in the characteristic IC_{50} values. The 3D microfluidic condition reproduced complex cell-matrix organization and mass transport process that are essentials to test the effectiveness of anti-cancer treatment. It is also important to mention that, as a future step, it will be possible to combine the microvessel-on-chip previously reported here and the glioblastoma-on-chip. In this way, we could mimic a blood-brain-tumor barrier model. This model would allow refining techniques and strategies for nanomedicine or new drugs to cross the BBB in an efficient way.

Chapter four presented the single-channel microfluidic device as a suitable platform for the differentiation of neural stem cells (NSCs). NSCs were successfully cultured over 16 days, and the differentiation into mature neurons was confirmed. The microfluidic system provided extracellular stimuli to guide and support the proliferation and differentiation of neural stem cells. This last chapter was an embryonic project that could represent the basis for future research. In fact, the combination of the systems produced during this thesis could converge into realizing a blood-brain-barrier model developed from the *in situ* differentiation of stem cells into the microfluidic devices.

Although other experiments need to be performed, the double-channel microfluidic system opens the way to reproduce the neurovascular unit, closely resembling the *in vivo* interactions in physiological and pathological conditions, as in glioblastoma. The three studies reported in this thesis highlighted functional characteristics of single components of the neurovascular unit. The double-channel microfluidic system offer the possibility of define the vascular- and the neuro-compartment, independently addressable but still ensuring the communication via direct and indirect contact. To this end, the first step of this work addressed the permeability of endothelial cells only interfaced the extravascular compartment made of an hydrogel composed by specific components of the basal lamina and the extracellular matrix. Subsequently, single components of the basal lamina has been selectively deposited as a single layer into the extravascular compartment, in a more physiological approach. Neural stem cells have been cultured in order to study the differentiation of neural stem cells into the major players of the BBB, i.e. astrocytes and neural cells. Lastly, we analyze the accumulation and dosage of anti-cancer drugs into the glioma-extravascular compartment. Future works will look at the combination of endothelial cells, neural cells and glioma cancer cells, in order to recapitulate key aspects of the BBB. In physiological

conditions, endothelial cells are interfaced with differentiated neural and glia cells, lading in their own deposited matrix, resembling the formation and cell-cell and cell-matrix interactions characteristics of an healthy BBB. In pathophysiological conditions, as in glioblastoma, cross-talk between cancer cells and glia cells can promote aggressiveness of cancer cells and drug-resistance. Moreover, it is important to highlight that also the matrix can be selectively tuned in composition and stiffness. In fact, it is noted that in cancer conditions it is promoted also a stiffening of the extracellular matrix. This can be easily addressed in our system, getting light on the effect of the stiffness of the matrix on all involved players: primarly cancer cells, but also endothelial cells and the accessibility to anti-cancer treatments.

With this new setup, it should be possible to gain a better insight into cell-cell and cell-matrix interactions and elucidate unknown mechanisms involved in stem cell differentiation, cell-cell crosstalk, and drug delivery. Most importantly, this microfluidic system will help minimize the gap between the *in vitro* and *in vivo* experiments, contributing to the reduction of animal experiments according to the 3R principles.

List of publications

MG Barbato, Rui C. Pereira, Hilaria Mollica, AnnaLisa Palange, Miguel Ferreira, Paolo Decuzzi. *«A Permeable on-Chip Microvasculature for Assessing the Transport of Macromolecules and Polymeric Nanoconstructs»*. J Colloid Interface Sci. **2021** Jul 15;594:409-423. doi: 10.1016/j.jcis.2021.03.053. Epub 2021 Mar 17. PMID: 33774397.

Ana M. Martins, **Maria Grazia Barbato**, Alessia Felici, Alexandra Brito, Iva Pashkuleva, Ricardo A. Pires, Rui L. Reis, Paolo Decuzzi. *«Modeling molecular and nano-therapies on brain tumor in compartimentalized microfluidic devices»*, submitted, **2021**

Ferreira M, Rizzuti IF, Palange AL, **Barbato MG**, Di Francesco V, Di Francesco M, Decuzzi P. *«Optimizing the pharmacological properties of discoidal polymeric nanoconstructs against triple negative breast cancer cells»*. Front Bioeng Biotechnol, **2020**

Palomba R, Palange AL, Rizzuti IF, Ferreira M, Cervadoro A, **Barbato MG**, Canale C, Decuzzi P. *«Modulating Phagocytic Cell Sequestration by Tailoring Nanoconstruct Softness»*. ACS Nano. February **2018**

Award and Conferences

Poster session, **Third Price Winner** for Poster in category "Nanotoxicology and nano-biocharacterization" at the European and Global Summit for Clinical Nanomedicine and Precision Medicine. Basel, October 26-28, **2020**. *Biomimetic microcapillary-on-a-chip to modulate endothelial permeability against nanodelivery systems.* **Maria Grazia Barbato**, Miguel Ferreira, Paolo Decuzzi

"Trainee Symposium for Organoids & Organs-on-chips 2020", August 11th **2020**, Virtual Event organized by Columbia University, August 11th 2020. Oral presentation entitled "*Biovessel-on-a-chip To Probe Endothelial Permeability Against Nanodelivery Systems*".

Poster session at Nanotechnology in Medicine II: Bridging Translational in vitro and in vivo Interfaces (ECI Conference Series), June 5-June 9, **2018** Albufeira, Portugal. **M.G. Barbato**, M.Ferreira, R.Palomba, A.Coclite, P.Lenarda, AL.Palange, P.Decuzzi, "*Modulating Nanoconstruct Stiffness As A Strategy For Targeting The Tumor Vasculature*"

References

1. Bikfalvi, A., *History and conceptual developments in vascular biology and angiogenesis research: a personal view.* Angiogenesis, 2017. **20**(4): p. 463-478.
2. Darland, D.C. and P.A. D'Amore, *Cell cell interactions in vascular development.* 2001.
3. Jain, R.K., *Molecular regulation of vessel maturation.* Nature medicine, 2003. **9**(6): p. 685-693.
4. Pugsley, M. and R. Tabrizchi, *The vascular system: An overview of structure and function.* Journal of pharmacological and toxicological methods, 2000. **44**(2): p. 333-340.
5. Potente, M. and T. Mäkinen, *Vascular heterogeneity and specialization in development and disease.* Nature Reviews Molecular Cell Biology, 2017. **18**(8): p. 477.
6. Aird, W., *Spatial and temporal dynamics of the endothelium.* Journal of Thrombosis and Haemostasis, 2005. **3**(7): p. 1392-1406.
7. Augustin, H.G. and G.Y. Koh, *Organotypic vasculature: from descriptive heterogeneity to functional pathophysiology.* Science, 2017. **357**(6353).
8. Clark, E.R. and E.L. Clark, *Observations on changes in blood vascular endothelium in the living animal.* American Journal of Anatomy, 1935. **57**(3): p. 385-438.
9. Claesson-Welsh, L., E. Dejana, and D.M. McDonald, *Permeability of the Endothelial Barrier: Identifying and Reconciling Controversies.* Trends in Molecular Medicine, 2020.
10. Yuan, W., et al., *Non-invasive measurement of solute permeability in cerebral microvessels of the rat.* Microvascular research, 2009. **77**(2): p. 166-173.
11. Yuan, S.Y. and R.R. Rigor. *Regulation of endothelial barrier function*. in *Colloquium Series on Integrated Systems Physiology: From Molecule to Function*. 2011. Morgan & Claypool Life Sciences.
12. Vandenbroucke, E., et al., *Regulation of endothelial junctional permeability.* Annals of the new York Academy of Sciences, 2008. **1123**(1): p. 134-145.
13. Dejana, E., F. Orsenigo, and M.G. Lampugnani, *The role of adherens junctions and VE-cadherin in the control of vascular permeability.* Journal of cell science, 2008. **121**(13): p. 2115-2122.
14. Navarro, P., L. Ruco, and E. Dejana, *Differential localization of VE-and N-cadherins in human endothelial cells: VE-cadherin competes with N-cadherin for junctional localization.* The Journal of cell biology, 1998. **140**(6): p. 1475-1484.
15. Radeva, M. and J. Waschke, *Mind the gap: mechanisms regulating the endothelial barrier.* Acta physiologica, 2018. **222**(1): p. e12860.
16. Aguilar-Cazares, D., et al., *Contribution of angiogenesis to inflammation and cancer.* Frontiers in oncology, 2019. **9**: p. 1399.
17. Park-Windhol, C. and P.A. D'Amore, *Disorders of vascular permeability.* Annual Review of Pathology: Mechanisms of Disease, 2016. **11**: p. 251-281.
18. Michel, C. and F. Curry, *Microvascular permeability.* Physiological reviews, 1999.
19. Nagy, J.A., et al., *Vascular permeability, vascular hyperpermeability and angiogenesis.* Angiogenesis, 2008. **11**(2): p. 109-119.

20. Curry, F.-R.E. and R.H. Adamson, *Vascular permeability modulation at the cell, microvessel, or whole organ level: towards closing gaps in our knowledge.* Cardiovascular research, 2010. **87**(2): p. 218-229.
21. Miles, A. and E.M. Miles, *Vascular reactions to histamine, histamine-liberator and leukotaxine in the skin of guinea-pigs.* The Journal of physiology, 1952. **118**(2): p. 228-257.
22. Whitesides, G.M., *The origins and the future of microfluidics.* nature, 2006. **442**(7101): p. 368-373.
23. Mark, D., et al., *Microfluidic lab-on-a-chip platforms: requirements, characteristics and applications.* Microfluidics based microsystems, 2010: p. 305-376.
24. Sackmann, E.K., A.L. Fulton, and D.J. Beebe, *The present and future role of microfluidics in biomedical research.* Nature, 2014. **507**(7491): p. 181-189.
25. Becker, H. and C. Gärtner, *Polymer microfabrication technologies for microfluidic systems.* Analytical and bioanalytical chemistry, 2008. **390**(1): p. 89-111.
26. Aumiller, G., et al., *Submicrometer resolution replication of relief patterns for integrated optics.* Journal of Applied Physics, 1974. **45**(10): p. 4557-4562.
27. Duffy, D.C., et al., *Rapid prototyping of microfluidic systems in poly (dimethylsiloxane).* Analytical chemistry, 1998. **70**(23): p. 4974-4984.
28. Hughes, M.P., K.F. Hoettges, and M.P. Hughes, *Microengineering in biotechnology*. Vol. 583. 2010: Springer.
29. Kuncova-Kallio, J. and P.J. Kallio. *PDMS and its suitability for analytical microfluidic devices*. in *2006 International Conference of the IEEE Engineering in Medicine and Biology Society*. 2006. IEEE.
30. Ingber, D.E., *Is it Time for Reviewer 3 to Request Human Organ Chip Experiments Instead of Animal Validation Studies?* Advanced Science, 2020. **7**(22): p. 2002030.
31. Van Duinen, V., et al., *Microfluidic 3D cell culture: from tools to tissue models.* Current opinion in biotechnology, 2015. **35**: p. 118-126.
32. Kimura, H., Y. Sakai, and T. Fujii, *Organ/body-on-a-chip based on microfluidic technology for drug discovery.* Drug metabolism and pharmacokinetics, 2018. **33**(1): p. 43-48.
33. Mittal, R., et al., *Organ-on-chip models: Implications in drug discovery and clinical applications.* Journal of cellular physiology, 2019. **234**(6): p. 8352-8380.
34. Ma, C., et al., *Organ-on-a-Chip: A New Paradigm for Drug Development.* Trends in Pharmacological Sciences, 2020.
35. Novak, R., et al., *Robotic fluidic coupling and interrogation of multiple vascularized organ chips.* Nature biomedical engineering, 2020. **4**(4): p. 407-420.
36. Fleischer, S., D.N. Tavakol, and G. Vunjak-Novakovic, *From arteries to capillaries: approaches to engineering human vasculature.* Advanced Functional Materials, 2020. **30**(37): p. 1910811.
37. Folkman, J. and C. Haudenschild, *Angiogenesis in vitro.* Nature, 1980. **288**(5791): p. 551-556.
38. Lee, S., et al., *Microfluidic-based vascularized microphysiological systems.* Lab on a Chip, 2018. **18**(18): p. 2686-2709.
39. Zervantonakis, I.K., et al., *Three-dimensional microfluidic model for tumor cell intravasation and endothelial barrier function.* Proceedings of the National Academy of Sciences, 2012. **109**(34): p. 13515-13520.

40. Chrobak, K.M., D.R. Potter, and J. Tien, *Formation of perfused, functional microvascular tubes in vitro.* Microvascular research, 2006. **71**(3): p. 185-196.
41. Zhao, S., et al., *Bio-functionalized silk hydrogel microfluidic systems.* Biomaterials, 2016. **93**: p. 60-70.
42. Xie, R., et al., *Engineering of hydrogel materials with perfusable microchannels for building vascularized tissues.* Small, 2020. **16**(15): p. 1902838.
43. Heintz, K.A., et al., *Fabrication of 3D biomimetic microfluidic networks in hydrogels.* Advanced healthcare materials, 2016. **5**(17): p. 2153-2160.
44. Noor, N., et al., *3D printing of personalized thick and perfusable cardiac patches and hearts.* Advanced Science, 2019. **6**(11): p. 1900344.
45. Offeddu, G.S., et al., *An on-chip model of protein paracellular and transcellular permeability in the microcirculation.* Biomaterials, 2019. **212**: p. 115-125.
46. Zhang, S., Z. Wan, and R.D. Kamm, *Vascularized organoids on a chip: Strategies for engineering organoids with functional vasculature.* Lab on a Chip, 2021.
47. Nashimoto, Y., et al., *Vascularized cancer on a chip: The effect of perfusion on growth and drug delivery of tumor spheroid.* Biomaterials, 2020. **229**: p. 119547.
48. Wild, C., E. Weiderpass, and B. Stewart, *World cancer report: cancer research for cancer prevention.* Lyon: International Agency for Research on Cancer, 2020: p. 23-33.
49. Sontheimer-Phelps, A., B.A. Hassell, and D.E. Ingber, *Modelling cancer in microfluidic human organs-on-chips.* Nature Reviews Cancer, 2019. **19**(2): p. 65-81.
50. Sun, W., et al., *Organ-on-a-Chip for Cancer and Immune Organs Modeling.* Advanced healthcare materials, 2019. **8**(4): p. 1801363.
51. Young, E.W., *Cells, tissues, and organs on chips: challenges and opportunities for the cancer tumor microenvironment.* Integrative Biology, 2013. **5**(9): p. 1096-1109.
52. Hsiao, A.Y., et al., *Microfluidic system for formation of PC-3 prostate cancer co-culture spheroids.* Biomaterials, 2009. **30**(16): p. 3020-3027.
53. Chen, M.B., et al., *Mechanisms of tumor cell extravasation in an in vitro microvascular network platform.* Integrative Biology, 2013. **5**(10): p. 1262-1271.
54. Kim, J., et al., *Three-Dimensional Human Liver-Chip Emulating Premetastatic Niche Formation by Breast Cancer-Derived Extracellular Vesicles.* ACS nano, 2020. **14**(11): p. 14971-14988.
55. Chramiec, A., et al., *Integrated human organ-on-a-chip model for predictive studies of anti-tumor drug efficacy and cardiac safety.* Lab on a Chip, 2020. **20**(23): p. 4357-4372.
56. Xu, Z., et al., *Application of a microfluidic chip-based 3D co-culture to test drug sensitivity for individualized treatment of lung cancer.* Biomaterials, 2013. **34**(16): p. 4109-4117.
57. Tan, H.-Y., H. Cho, and L.P. Lee, *Human mini-brain models.* Nature Biomedical Engineering, 2020: p. 1-15.
58. Teixeira, M.I., et al., *Recent developments in microfluidic technologies for central nervous system targeted studies.* Pharmaceutics, 2020. **12**(6): p. 542.
59. Jahromi, M.A.M., et al., *Microfluidic brain-on-a-chip: perspectives for mimicking neural system disorders.* Molecular neurobiology, 2019. **56**(12): p. 8489-8512.
60. Zhao, Y., et al., *Multiscale brain research on a microfluidic chip.* Lab on a Chip, 2020. **20**(9): p. 1531-1543.
61. Jackson-Holmes, E.L., et al., *Microfluidic perfusion modulates growth and motor neuron differentiation of stem cell aggregates.* Analyst, 2020. **145**(14): p. 4815-4826.

62. Amadio, S., et al., *Plasticity of primary microglia on micropatterned geometries and spontaneous long-distance migration in microfluidic channels.* BMC neuroscience, 2013. **14**(1): p. 1-13.
63. Shin, Y., et al., *Blood–brain barrier dysfunction in a 3D in vitro model of Alzheimer's disease.* Advanced Science, 2019. **6**(20): p. 1900962.
64. Kane, K.I., et al., *Passive controlled flow for Parkinson's disease neuronal cell culture in 3D microfluidic devices.* Organs-on-a-Chip, 2020. **2**: p. 100005.
65. Osaki, T., S.G. Uzel, and R.D. Kamm, *On-chip 3D neuromuscular model for drug screening and precision medicine in neuromuscular disease.* Nature protocols, 2020. **15**(2): p. 421-449.
66. Park, T.-E., et al., *Hypoxia-enhanced Blood-Brain Barrier Chip recapitulates human barrier function and shuttling of drugs and antibodies.* Nature communications, 2019. **10**(1): p. 1-12.
67. Pugsley, M.K. and R. Tabrizchi, *The vascular system. An overview of structure and function.* J Pharmacol Toxicol Methods, 2000. **44**(2): p. 333-40.
68. Komarova, Y. and A.B. Malik, *Regulation of endothelial permeability via paracellular and transcellular transport pathways.* Annu Rev Physiol, 2010. **72**: p. 463-93.
69. Hawkins, B.T. and T.P. Davis, *The blood-brain barrier/neurovascular unit in health and disease.* Pharmacol Rev, 2005. **57**(2): p. 173-85.
70. Chen, Y. and L. Liu, *Modern methods for delivery of drugs across the blood-brain barrier.* Adv Drug Deliv Rev, 2012. **64**(7): p. 640-65.
71. Patel, T., et al., *Polymeric nanoparticles for drug delivery to the central nervous system.* Adv Drug Deliv Rev, 2012. **64**(7): p. 701-5.
72. Choi, H.S., et al., *Renal clearance of quantum dots.* Nat Biotechnol, 2007. **25**(10): p. 1165-70.
73. Moghimi, S.M., A.C. Hunter, and J.C. Murray, *Long-circulating and target-specific nanoparticles: theory to practice.* Pharmacol Rev, 2001. **53**(2): p. 283-318.
74. Schnitzler, J.G., et al., *Surmounting the endothelial barrier for delivery of drugs and imaging tracers.* Atherosclerosis, 2020.
75. Aguilar-Cazares, D., et al., *Contribution of angiogenesis to inflammation and cancer.* Frontiers in Oncology, 2019. **9**.
76. Jain, R.K., *Barriers to drug delivery in solid tumors.* Sci Am, 1994. **271**(1): p. 58-65.
77. Jain, R.K. and T. Stylianopoulos, *Delivering nanomedicine to solid tumors.* Nat Rev Clin Oncol, 2010. **7**(11): p. 653-64.
78. Kim, Y., et al., *Probing nanoparticle translocation across the permeable endothelium in experimental atherosclerosis.* Proc Natl Acad Sci U S A, 2014. **111**(3): p. 1078-83.
79. Fang, J., H. Nakamura, and H. Maeda, *The EPR effect: Unique features of tumor blood vessels for drug delivery, factors involved, and limitations and augmentation of the effect.* Adv Drug Deliv Rev, 2011. **63**(3): p. 136-51.
80. Lee, A., et al., *Dexamethasone-loaded Polymeric Nanoconstructs for Monitoring and Treating Inflammatory Bowel Disease.* Theranostics, 2017. **7**(15): p. 3653-3666.
81. Casnocha, S.A., et al., *Permeability of human endothelial monolayers: effect of vasoactive agonists and cAMP.* Journal of Applied Physiology, 1989. **67**(5): p. 1997-2005.
82. Godin, B. and E. Touitou, *Transdermal skin delivery: predictions for humans from in vivo, ex vivo and animal models.* Advanced drug delivery reviews, 2007. **59**(11): p. 1152-1161.

83. Islam, M., S. Beverung, and R. Steward Jr, *Bio-inspired microdevices that mimic the human vasculature.* Micromachines, 2017. **8**(10): p. 299.
84. Sakolish, C.M., et al., *Modeling barrier tissues in vitro: methods, achievements, and challenges.* EBioMedicine, 2016. **5**: p. 30-39.
85. Bogorad, M.I., et al., *In vitro microvessel models.* Lab on a Chip, 2015. **15**(22): p. 4242-4255.
86. Miali, M.E., et al., *Leaf-Inspired Authentically Complex Microvascular Networks for Deciphering Biological Transport Process.* ACS Appl Mater Interfaces, 2019. **11**(35): p. 31627-31637.
87. Manneschi, C., et al., *A microfluidic platform with permeable walls for the analysis of vascular and extravascular mass transport.* Microfluidics and Nanofluidics, 2016. **20**(8): p. 113.
88. Ho, Y.T., et al., *A facile method to probe the vascular permeability of nanoparticles in nanomedicine applications.* Scientific reports, 2017. **7**(1): p. 1-13.
89. Wang, H.-F., et al., *Tumor-vasculature-on-a-chip for investigating nanoparticle extravasation and tumor accumulation.* ACS nano, 2018. **12**(11): p. 11600-11609.
90. Zhang, B., et al., *Biodegradable scaffold with built-in vasculature for organ-on-a-chip engineering and direct surgical anastomosis.* Nature materials, 2016. **15**(6): p. 669-678.
91. Price, G.M. and J. Tien, *Subtractive methods for forming microfluidic gels of extracellular matrix proteins.* Microdevices in biology and engineering. Boston, MA: Artech House, 2009: p. 235-248.
92. Kim, Y., et al., *Probing nanoparticle translocation across the permeable endothelium in experimental atherosclerosis.* Proceedings of the National Academy of Sciences, 2014. **111**(3): p. 1078-1083.
93. Kwak, B., et al., *Simulation of complex transport of nanoparticles around a tumor using tumor-microenvironment-on-chip.* Journal of Controlled Release, 2014. **194**: p. 157-167.
94. Tang, Y., et al., *A biomimetic microfluidic tumor microenvironment platform mimicking the EPR effect for rapid screening of drug delivery systems.* Scientific reports, 2017. **7**(1): p. 1-14.
95. Mollica, H., et al., *Two-channel compartmentalized microfluidic chip for real-time monitoring of the metastatic cascade.* ACS Biomaterials Science & Engineering, 2019. **5**(9): p. 4834-4843.
96. Key, J., et al., *Soft Discoidal Polymeric Nanoconstructs Resist Macrophage Uptake and Enhance Vascular Targeting in Tumors.* ACS Nano, 2015. **9**(12): p. 11628-41.
97. Palomba, R., et al., *Modulating Phagocytic Cell Sequestration by Tailoring Nanoconstruct Softness.* ACS Nano, 2018. **12**(2): p. 1433-1444.
98. Colasuonno, M., et al., *Erythrocyte-Inspired Discoidal Polymeric Nanoconstructs Carrying Tissue Plasminogen Activator for the Enhanced Lysis of Blood Clots.* ACS Nano, 2018. **12**(12): p. 12224-12237.
99. Palange, A.L., et al., *Deformable Discoidal Polymeric Nanoconstructs for the Precise Delivery of Therapeutic and Imaging Agents.* Mol Ther, 2017. **25**(7): p. 1514-1521.
100. Ferreira, M., et al., *Optimizing the Pharmacological Properties of Discoidal Polymeric Nanoconstructs Against Triple-Negative Breast Cancer Cells.* Frontiers in Bioengineering and Biotechnology, 2020. **8**(5).
101. Follain, G., et al., *Fluids and their mechanics in tumour transit: shaping metastasis.* Nature Reviews Cancer, 2019: p. 1-18.

102. Serna-Márquez, N., et al., *Fibrillar Collagen Type I Participates in the Survival and Aggregation of Primary Hepatocytes Cultured on Soft Hydrogels.* Biomimetics, 2020. **5**(2): p. 30.
103. McRae, M., et al., *Characterization of cell-cell junction changes associated with the formation of a strong endothelial barrier.* Tissue barriers, 2018. **6**(1): p. e1405774.
104. Neuwelt, E., et al., *Osmotic blood-brain barrier disruption: a new means of increasing chemotherapeutic agent delivery.* Transactions of the American Neurological Association, 1979. **104**: p. 256-260.
105. D'Amico, R.S., et al., *Super selective intra-arterial cerebral infusion of modern chemotherapeutics after blood–brain barrier disruption: where are we now, and where we are going.* Journal of Neuro-oncology, 2020: p. 1-18.
106. Jackson, S., et al., *The effect of regadenoson-induced transient disruption of the blood–brain barrier on temozolomide delivery to normal rat brain.* Journal of neuro-oncology, 2016. **126**(3): p. 433-439.
107. Kim, D.-G. and M.S. Bynoe, *A2A adenosine receptor regulates the human blood-brain barrier permeability.* Molecular neurobiology, 2015. **52**(1): p. 664-678.
108. Augustin, H.G. and G.Y. Koh, *Organotypic vasculature: From descriptive heterogeneity to functional pathophysiology.* Science, 2017. **357**(6353): p. eaal2379.
109. Ellis, C.G., J. Jagger, and M. Sharpe, *The microcirculation as a functional system.* Critical care, 2005. **9**(S4): p. S3.
110. McCoy, M.G., et al., *Collagen I hydrogel microstructure and composition conjointly regulate vascular network formation.* Acta biomaterialia, 2016. **44**: p. 200-208.
111. Anguiano, M., et al., *Characterization of three-dimensional cancer cell migration in mixed collagen-Matrigel scaffolds using microfluidics and image analysis.* PloS one, 2017. **12**(2).
112. Alimperti, S., et al., *Three-dimensional biomimetic vascular model reveals a RhoA, Rac1, and N-cadherin balance in mural cell–endothelial cell-regulated barrier function.* Proceedings of the National Academy of Sciences, 2017. **114**(33): p. 8758-8763.
113. Wong, J.F., et al., *Integrated electrochemical measurement of endothelial permeability in a 3D hydrogel-based microfluidic vascular model.* Biosensors and Bioelectronics, 2020. **147**: p. 111757.
114. Zheng, Y., et al., *In vitro microvessels for the study of angiogenesis and thrombosis.* Proceedings of the national academy of sciences, 2012. **109**(24): p. 9342-9347.
115. Michel, C. and F. Curry, *Microvascular permeability.* Physiological reviews, 1999. **79**(3): p. 703-761.
116. Abbott, N.J., L. Rönnbäck, and E. Hansson, *Astrocyte–endothelial interactions at the blood–brain barrier.* Nature reviews neuroscience, 2006. **7**(1): p. 41.
117. Campisi, M., et al., *3D self-organized microvascular model of the human blood-brain barrier with endothelial cells, pericytes and astrocytes.* Biomaterials, 2018. **180**: p. 117-129.
118. Secomb, T.W., *Mechanics of blood flow in the microcirculation.* Symp Soc Exp Biol, 1995. **49**: p. 305-21.
119. Laumann, M., et al., *Emerging attractor in wavy poiseuille flows triggers sorting of biological cells.* Physical review letters, 2019. **122**(12): p. 128002.
120. Lee, S.Y., M. Ferrari, and P. Decuzzi, *Shaping nano-/micro-particles for enhanced vascular interaction in laminar flows.* Nanotechnology, 2009. **20**(49): p. 495101.

121. Whitesides, G.M., *The origins and the future of microfluidics.* Nature, 2006. **442**(7101): p. 368-73.
122. Sackmann, E.K., A.L. Fulton, and D.J. Beebe, *The present and future role of microfluidics in biomedical research.* Nature, 2014. **507**(7491): p. 181-9.
123. Vlachogiannis, G., et al., *Patient-derived organoids model treatment response of metastatic gastrointestinal cancers.* Science, 2018. **359**(6378): p. 920-926.
124. Ranga, A., N. Gjorevski, and M.P. Lutolf, *Drug discovery through stem cell-based organoid models.* Adv Drug Deliv Rev, 2014. **69-70**: p. 19-28.
125. Zhang, Y.S., et al., *Bioprinting the Cancer Microenvironment.* ACS Biomater Sci Eng, 2016. **2**(10): p. 1710-1721.
126. Bhatia, S.N. and D.E. Ingber, *Microfluidic organs-on-chips.* Nat Biotechnol, 2014. **32**(8): p. 760-72.
127. van der Meer, A.D. and A. van den Berg, *Organs-on-chips: breaking the in vitro impasse.* Integr Biol (Camb), 2012. **4**(5): p. 461-70.
128. Park, T.E., et al., *Hypoxia-enhanced Blood-Brain Barrier Chip recapitulates human barrier function and shuttling of drugs and antibodies.* Nature Communications, 2019. **10**.
129. Herland, A., et al., *Quantitative prediction of human pharmacokinetic responses to drugs via fluidically coupled vascularized organ chips.* Nat Biomed Eng, 2020. **4**(4): p. 421-436.
130. Moraes, C., et al., *Organs-on-a-chip: a focus on compartmentalized microdevices.* Ann Biomed Eng, 2012. **40**(6): p. 1211-27.
131. Huh, D., G.A. Hamilton, and D.E. Ingber, *From 3D cell culture to organs-on-chips.* Trends Cell Biol, 2011. **21**(12): p. 745-54.
132. Schaff, U.Y., et al., *Vascular mimetics based on microfluidics for imaging the leukocyte--endothelial inflammatory response.* Lab Chip, 2007. **7**(4): p. 448-56.
133. Prabhakarpandian, B., et al., *Microfluidic devices for modeling cell-cell and particle-cell interactions in the microvasculature.* Microvasc Res, 2011. **82**(3): p. 210-20.
134. Omori, T., et al., *Hemodynamics in the microcirculation and in microfluidics.* Ann Biomed Eng, 2015. **43**(1): p. 238-57.
135. Mollica, H., et al., *Deciphering the relative contribution of vascular inflammation and blood rheology in metastatic spreading.* Biomicrofluidics, 2018. **12**(4): p. 042205.
136. Palange, A.L., et al., *Modulating the vascular behavior of metastatic breast cancer cells by curcumin treatment.* Front Oncol, 2012. **2**: p. 161.
137. King, M.R., et al., *A physical sciences network characterization of circulating tumor cell aggregate transport.* Am J Physiol Cell Physiol, 2015. **308**(10): p. C792-802.
138. Decuzzi, P., et al., *Flow chamber analysis of size effects in the adhesion of spherical particles.* Int J Nanomedicine, 2007. **2**(4): p. 689-96.
139. Decuzzi, P., et al., *Size and shape effects in the biodistribution of intravascularly injected particles.* J Control Release, 2010. **141**(3): p. 320-7.
140. Farokhzad, O.C., et al., *Microfluidic system for studying the interaction of nanoparticles and microparticles with cells.* Anal Chem, 2005. **77**(17): p. 5453-9.
141. Charoenphol, P., R.B. Huang, and O. Eniola-Adefeso, *Potential role of size and hemodynamics in the efficacy of vascular-targeted spherical drug carriers.* Biomaterials, 2010. **31**(6): p. 1392-402.
142. Bhatia, S.N. and D.E. Ingber, *Microfluidic organs-on-chips.* Nature Biotechnology, 2014. **32**(8): p. 760-772.

143. Choi, Y., et al., *A microengineered pathophysiological model of early-stage breast cancer.* Lab Chip, 2015. **15**(16): p. 3350-7.
144. Carvalho, M.R., et al., *Colorectal tumor-on-a-chip system: A 3D tool for precision onco-nanomedicine.* Science Advances, 2019. **5**(5).
145. Manneschi, C., et al., *A microfluidic platform with permeable walls for the analysis of vascular and extravascular mass transport.* Microfluidics and Nanofluidics, 2016. **20**(8).
146. Vatine, G.D., et al., *Human iPSC-Derived Blood-Brain Barrier Chips Enable Disease Modeling and Personalized Medicine Applications.* Cell Stem Cell, 2019. **24**(6): p. 995-1005 e6.
147. Chen, M.B., et al., *On-chip human microvasculature assay for visualization and quantification of tumor cell extravasation dynamics.* Nat Protoc, 2017. **12**(5): p. 865-880.
148. Funamoto, K., et al., *A novel microfluidic platform for high-resolution imaging of a three-dimensional cell culture under a controlled hypoxic environment.* Lab Chip, 2012. **12**(22): p. 4855-63.
149. Osaki, T., V. Sivathanu, and R.D. Kamm, *Engineered 3D vascular and neuronal networks in a microfluidic platform.* Sci Rep, 2018. **8**(1): p. 5168.
150. Zhang, B., et al., *Microfabrication of AngioChip, a biodegradable polymer scaffold with microfluidic vasculature.* Nat Protoc, 2018. **13**(8): p. 1793-1813.
151. Zervantonakis, I.K., et al., *Three-dimensional microfluidic model for tumor cell intravasation and endothelial barrier function.* Proc Natl Acad Sci U S A, 2012. **109**(34): p. 13515-20.
152. Pavesi, A., et al., *Using microfluidics to investigate tumor cell extravasation and T-cell immunotherapies.* Conf Proc IEEE Eng Med Biol Soc, 2015. **2015**: p. 1853-6.
153. Roberts, S.A., A.E. Waziri, and N. Agrawal, *Development of a Single-Cell Migration and Extravasation Platform through Selective Surface Modification.* Anal Chem, 2016. **88**(5): p. 2770-6.
154. Adriani, G., et al., *A 3D neurovascular microfluidic model consisting of neurons, astrocytes and cerebral endothelial cells as a blood-brain barrier.* Lab Chip, 2017. **17**(3): p. 448-459.
155. Lee, S.W.L., et al., *Modeling Nanocarrier Transport across a 3D In Vitro Human Blood-Brain-Barrier Microvasculature.* Adv Healthc Mater, 2020. **9**(7): p. e1901486.
156. Cloughesy, T.F., W.K. Cavenee, and P.S. Mischel, *Glioblastoma: From Molecular Pathology to Targeted Treatment.* Annual Review of Pathology: Mechanisms of Disease, Vol 9, 2014. **9**: p. 1-25.
157. Gao, H.L., et al., *Whole-cell SELEX aptamer-functionalised poly(ethyleneglycol)-poly(epsilon-caprolactone) nanoparticles for enhanced targeted glioblastoma therapy.* Biomaterials, 2012. **33**(26): p. 6264-6272.
158. Gao, H.L., et al., *In vitro and in vivo intracellular distribution and anti-glioblastoma effects of docetaxel-loaded nanoparticles functioned with IL-13 peptide.* International Journal of Pharmaceutics, 2014. **466**(1-2): p. 8-17.
159. Stigliano, C., et al., *Radiolabeled Polymeric Nanoconstructs Loaded with Docetaxel and Curcumin for Cancer Combinatorial Therapy and Nuclear Imaging.* Advanced Functional Materials, 2015. **25**(22): p. 3371-3379.
160. Lee, A., et al., *Spherical polymeric nanoconstructs for combined chemotherapeutic and anti-inflammatory therapies.* Nanomedicine-Nanotechnology Biology and Medicine, 2016. **12**(7): p. 2139-2147.

161. Gelmon, K., *The Taxoids - Paclitaxel and Docetaxel.* Lancet, 1994. **344**(8932): p. 1267-1272.
162. Kuppens, I.E., *Current state of the art of new tubulin inhibitors in the clinic.* Curr Clin Pharmacol, 2006. **1**(1): p. 57-70.
163. Shi, C.H., et al., *Docetaxel-loaded PEO-PPO-PCL/TPGS mixed micelles for overcoming multidrug resistance and enhancing antitumor efficacy.* Journal of Materials Chemistry B, 2015. **3**(20): p. 4259-4271.
164. Pires, R.A., et al., *Controlling Cancer Cell Fate Using Localized Biocatalytic Self-Assembly of an Aromatic Carbohydrate Amphiphile.* Journal of the American Chemical Society, 2015. **137**(2): p. 576-579.
165. Brito, A., et al., *Inhibiting cancer metabolism by aromatic carbohydrate amphiphiles that act as antagonists of the glucose transporter GLUT1* Chemical Science, 2020.
166. Brito, A., et al., *Aromatic carbohydrate amphiphile disrupts cancer spheroids and prevents relapse.* Nanoscale, 2020.
167. Nishioka, T., et al., *Distribution of the glucose transporters in human brain tumors.* Cancer research, 1992. **52**(14): p. 3972-3979.
168. Pistollato, F., et al., *Intratumoral hypoxic gradient drives stem cells distribution and MGMT expression in glioblastoma.* Stem cells, 2010. **28**(5): p. 851-862.
169. Sontheimer-Phelps, A., B.A. Hassell, and D.E. Ingber, *Modelling cancer in microfluidic human organs-on-chips.* Nat Rev Cancer, 2019. **19**(2): p. 65-81.
170. Gomez-Roman, N., et al., *A novel 3D human glioblastoma cell culture system for modeling drug and radiation responses.* Neuro-oncology, 2017. **19**(2): p. 229-241.
171. Melissaridou, S., et al., *The effect of 2D and 3D cell cultures on treatment response, EMT profile and stem cell features in head and neck cancer.* Cancer cell international, 2019. **19**(1): p. 16.
172. Temple, S., *The development of neural stem cells.* Nature, 2001. **414**(6859): p. 112-117.
173. Teixeira, A.I., J.K. Duckworth, and O. Hermanson, *Getting the right stuff: controlling neural stem cell state and fate in vivo and in vitro with biomaterials.* Cell research, 2007. **17**(1): p. 56-61.
174. Adams, J.C. and F.M. Watt, *Regulation of development and differentiation by the extracellular matrix.* Development, 1993. **117**(4): p. 1183-1198.
175. Barros, C.S., S.J. Franco, and U. Müller, *Extracellular matrix: functions in the nervous system.* Cold Spring Harbor perspectives in biology, 2011. **3**(1): p. a005108.
176. Hughes, C.S., L.M. Postovit, and G.A. Lajoie, *Matrigel: a complex protein mixture required for optimal growth of cell culture.* Proteomics, 2010. **10**(9): p. 1886-1890.
177. Uemura, M., et al., *Matrigel supports survival and neuronal differentiation of grafted embryonic stem cell-derived neural precursor cells.* Journal of neuroscience research, 2010. **88**(3): p. 542-551.
178. Beebe, D.J., G.A. Mensing, and G.M. Walker, *Physics and applications of microfluidics in biology.* Annual review of biomedical engineering, 2002. **4**(1): p. 261-286.
179. Christopherson, G.T., H. Song, and H.-Q. Mao, *The influence of fiber diameter of electrospun substrates on neural stem cell differentiation and proliferation.* Biomaterials, 2009. **30**(4): p. 556-564.
180. Solanki, A., et al., *Controlling differentiation of neural stem cells using extracellular matrix protein patterns.* small, 2010. **6**(22): p. 2509-2513.

181. Hall, P.E., J.D. Lathia, and M.A. Caldwell, *Laminin enhances the growth of human neural stem cells in defined culture media.* BMC neuroscience, 2008. **9**(1): p. 1-10.
182. Ma, W., et al., *Cell-extracellular matrix interactions regulate neural differentiation of human embryonic stem cells.* BMC developmental biology, 2008. **8**(1): p. 1-13.
183. Han, S., et al., *Three-dimensional extracellular matrix-mediated neural stem cell differentiation in a microfluidic device.* Lab on a Chip, 2012. **12**(13): p. 2305-2308.